



Evaluating Hydrodynamic and Bathtub Water-Level Models to Assess Storm Surge Flooding in the Canadian Arctic

The case of Tuktoyaktuk, Northwest Territories, Canada

Daniel António Gaudêncio Pinheiro

Thesis to obtain the Master of Science Degree in

Environmental Engineering

Supervisors: Prof. Gonçalo Brito Guapo Teles Vieira, Prof. João Alfredo Vieira Canário

Examination Committee

Chairperson: Prof. Ramiro Joaquim de Jesus Neves

Supervisors: Prof. Gonçalo Vieira, Prof. João Canário

Members of the Committee: Prof. Eusébio Joaquim Marques dos Reis

December 2021

I declare that this document is an original work of my own authorship and that it fulfils all the requirements of the Code of Conduct and Good Practices of the Universidade de Lisboa.

I. Acknowledgements

To start, I would like to warmly thank my supervisors and mentors, Gonçalo Vieira, Dustin Whalen and João Canário for the guidance, support, friendliness, and inspiration since the first day. I am incredibly grateful and honoured for all I have learned with them and how this collaboration shaped me as a person.

I wish to acknowledge the support of PROPOLAR - Portuguese Polar Program (FCT), POLAR2E, Nunataryuk project, Natural Resources Canada and the Geological Survey of Canada for providing data, handling all the logistics, traveling and accommodation expenses.

A special thanks to the community of Tuktoyaktuk for the hospitality.

I am thankful to the wonderful and inspiring people I met along the way, especially Pedro Freitas, Pedro Pina, Bay, Danika, Angus, Paul Fraser and Calvin Pokiak. This research would not be possible without them.

I sincerely thank my father, António, for always believing in me.

Lastly but most important, thank you Hanna for always being there for me.

This work is part of the Nunataryuk funded under the European Union's Horizon 2020 Research and Innovation Programme under grant agreement no. 773421, and with co-funding by the Climate Change Preparedness in the North (CCPN) program.

II. Resumo

O aquecimento do Ártico está a levar a uma redução acelerada do gelo marinho, com modelos para 2100 a indicar a redução de 43 a 94% da sua área em setembro e de 8 a 34% em fevereiro (IPCC, 2021). O aumento da duração da estação livre de gelo vai resultar numa maior exposição do litoral à ação das ondas, com o clima também a modificar a contribuição dos processos de erosão terrestre. Durante a curta época de água livre de gelo (junho a outubro) existe um aumento das tempestades costeiras no Mar de Beaufort, levando a um incremento na erosão costeira e inundações (Fritz et al., 2015, Ramage et al., 2018)

Este trabalho focou-se na comunidade costeira de Tuktoyaktuk (Territórios do Noroeste, Canadá), onde foram recolhidas imagens aéreas de alta resolução com recurso a veículos aéreos não tripulados (VANT), permitindo criar ortofotomapas e modelos digitais de superfície (MDS) que foram usados como base para um modelo probabilístico de inundação e um modelo hidrodinâmico, MOHID.

A partir dos cenários RCP4.5 e RCP8.5 de subida do nível do IPCC, e usando o modelo probabilístico e o MDS de alta resolução, é esperado, respetivamente, que 29,2 a 32,2% (MOHID: 14,4 a 16,1 %) da área de estudo fique submersa em 2100. Estas percentagens podem variar de 76,5 a 80,7% (MOHID: 56 a 60%) em episódios extremos associados a sobrelevação do nível do mar para tempestades com um período de retorno de 100 anos.

Palavras-chave: inundação costeira, modelo bathtub, modelo hidrodinâmico, VANT, LIDAR, alterações climáticas

III. Abstract

Arctic warming is leading to an increased reduction in sea ice, with models for 2100 indicating a reduction in the Arctic sea ice area from 43 to 94% in September and from 8 to 34% in February (IPCC, 2021). The increase of the sea-ice free season duration will result in more exposure of the coasts to wave action, with changing climate also modifying the contribution of terrestrial erosion processes. The increase of the sea-ice free season duration will result in more exposure of the coasts to wave action, with changing climate also modifying the contribution of terrestrial erosion processes. During the short open water season (June to October) there has been an increase in coastal storms in the Beaufort Sea this has led to an increment in coastal erosion and flooding (Fritz et al., 2015, Ramage et al., 2018).

This work focused on the Hamlet of Tuktoyaktuk (Northwest Territories, Canada), where ultra-high-resolution surveys with unmanned aerial vehicles (UAVs) have been conducted, allowing to generate orthophoto mosaics and digital surface models (DSM) that were used as inputs for a probabilistic flood model and MOHID hydrodynamic model.

From the IPCC scenarios RCP4.5 and RCP8.5, respectively, it is expected that 29.2 to 32.2% (MOHID: 14.4 to 16.1%) of the study area is permanently submerged by 2100, only accounting for the sea level rise. These percentages can go up to 76.5 to 80% (MOHID: 56 to 60%) during a storm surge event with a 100-year return period.

Keywords: flood map, coastal flooding, bathtub modelling, hydrodynamic modelling, UAV, LiDAR, climate change

IV. Table of Contents

I.	Acknowledgements.....	3
II.	Resumo.....	5
III.	Abstract	6
IV.	Table of Contents	7
V.	List of Figures.....	10
VI.	List of Tables.....	15
VII.	List of Abbreviations.....	16
1.	Introduction	17
1.1.	Problem Characterization.....	17
1.2.	Objectives and Methodology.....	19
1.3.	Structure of the Thesis	19
2.	State of the Art.....	20
2.1.	Sea Level Rise Projections	20
2.1.	Storm Surges	22
2.2.	Coastal Erosion	23
3.	Characterization of the Study Area.....	25
3.1.	Regional Setting.....	25
3.2.	Characteristics of the Hamlet of Tuktoyaktuk	27
3.3.	Coastal Erosion and Flooding in Tuktoyaktuk.....	28
4.	Data and Methods.....	32
4.1.	Introduction.....	32
4.2.	Topographic Data.....	34
4.2.1.	Airborne LiDAR	34
4.2.2.	UAV Digital Surface Model.....	36
4.2.3.	Field Survey of Culverts	38
4.3.	Tide Data and Storm Surge Assessment.....	40

4.4.	Time-lapse Cameras for Storm Surge Analysis	41
4.5.	Driftwood Mapping	42
4.6.	Bathtub Flood Modelling	43
4.6.1.	Model Description.....	43
4.6.2.	Model Setup	48
4.7.	Hydrodynamic Flood Modelling (MOHID)	51
4.7.1.	Model description	51
4.7.2.	Model Setup	53
4.8.	Validation of the Model Results.....	56
4.8.1.	Local Knowledge and Field Observations.....	56
4.8.2.	UAV Imagery Analysis and Chart Datum Conversion.....	56
5.	Analysis and Discussion of the Results	58
5.1.	Data Uncertainty Assessment.....	58
5.1.1.	Chart Datum Conversion to CGVD2013	58
5.2.	Harmonic Analysis of the Tides.....	63
5.3.	Storm Surge Analysis.....	64
5.4.	Validation of the Models.....	66
5.4.1.	UAV Imagery Analysis	66
5.4.1.	Storm Surge Time-lapse Analysis.....	68
a)	Flood event: 4 th of August 2019	68
b)	Flood event: 5 th of August 2019	69
5.4.2.	Historical Flood Event: 1963 – Highest Water Level Recorded.....	71
5.5.	Sea Level Change and Shore Line Retreat in the 21 st Century.....	73
5.6.	Storm Surge Flood Modelling in the 21 st Century	80
5.6.1.	50-year Return Period Storm Surge Event	80
5.6.2.	100-year Return Period Storm Surge Event	86
5.7.	Presently Flood Exposed Infrastructure.....	92
5.7.1.	Transportation and Buildings	93
6.	Conclusions and Outlook.....	96

7. References.....	98
8. Appendix.....	109

V. List of Figures

Figure 1 – The Beaufort coast showing the location of Tuktoyaktuk.	18
Figure 2 – Storm surge event in Tuktoyaktuk that took place in the 4 th of august 2019 where the wave run-up reached several buildings located near Flagpole Point.	18
Figure 3 - Time series of global annual change in mean surface temperature for the 2006–2100 period (relative to 1986–2005) from Coupled Model Intercomparison Project Phase 5 (CMIP5) concentration-driven experiments. Projections are shown for the multi-model mean (solid lines) and the 5% to 95% range across the distribution of individual models (shading). Grey lines and shading represent the CMIP5 historical simulations (IPCC, 2013).	21
Figure 4 - Derived vertical crustal motion from GPS for Canada and surrounding regions (Craymer et al.,2011).	22
Figure 5 - Storm surge schematic representation. (NOAA, 2021)	23
Figure 6 – The Tuktoyaktuk Peninsula area (Côté and Burn, 2002).	25
Figure 7 – Bathymetric contours surrounding Tuktoyaktuk Peninsula (Wolfe et al., 1998)	26
Figure 8 –Study area boundary and spatial distribution of the assessed buildings extracted from NWT Administration of the Territorial Land Acts System (ATLAS) (Government of Northwest Territories, 2021).	28
Figure 9 - Coastal erosion progression estimates (Johnson et al., 2003).	29
Figure 10 – Open-water season hourly water level data extracted from Tuktoyaktuk tide gauge.....	30
Figure 11 – Methodology flowchart.....	33
Figure 12 - 2004 LiDAR DEM of the study area in CGVD2013 and a spatial resolution of 1 meter.	35
Figure 13 - DSM derived from the UAV flights and used for modelling with a cell size of 0.1 by 0.1 m.....	37
Figure 14 – Location of all the surveyed culverts included in both models.	38
Figure 15 – Culverts 1 and 2, representing the connectivity of an area that was previously considered as unconnected in the DEMs without the incorporation of the culvert system. A) Facing North. B) Facing South.	39
Figure 16 – Original UAV DSM with two of the surveyed culverts. Note that the topography of the culverts is visible in the DSM.....	39
Figure 17 – Elevation changes after the implementation of linear interpolation for Culvert 1.	40
Figure 18 – Location of Tuktoyaktuk relative to the IPCC sea level rise data predictions sampling point from https://icdc.cen.uni-hamburg.de/las/getUI.do (Church et al., 2013).	40
Figure 19 – Predicted sea level rise based on IPCC Scenarios RCP4.5 and RCP8.5 with a confidence interval of 95% relative to 1986-2005 for Tuktoyaktuk – extracted at 70.5 N; 133.5 W from https://icdc.cen.uni-hamburg.de/las/getUI.do (Church et al., 2013).	41

Figure 20 – Location of the time-lapse camera and other pictures taken during the storm event of the 5 th of August 2019.	42
Figure 21 – Driftwood accumulation in Tuktoyaktuk. A) Picture taken during field work. B) Driftwood debris visible from UAV footage.....	43
Figure 22 – Spatial distribution and location of the points used to determine the difference between Chart Datum and CGVD2013.	45
Figure 23 – Spatial distribution of the points used to determine elevation dataset RMSE. A) UAV. B) LiDAR.	46
Figure 24 - Z-scores / Standard-Scores and normal distribution.	46
Figure 25 - Estimation of flooding probability for an inundation level of 2.5 m for different terrain elevations accounting for uncertainty by applying NOAA's Coastal Services Center method. Adapted from (Antunes et al., 2019). For the indexes, see Table 2.	47
Figure 26 – Different bathtub approaches. (a) zero connectivity rule; (b) four-way connectivity in orthogonal directions, excluding cells not connected to the sea and (c) eight-way hydrological connectivity rule for 1 m SLR where a cell is flooded only if it is connected to a water body directly or via adjacent cells in either orthogonal or diagonal directions (Yunus et al., 2016).	49
Figure 27 – ArcGIS Pro Model Builder process used for bathtub modelling.	50
Figure 28 - Hydrodynamic Module flux of information with other modules. Adapted from MARETEC (2012).	52
Figure 29 – Sigma layers with 4 layers. Adapted from MARETEC (2012)	53
Figure 30 –Hydrodynamic modelling workflow diagram.	53
Figure 31 – Hydrodynamic model extent and excluded areas.....	54
Figure 32 – Interpolated bathymetry surface used in the hydrodynamic modelling.	55
Figure 33 – Location of the points used to validate the inundation models.....	57
Figure 34 - Absolute error in meters by gauge height sampling point.	58
Figure 35 – Boxplot of Gauge Height Sampling Points difference between CGVD2013 and Chart Datum.	60
Figure 36 – Spatial distribution of the squared differences of Z-GPS and Z-DSM and Z-DEM in CGVD2013.	61
Figure 37 – Difference between UAV DSM and LiDAR DEM in CGVD2013.	62
Figure 38 – Output of harmonic analysis for Tuktoyaktuk tide gauge in meters above Chart Datum.	63
Figure 39 – Yearly maximum tide height and linear trend in meters above Chart Datum derived from the harmonic analysis.	63
Figure 40 – Residual non-tidal hourly water level plotted after removing the astronomical tide and MSL obtained by harmonic analysis.....	64
Figure 41 – Gumbel frequency distribution and QQ-plot from the Gumbel distribution.....	65

Figure 42 – Gumbel distribution output of the storm surge water levels obtained from MATLAB Flood Frequency Distribution package.	65
Figure 43 – Bathtub model validation and shoreline prediction for sampling points 1 and 4. A) LiDAR DEM. B) UAV DSM	67
Figure 44 - MOHID validation and shoreline prediction for sampling points 15 and 16. A) LiDAR DEM. B) UAV DSM.....	68
Figure 45 – Time-lapse pictures taken during the storm surge event on the 4 th of august 2019. A) 07:05. B) 17:40. (Local time)	69
Figure 46 – Results of both flood models ran on the different elevation datasets rendered in ArcGIS Pro at the time-lapse camera position for the water-level read at 17:40. A) Bathtub model and UAV DSM. B) MOHID and UAV DSM. C) Bathtub model and LiDAR DEM. D) MOHID and LiDAR DEM.	69
Figure 47 – Picture taken on Tuktu Road by Kitti Hall on the 5 th of august 2019 at 9:47 AM (GMT -6:00) during a storm surge event with a water level of 1.39 m above Chart Datum.	70
Figure 48 - Bathtub model output for the same water level as Figure 47 by hazard class, rendered in ArcGIS Pro. A) UAV DSM B) LiDAR DEM	70
Figure 49 - Hydrodynamic model output at the same location and same time a Figures 64 and 65, rendered in ArcGIS Pro. A) UAV DSM. B) LiDAR DEM. The yellow polygon represents an unconnected area, therefore classified as not flooded.	70
Figure 50 – Bathtub model output for UAV DSM, LiDAR DEM and the areas estimated by both datasets for all hazard classes (2 to 5), for the water level of 2.23 m above CD registered at 2:00 PM on 4/10/1963. .	71
Figure 51 – Matching driftwood locations by hazard class and mismatching points for the bathtub model for the water level of 2.23 m above CD registered at 2:00 PM on 4/10/1963. A) UAV DSM and B) LiDAR DEM.	72
Figure 52 – Number of driftwood points identified as matching points by the elevation dataset and by hazard class for the bathtub model.....	72
Figure 53 - Matching driftwood locations and mismatching points for the hydrodynamic model for the water level of 2.23 m above CD registered at 2:00 PM on 4/10/1963. A) UAV DSM and B) LiDAR DEM.....	73
Figure 54 – Comparison of the total area flooded (m ²) of both models for LiDAR and UAV by scenario. The year 2020 does not correspond to any RCP scenario and only represents the mean highest astronomical tide added to the 2020 mean sea level. The “all classes” classification stands for the grouping of the hazard classes from 5 to 2.	76
Figure 55 – Bathtub model results comparison between the total area flooded by hazard class for the RCP4.5 scenario.	76
Figure 56 - Bathtub model results comparison between the total area flooded by hazard class for the RCP8.5 scenario.	77
Figure 57 –Bathtub model predicted highest astronomical tide for the year 2100 by hazard class on UAV DSM. A) RCP4.5 and B) RCP8.5.....	78

Figure 58 – Bathtub model predicted highest astronomical tide for the year 2100 by hazard class on LiDAR DEM.A) RCP4.5 and B) RCP8.5.....	78
Figure 59 - Hydrodynamic model predicted highest astronomical tide in 2020 and for 2060 and 2100 based on the UAV DSM. A) RCP4.5 and B) RCP8.5.	79
Figure 60 - Hydrodynamic model predicted highest astronomical tide in 2020 and for 2060 and 2100 based on the LiDAR DEM. A) RCP4.5 and B) RCP8.5.	79
Figure 61 – Differences between MOHID and bathtub models for the year 2100 on a RCP8.5 scenario. A) UAV DSM. B) LiDAR DEM.....	80
Figure 62 - Comparison between total area flooded by elevation dataset for the bathtub model. The scenario represented is RCP8.5 for the year of 2100 and a 50-year return period storm surge.	82
Figure 63 - MOHID flooded areas for 2020, 2060 and 2100 for the RCP8.5 scenario with a 50-year return period storm surge on UAV DSM.....	83
Figure 64 – Flooded buildings by model for the year 2100 and scenario RCP8.5 with a 50-year return period storm surge event on UAV DSM. A) Bathtub. B) MOHID.	85
Figure 65 – Flooded roads obtained from bathtub model for the year of 2100 and RCP8.5 scenario for a 50-year return period storm surge event on UAV DSM.	86
Figure 66 – Comparison between the UAV DSM and LiDAR DEM outputs from the bathtub model for the year 2100 and scenario RCP8.5 for a 100-year return period storm surge event. Hazard classes (2 to 5) are grouped as one single class.	88
Figure 67 - Comparison between the UAV DSM and LiDAR DEM outputs from the hydrodynamic model for the year 2100 and scenario RCP8.5 for a 100-year return period storm surge event.....	89
Figure 68 - MOHID water flooded areas by year for with a 100-year return period storm surge on UAV DSM and RCP8.5 scenario.	90
Figure 69 - Flooded buildings identified by the bathtub model for the year of 2100 by scenario for a 100-year return period storm surge event over the UAV DSM. A) RCP4.5. B) RCP8.5.....	91
Figure 70 – Flooded roads identified by the bathtub model for the year of 2100 by scenario for a 100-year return period storm surge event over the UAV DSM.	92
Figure 71 – Roads by flood hazard class obtained by the bathtub model over UAV DSM for two different storm surge events in 2020. A)50-year return. B) 100-year return period.....	93
Figure 72 – Buildings by flood hazard class obtained by the bathtub model over UAV DSM for a 50-year (left) return period storm surge and 100-year (right) return period for 2020.....	94
Figure 73 – Detail of the overlay of ATLAS’ (Government of Northwest Territories, 2021) “Flood_Risk” layer and the year 2020 bathtub model result for a 100-year return period storm surge as affected buildings by hazard class.....	95

Figure A 1 - Driftwood uppermost limit derived from the UAV orthophotomaps, manually digitized and vectorized as linear features.	111
Figure A 2 - Flood and coastal erosion affected locations, comments and historical water heights identified by the staff of Hamlet of Tuktoyaktuk (Courtesy of Calvin Pokiak – unpublished).	112
Figure A 3 – MOHID Grid data (5 x 5 m) of the UAV DSM combined with the bathymetry derived from Tuktoyaktuk Harbour nautical chart, rendered in ArcGIS Pro.....	113
Figure A 4 - MOHID Grid data (5 x 5 m) of the LiDAR DEM combined with the bathymetry derived from Tuktoyaktuk Harbour nautical chart, rendered in ArcGIS Pro.....	113
Figure A 5 - Differences and overlapped extents of the bathtub model with a sea level rise scenario RCP8.5 for UAV and LiDAR with all hazard classes grouped for the year 2100.	114
Figure A 6 - MOHID flooded areas for 2020, 2060 and 2100 for the RCP4.5 scenario with a 50-year return period storm surge on UAV DSM.....	115
Figure A 7 - MOHID flooded areas for 2020, 2060 and 2100 for the RCP4.5 scenario with a 50-year return period storm surge on LiDAR DEM.....	116
Figure A 8 - MOHID flooded areas for 2020, 2060 and 2100 for the RCP8.5 scenario with a 50-year return period storm surge on LiDAR DEM.....	117
Figure A 9 - MOHID flooded areas for 2020, 2060 and 2100 for the RCP4.5 scenario with a 100-year return period storm surge on LiDAR DEM.....	118
Figure A 10 – MOHID flooded areas by year for with a 100-year return period storm surge on UAV DSM and RCP4.5 scenario.	119
Figure A 11 - MOHID flooded areas for 2020, 2060 and 2100 for the RCP8.5 scenario with a 100-year return period storm surge on LiDAR DEM.	120
Figure A 12 - Flood depth for the RCP4.5 scenario and a storm surge event with a 50-year return period on UAV DSM.....	121
Figure A 13 - Flood depth for the RCP8.5 scenario and a storm surge event with a 50-year return period on UAV DSM.....	122
Figure A 14 - Flooded buildings by model for the year 2100 and scenario RCP4.5 with a 50-year return period storm surge event on UAV DSM. A) Bathtub. B) MOHID.	123
Figure A 15 - Flooded roads by model for the year 2100 and scenario RCP4.5 with a 50-year return period storm surge event on UAV DSM. A) Bathtub. B) MOHID.	123

VI. List of Tables

Table 1 – Modelled return periods of peak storm water levels (m above CD) calculated by Manson & Solomon (2007).....	31
Table 2 – Probability range and hazard classes used for mapping. Adapted from Antunes et al. (2019).	48
Table 3 – Gauge height sampling point data summary used for Chart Datum conversion.	59
Table 4 – Average storm surge water level by return period with a 95% confidence interval.	65
Table 5 – Gumbel distribution summary output.	66
Table 6 – UAV DSM bathtub model inputs used for the sea level rise simulations by scenario, all SD values are in m.	74
Table 7 – UAV DSM hydrodynamic model water level inputs and outputs for the sea level rise simulations by scenario.	74
Table 8 –LiDAR DEM bathtub model inputs used for the sea level rise simulations by scenario, all SD values are in m.	74
Table 9 – LiDAR DEM hydrodynamic model water level inputs and outputs for the sea level rise simulations by scenario.	74
Table 10 – UAV DSM bathtub model inputs used for the sea level rise and a 50-year return period storm surge by scenario.	80
Table 11 - UAV DSM bathtub model inputs used for the sea level rise and a 50-year return period storm surge by scenario.	81
Table 12 – LiDAR DEM bathtub model inputs used for the sea level rise and a 50-year return period storm surge by scenario.	81
Table 13 - LiDAR DEM hydrodynamic model water level inputs and outputs for the sea level rise and a 50-year return period storm surge by scenario.	81
Table 14 – UAV DSM bathtub model inputs used for the sea level rise and a 100-year return period storm surge by scenario.	87
Table 15 – UAV DSM hydrodynamic model inputs used for the sea level rise and a 100-year return period storm surge by scenario.	87
Table 16 – LiDAR DEM bathtub model inputs and outputs used for the sea level rise and a 100-year return period storm surge by scenario.	87
Table 17 – LiDAR DEM hydrodynamic model inputs and outputs used for the sea level rise and a 100-year return period storm surge by scenario.	87
Table A 1 - GPS points used to determine the RMSE of the UAV DSM.	109
Table A 2 - GPS points used to determine the RMSE of the LiDAR DEM.	110

VII. List of Abbreviations

CD – Chart Datum

CGVD2013 – Canadian Geodetic Vertical Datum of 2013

CGVD28 - Canadian Geodetic Vertical Datum of 1928

DEM – Digital Elevation Model

DFO – Fisheries and Oceans Canada

DSM – Digital Surface Model

GIS – Geographical Information Systems

GSC – Geological Survey of Canada

HAT – Highest Astronomical Tide

IPCC – Intergovernmental Panel on Climate Change

LiDAR – Light Detection and Ranging

MHAT – Mean Highest Astronomical Tide

MSL – Mean Sea Level

NOAA – National Oceanic and Atmospheric Administration

NRCan – Natural Resources Canada

RMSE – Root Mean Squared Error

SD – Standard Deviation

SLR – Sea Level Rise

UAV – Unmanned Aerial Vehicle

1. Introduction

1.1. Problem Characterization

Arctic warming is leading to an accelerated reduction in sea ice. For the year 2100, models predict a reduction in the Arctic sea ice area from 43 to 94% in September and from 8 to 34% in February (IPCC,2021). The increase of the sea-ice free season duration translates in additional exposure of the coastline to wave action. This thesis focuses on the Beaufort Sea coastal Hamlet of Tuktoyaktuk (Northwest Territories, Canada). Regions in the northern hemisphere at higher latitudes will be more affected by climate change than lower latitude regions (Räisänen, 2001). The predicted reduction in sea ice (Johannssen et al., 2002) translates in a longer period for storms to erode the coastline. According to Johannssen et al. (2002), the expected increase in temperature during summer leads to the melting of ice-bounded sediments in coastal cliffs.

The Beaufort Sea coast consists of unconsolidated sediments which makes it an exceptionally dynamic environment vulnerable to marine processes such as wave action, tides, storm surges, and ice push, as well as permafrost degradation processes, such as thermoerosion and thaw subsidence (Harper, 1990).

For coastal settlements, the risk of storm-surge flooding associated with sea level rise is of major concern. Satellite data shows that the global mean sea level has been increasing at a rate of 3 ± 0.4 mm per year between January 1993 and July 2020 (NOAA, 2021), and in Tuktoyaktuk, with a rate of 2.75 ± 1.07 mm per year, from 1961 to 2020, based on detrended tide gauge data (NOAA, 2021). According to the Intergovernmental Panel on Climate Change (IPCC), the mean sea level is expected to rise more than 1 m, by 2100, mainly due to thermal expansion of the oceans and increased melting of land ice (IPCC, 2021; Church et al., 2013a), leading to an increase in storm surge frequency.

Tuktoyaktuk, depicted in Figure 1, is located in a low-lying area in the Kugmallit Bay, where severe coastal erosion destruction has been continuously documented (Danard et al., 2003; Solomon, 2005). The main cause of coastal erosion along the coast of Tuktoyaktuk is wind-induced storm surge events that are most frequent during late summer (Manson and Solomon, 2007; Jones et al., 2009).

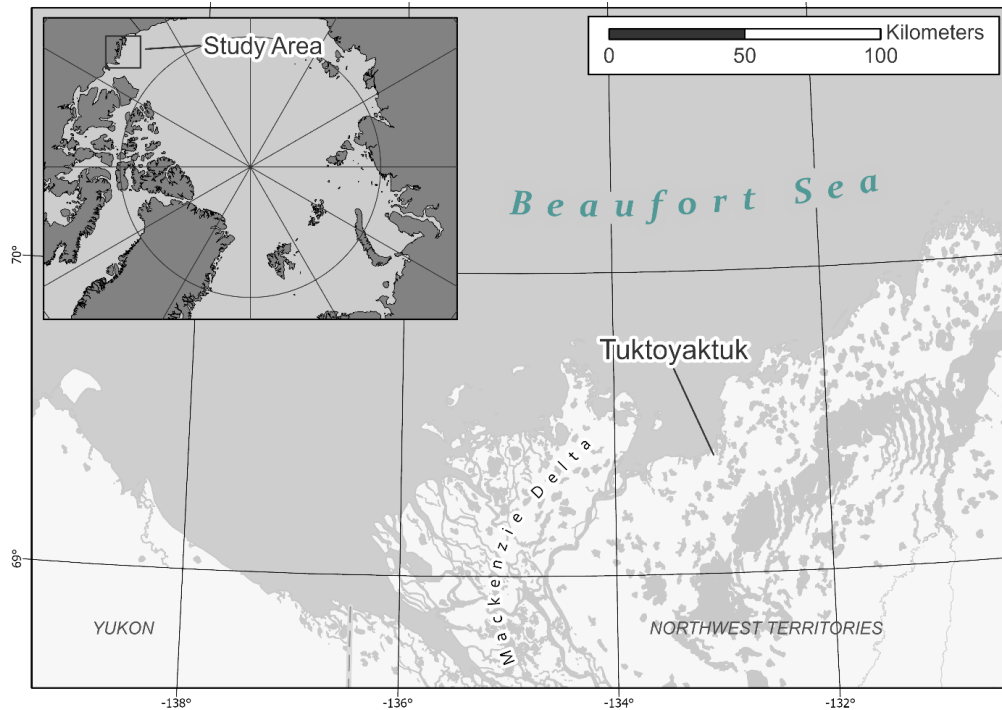


Figure 1 – The Beaufort coast showing the location of Tuktoyaktuk.

Storm surge exposes the settlements in coastal areas to flooding and structural destruction. Accurate and understandable forecasts, and inundation mapping products play important roles in preparing for and mitigating these events, including flood protection and evacuation. As a storm surge event happens, the sea leads to a rise in water level at the coast that can be extremely severe, as seen in Figure 2.



Figure 2 – Storm surge event in Tuktoyaktuk that took place in the 4th of August 2019 where the wave run-up reached several buildings located near Flagpole Point.

The present rates of cliff erosion are projected to increase due to sea level rise, thaw of permafrost, and the increase in frequency of severe coastal storms during the open-water season, that is becoming longer. Measures to control coastal erosion in Tuktoyaktuk have been implemented over the past years but the effect of sea level rise translates in the need of continuously monitoring, maintenance and possibly, the

construction of new structures to mitigate erosion. The identification of areas prone to flooding is of major interest to support climate change adaptation and mitigation before Tuktoyaktuk becomes permanently uninhabitable.

1.2. Objectives and Methodology

The objective of this thesis is to produce and analyse the implications of ultra-high-resolution inundation maps that incorporate the IPCC Fifth Assessment Report (AR5) sea level rise projections for the scenarios RCP4.5 and RCP8.5, for the years of 2060 and 2100 and storm surge events with 50-year and 100-year return periods in Tuktoyaktuk, Northwest Territories, Canada.

Two different models are used to identify flooded areas, a GIS-based bathtub model , and a hydrodynamic model, the MOHID Water. The models use two different elevation datasets for comparison: i: the most recent ultra-high-resolution surface model, surveyed with a senseFly eBee Plus in 2018, and ii. a LiDAR elevation model surveyed in 2004.

1.3. Structure of the Thesis

The thesis is divided in six chapters. The first, an introduction, serves as a characterization of the problem addressed, the objectives of the study and presents a brief description of the methodology used.

The second chapter refers to the state of the art and the theoretical knowledge required to understand the processes covered in this thesis, followed by an in-depth characterization of the study area in chapter three.

The methodology and a detailed description of the datasets and models used are contained in the fourth chapter.

The flood assessment and mapping are described in the fourth chapter, where the elevation data used, and sea level rise scenarios are explained.

Chapter five is dedicated to the analysis and discussion of the results, followed by the conclusion and suggestions for future works, included in chapter six.

2. State of the Art

As global warming and sea level rise in the Arctic accelerate (Comiso, 2003) and sea ice decreases (Barber and Hanesiak, 2004), impacts are expected to affect land further away from the current shore, increase in flood frequency and the salinization of thermokarst lakes. The expansion of the open water season and permafrost degradation (Jorgenson et al., 2006) translated in major increases in coastal erosion rates in the Arctic, namely in the Beaufort coast, where the rates are among the world's highest (Solomon, 2005; Jones et al. 2009).

According to the IPCC report (IPCC 2021) air temperature is “very likely” to continue increasing in the Arctic and sea ice cover to diminish. Drobot and Maslanik (2003) and Simmonds et al. (2008) indicate that coastal erosion will also increase in the Arctic because of higher temperatures and reduced sea ice coverage. More specifically, Manson and Solomon (2007), Jones et al. (2009), Gunther et al. (2013) and Hynes et al. (2014), point the Beaufort coast as one of the regions most affected by the phenomena.

Models that aim to replicate water surface can use many variables as inputs depending on the complexity of the scenario to be modelled. In this study, to assess the areas prone to coastal flooding caused by storm surge events combined with the effects of climate change, represented by sea level rise, variables such storm surge and predicted sea level rise water levels at a local scale are fundamental to both modelling approaches.

This chapter covers the theoretical background and state of the art of the essential building blocks of modelling used in this study, coastal dynamics, and identification of limitations in the context of this research.

2.1. Sea Level Rise Projections

One of the most substantial effects of climate change is sea-level rise (Stern, 2007; IPCC, 2013). The global mean sea level rise is depicted in Figure 3 and indicates that, by the year 2100, it is possible that it exceeds 1 m (IPCC, 2013; Meehl et al., 2007; Church et al., 2013a). The large uncertainty range of global sea level (Milne et al., 2009) is explained by the different assumptions regarding future carbon emissions result in different sea level predictions.

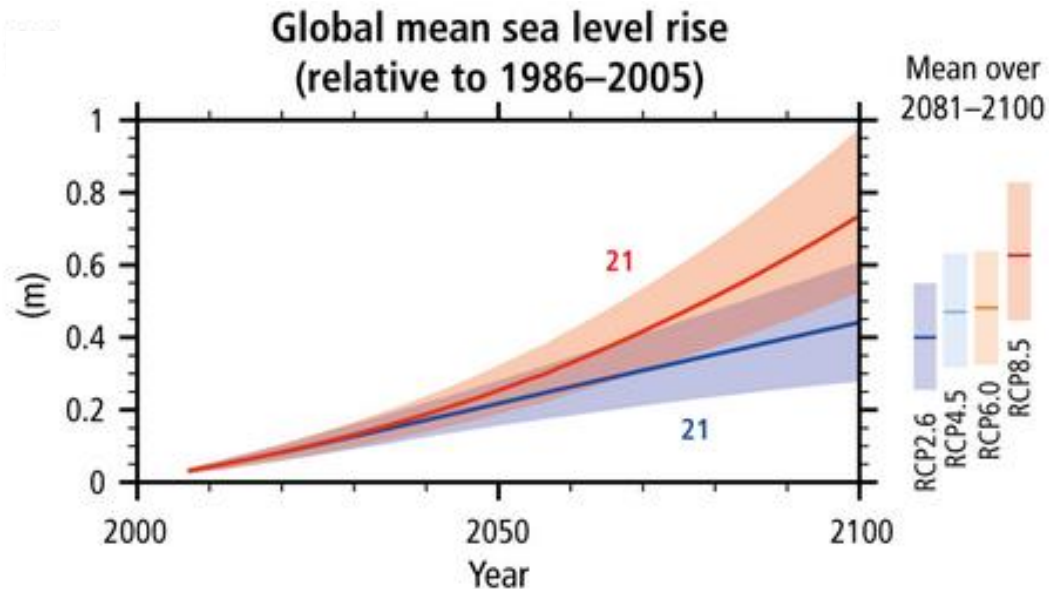


Figure 3 - Time series of global annual change in mean surface temperature for the 2006–2100 period (relative to 1986–2005) from Coupled Model Intercomparison Project Phase 5 (CMIP5) concentration-driven experiments. Projections are shown for the multi-model mean (solid lines) and the 5% to 95% range across the distribution of individual models (shading). Grey lines and shading represent the CMIP5 historical simulations (IPCC, 2013).

These projections are based in different contributions, such as thermal expansion of the ocean, surface melting and ice discharge from mountain glaciers and ice caps and from the Greenland and Antarctic ice sheets. Smaller contributions are also included, such as groundwater usage and water entrapment by dams. The possibility of a swift degradation of the West Antarctic ice sheet represents another level of significant uncertainty regarding the future projections of sea level rise (IPCC, 2019; Church et al., 2013a). Relative sea level is the change in sea level relative to the solid surface of Earth and it depends on various factors in addition to the projected global sea level such as local vertical motion, spatial variations of the distribution of glacial meltwater and ocean dynamics (James et al., 2014). The scenarios used in this thesis are established on the Representative Concentration Pathways (RCP) scenarios (Moss et al., 2010) as described in the Fifth Assessment Report (AR5) of the IPCC: RCP4.5 and RCP8.5. These scenarios represent different greenhouse gas concentration pathways where the number in each name corresponds to the net radiative forcing in $W\ m^{-2}$ at 2100. The net radiative forcing is the difference between the energy that enters Earth's atmosphere and the quantity that is radiated out of the system. The change in sea level at a given location depends on its distance to the source of meltwater and Canada possesses considerable mountains and ice caps, mainly in the west and northeast. The proximity to Greenland's ice sheet, the mountain glaciers of the Coast Mountains and the Gulf of Alaska raises the significance of the effects of sea level rise (James et al., 2014). Vertical land motion affects projections of relative sea level. Land uplift diminishes the effect of sea level rise, and even surpasses it, but land subsidence contributes to its aggravation. In Canada, the surface is uplifting and subsiding at various rates and varying across the country, as seen in Figure 4, due to the effects of the last continental glaciation isostatic rebound. In western

and northern Canada and surrounding regions, recent and present-day changes in ice mass also generate significant crustal motion. This effect is particularly noticeable in Alaska and Greenland, where the highest uplift rates were registered. (James et al., 2014).

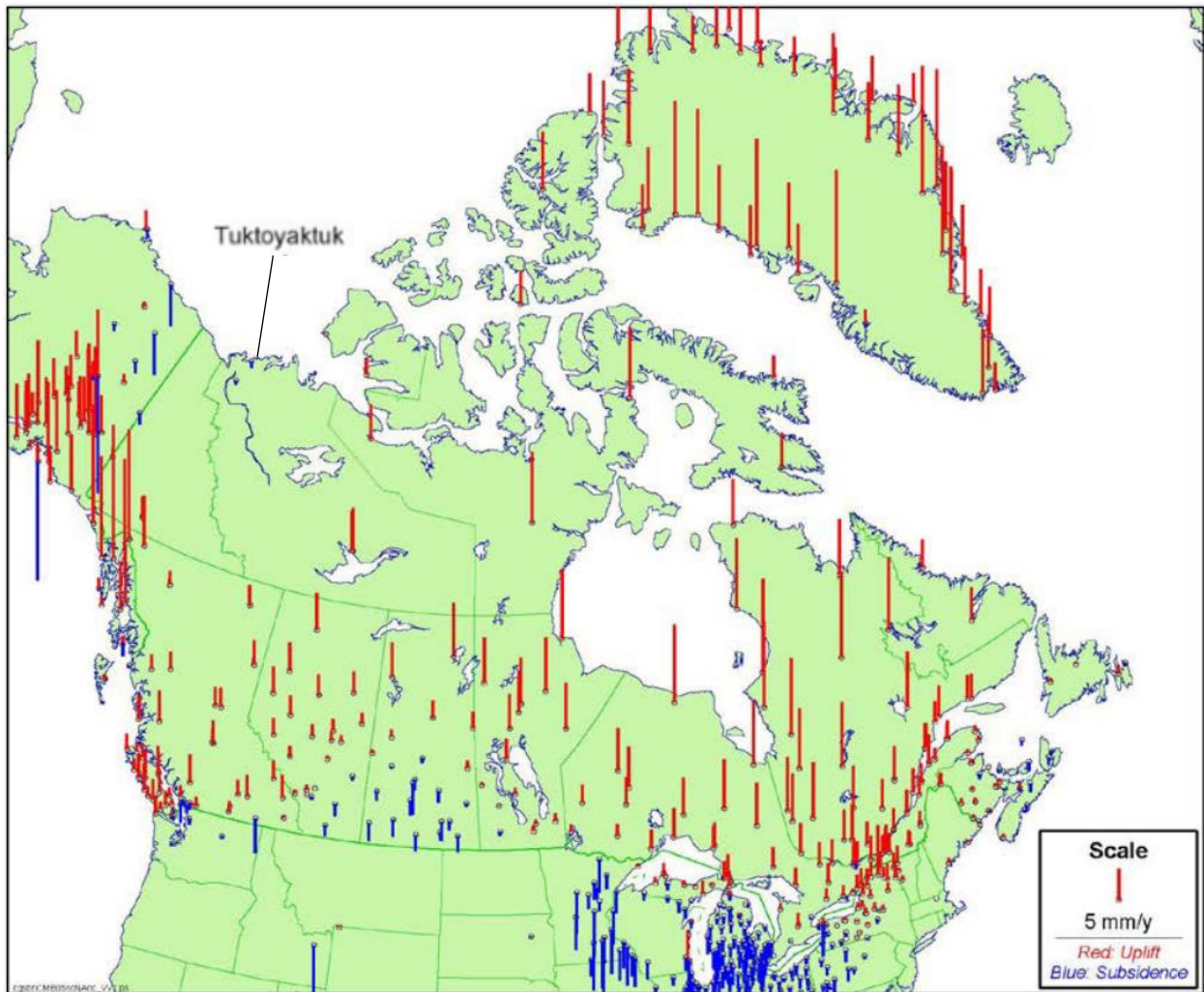


Figure 4 - Derived vertical crustal motion from GPS for Canada and surrounding regions (Craymer et al., 2011).

According to James et al. (2014), Tuktoyaktuk is projected to experience a relative sea level rise, at, or close to the global mean for the year of 2100.

2.1. Storm Surges

A storm surge is defined as the difference between the observed water level and the level predicted for the astronomical tide. Surges are caused by atmospheric low-pressure systems and high winds associated with storms that pushes water onshore. The storm surge water level height depends on the orientation of the coastline compared to the storm track, the intensity, size and speed of the storm and local bathymetry. (NOAA, 2021) A schematic representation of a storm surge water level can be seen in Figure 5.

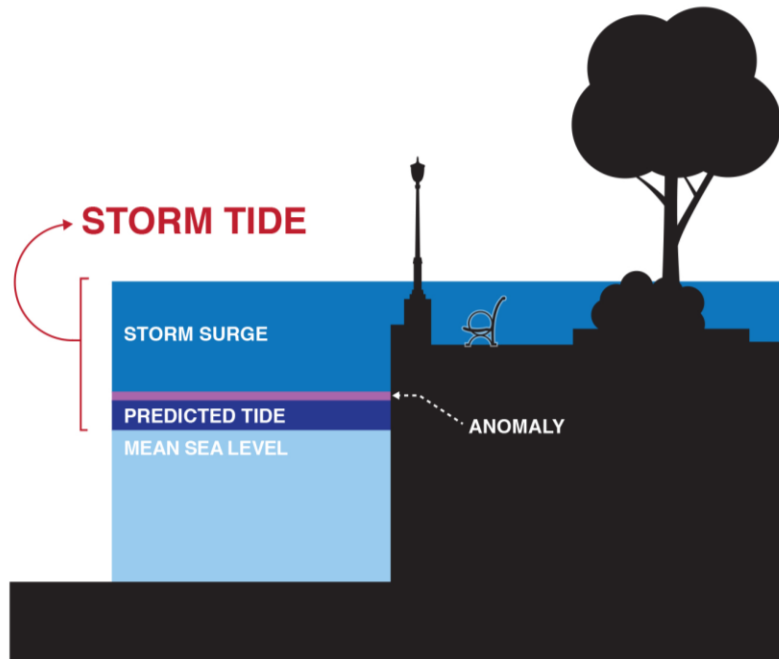


Figure 5 - Storm surge schematic representation. (NOAA, 2021)

Storm surge should not be confused with storm tide. Storm tide is the combined water level rise of both storm surge and the astronomical tide (NHC, 2021). The increase in water height can lead to severe flooding in coastal areas, especially when a storm surge coincides with the normal high tide (McLean et al., 2001).

Sea level rise associated with increased storm surges will impact coastal communities in many ways (Hinkel et al., 2013). In Arctic coastal regions severe ocean storms are frequent and intense (Terenzi, Jorgenson and Ely, 2014; Manson and Solomon, 2007) with surges ranging between 1.5 – 3.7 m along the Beaufort and Chukchi Sea coasts (Hume and Schalk, 1967; Reimnitz and Maurer, 1979). Storm surges are amongst the most devastating natural disruptions affecting Arctic coastal communities (Brunner et al., 2004). Together with reduced sea ice extent (Serreze et al, 2007), the increase in fetch and wave action (Overeem et al., 2011; Lintern et al., 2011), storm severity is expected to increase, translating in larger, more frequent storm surges (Manson and Solomon, 2007).

2.2. Coastal Erosion

About 34% of Earth's coasts are affected by permafrost, yet only 35% of these coasts in the Arctic are lithified and the remaining 65% unlithified and hence, particularly vulnerable to coastal erosion (Lantuit et al., 2012). Coastal erosion is especially effective in coasts with excess ground ice due to the thermal influence of sea water and the volume loss upon thaw. Permafrost coastal erosion is limited to a few months a year, the ice-free summer season, and during this period, erosion rates can be similar to or higher than those of temperate regions (Overduin et al., 2014). According to Lantuit et al. (2012), the average Arctic coastal erosion rate is 0.5 m yr^{-1} and 3% of the Arctic coastline is retreating at a rate higher than 3 m yr^{-1} .

Extreme 25 m erosion events were reported by Jones et al. (2009) in one year at Drew Point, an ice-rich site located on the Alaskan Beaufort Sea coast. Regionally, the highest erosion rates are observed along the Beaufort and East Siberian coasts, where bluffs of unlithified and ice-rich material are exposed and where cliff heights are generally low (Overduin et al., 2014). Extreme erosion rates can take place in a short period at specific locations (Dallimore et al., 1996; Barnhart et al., 2014), while average erosion rates for longer coastal segments or long observation periods are generally much lower (Solomon, 2005). Storminess, waves and storm surges, duration of ice-free season, sea level and sea surface temperature are the regional factors acting on a larger scale, while local factors controlling erosion are related with sediment properties, such as cohesiveness and grain size, cryostratigraphy and geomorphology (cliff height and slope, exposure, underwater slope, presence of spits and barrier islands and coastal hinterland topography) (Solomon, 2005; Jones et al., 2009). The importance of the sea-ice free season, exposure to wave action and sea water temperature were studied by Barnhart et al (2014) in the Alaskan Beaufort Sea. Günther et al. (2015) focused on the importance of the temporal synchronism of open water with warm summer air temperatures in the southern Laptev Sea.

3. Characterization of the Study Area

3.1. Regional Setting

The Tuktoyaktuk Peninsula, Figure 6, is a 40 km wide peninsula that stretches northeast for 160 km from Tuktoyaktuk to Cape Dalhousie. The peninsula lies within the zone of continuous permafrost with a permafrost thickness from 200 m to over 600 m (Judge et al., 1987; Burn and Kokelj, 2009). It is characterized by poorly drained areas that typically contain polygonal terrain and organic soils (Kokelj et al., 2014; Steedman et al., 2016). Rolling, ice-rich irregular mounds of glacial debris are locally frequent (Aylsworth et al., 2000). The peninsula is rich in lakes and water bodies with depths that can exceed two-thirds of the winter ice thickness (Burn, 2002). The drainage of these lakes causes permafrost to build up and the presence of lake sediments (Mackay, 1992), provides a nutrient-rich soil for shrubs to colonize (Marsh et al., 2009). The vegetation is characterized by dwarf-shrub tundra along the whole peninsula (Timoney et al., 1992).

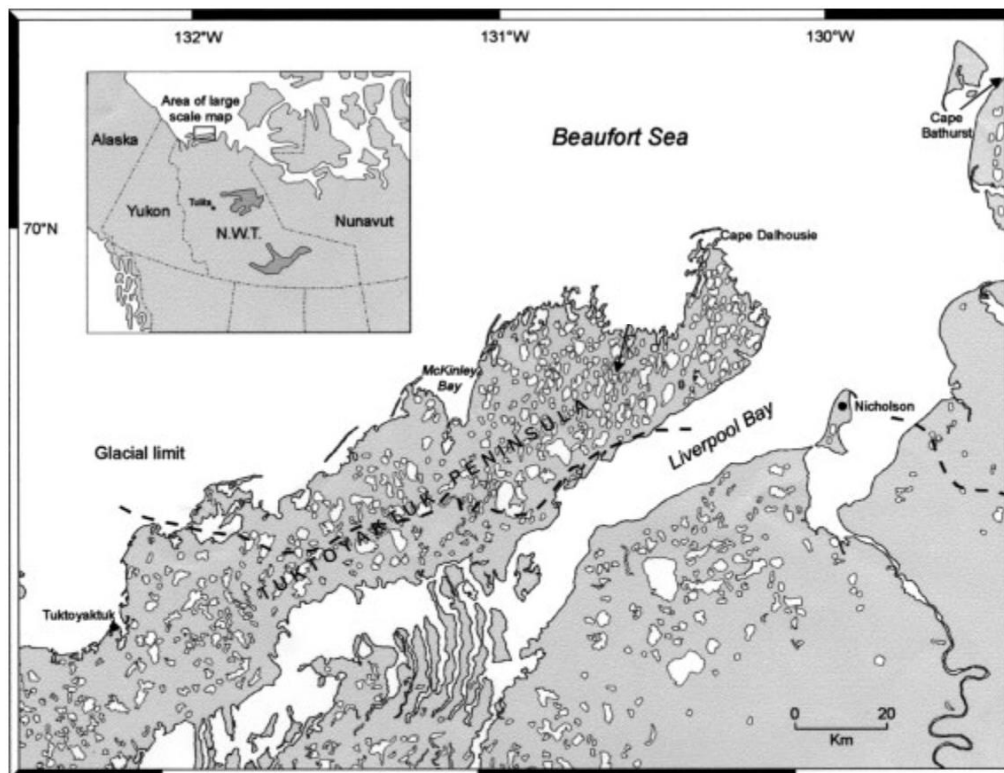


Figure 6 – The Tuktoyaktuk Peninsula area (Côté and Burn, 2002).

The region is characterised by colder and drier conditions near the coast with warmer and wetter conditions inland. The mean annual air temperature for 1981-2010 at Tuktoyaktuk was -10.1 ± 1.3 °C, a mean annual snowfall of 103.1 cm and 74.9 mm of mean annual rainfall (Environment Canada, 2021). The wind regime in Tuktoyaktuk is bimodal during late summer with higher frequencies of north-westerly and south-easterly

winds (Solomon, 2005; Manson and Solomon, 2007; Atkinson, 2005; Hudak and Young, 2002). Increasing air temperatures registered since the 1970s have been associated with an increase in permafrost temperatures (Smith et al., 2005; Burn and Kokelj, 2009; Burn and Zhang, 2010).

The bathymetry of the Beaufort Sea is shown in Figure 7. The region is characterized by very shallow nearshore seaward slopes surrounding Tuktoyaktuk Peninsula and the Mackenzie Bay with coast-parallel isobaths and a very low gradient. The most notable slopes start occurring past the 50 m isobath as the distance to shore increases (Wolfe et al., 1998).

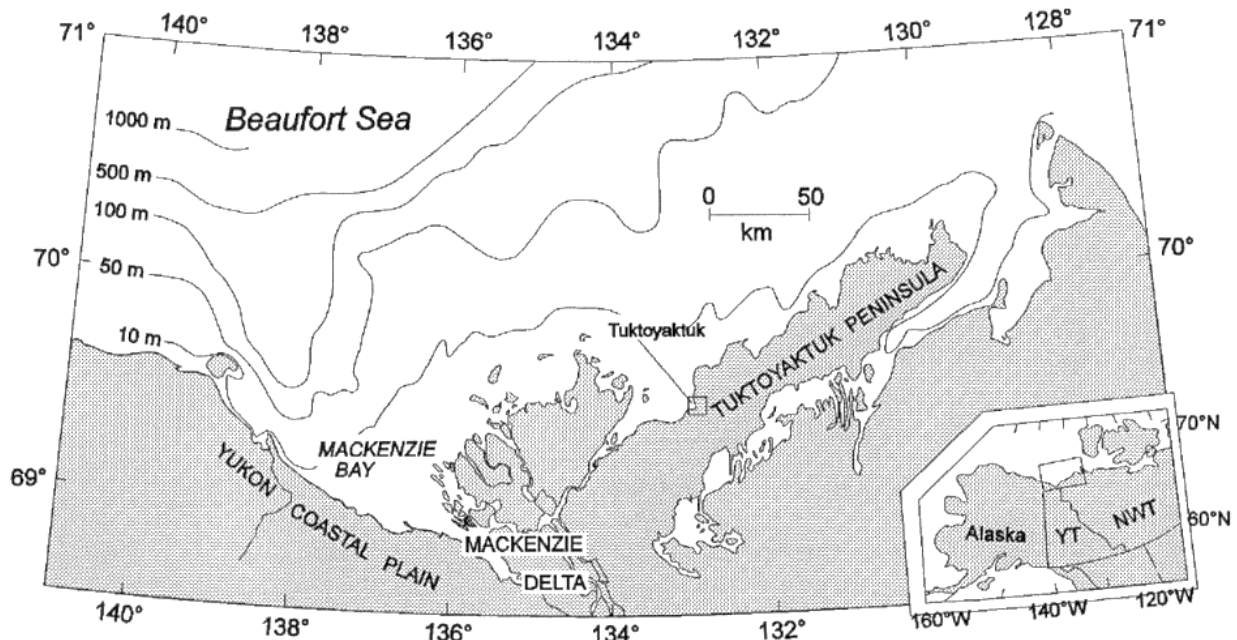


Figure 7 – Bathymetric contours surrounding Tuktoyaktuk Peninsula (Wolfe et al., 1998)

Offshore sea ice is present for approximately 9 months of the year, preventing wave action and coastal processes. Sea ice limits the open-water season to approximately 3 months, from mid-July to mid-October. The occurrence of offshore sea ice limits wave action even during the open water season, meaning that the Beaufort Sea has relatively low wave-energy (Harper, 1990). Tidal currents are often slow, with speeds under 15 cm s^{-1} for more than 90% of the time (Fissel and Birch, 1984). The currents in shallow waters close to the coast are assumed to be principally wind driven (Harper, 1990). The tide amplitude in the Beaufort Sea ranges from 0.3 m for neap tides and 0.5 m for spring tides. Storm surges caused by strong winds are frequent and surveys of log debris indicate storm surge water height of 2.4 m above mean sea level in Tuktoyaktuk (Harper et al., 1998). Coastal communities are most vulnerable if a storm surge peaks during a high-tide event. Tuktoyaktuk's average seasonal cycle is described by highest tides occurring from May to September, corresponding to the open-water months.

3.2. Characteristics of the Hamlet of Tuktoyaktuk

The Inuvialuit Hamlet of Tuktoyaktuk, located in Tuktoyaktuk Peninsula (Figure 7), has 995 inhabitants (Northwest Territories Bureau of Statistics, 2021) and is the most northern community on the mainland. Its name in Inuvialuktun means “resembling a caribou”. The hamlet was formerly known as Port Brabant, and nowadays is commonly abbreviated to “Tuk”. In 1934 the Hudson’s Bay Company selected this site as an alternative to Herschel Island and as the most suitable harbour in the region for transshipping freight brought by barge down the Mackenzie River to bigger ships for distribution along the Arctic Coast. During the 1950s the decline in fur prices and the beginning of the Distant Early Warning (DEW) Line construction triggered a population shift from the surrounding areas to Tuktoyaktuk. In the 70s and 80s, oil exploration originated massive changes in the community by making large numbers of people transition to a wage-earning economy. The oil and gas industry started to decline in the late 80s, originating a high level of unemployment. Nowadays, limited employment is available through private business and government services. Tourism during summer provides seasonal employment to a few people, especially after the construction of the Dempster Highway in 2017 that brought Tuk closer to Inuvik and strengthened its access to the South (Community of Tuktoyaktuk, 2008). Before the construction of the Dempster Highway, Tuk was only accessed by sea, a winter road or by airplane. Tuktoyaktuk’s infrastructure comprise the Mangilaluk School, providing education up to the 12th grade, a community hall (Kitti Hall), and several recreational facilities, such as a swimming pool and a gymnasium and a health centre. The municipal infrastructure includes a fire hall, sanitation by door-to-door truck and a gravel road system (NWT Bureau of Statistics, 2013). The Tuk area contains two large pingos (small hill in Inuvialuit), a dome-shaped mound with a layer of soil over a large core of ice, and is the entry point for Pingo Canadian Landmark, a protected area that extends for approximately 16 km² and includes Canada’s highest pingo at 49 m. The peninsula on which the Hamlet of Tuk is located, is composed mostly of glaciofluvial sands, typically 2 to 3 m thick, and underlain by massive ground ice (Rampton and Bouchard, 1975). The tundra landscape and near-shore are characterized by sparse but varied flora and fauna, including many species crucial to the community livelihood and diet, such as caribou, bears, muskox, fox, geese, ducks, seals, whales, and fish (Carmack and Macdonald, 2002; Manson et al., 2005). Figure 8 shows the spatial distribution of the buildings located in the study area (approximately 2 km²) and the boundaries for flood modelling and mapping in this study.

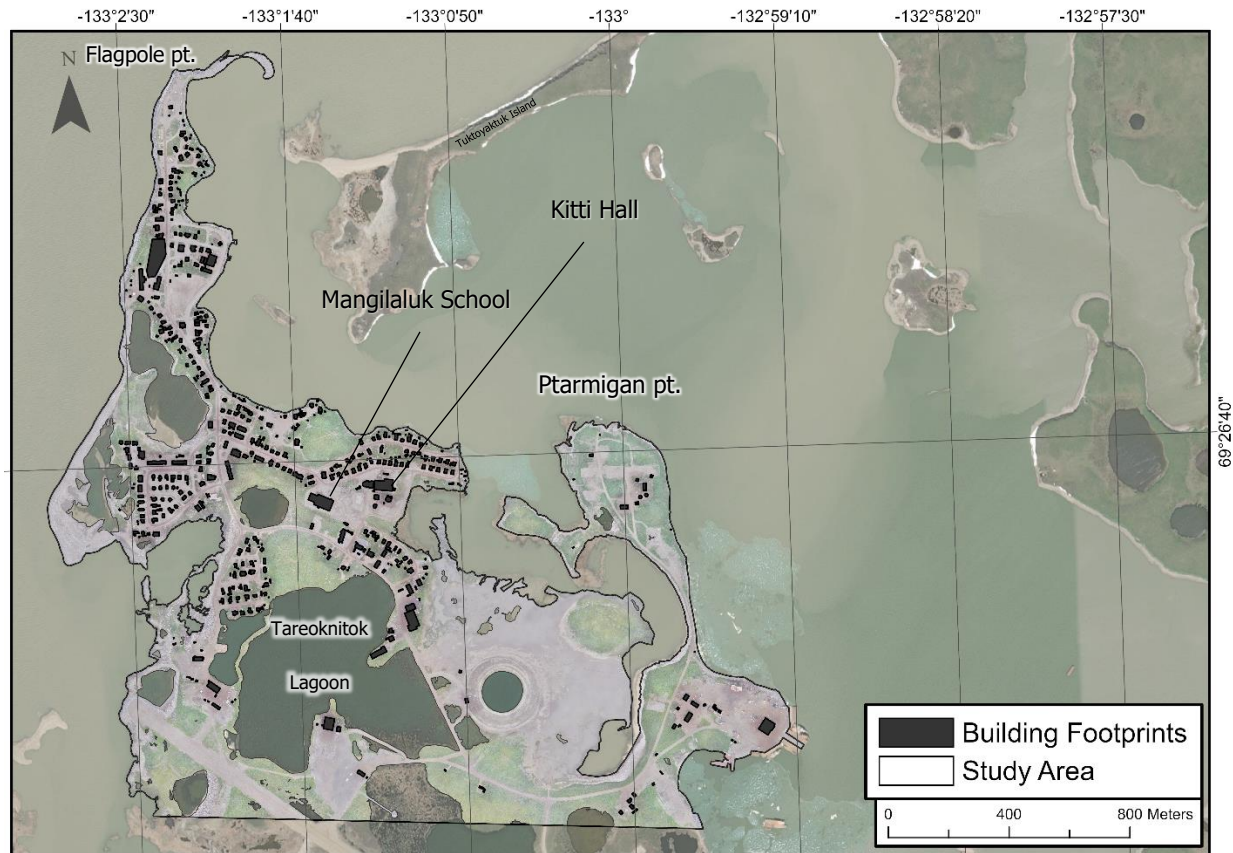


Figure 8—Study area boundary and spatial distribution of the assessed buildings extracted from NWT Administration of the Territorial Land Acts System (ATLAS) (Government of Northwest Territories, 2021). Imagery Sources - Basemap: ESRI, Study area: 2018 UAV Orthophotomap.

3.3. Coastal Erosion and Flooding in Tuktoyaktuk

According to Solomon (2005) the Tuktoyaktuk Peninsula is characterized by coastal retreat rates of 0.7 to 0.8 m yr⁻¹. The Hamlet of Tuktoyaktuk, which has a long history of coastal erosion issues related with the high content in ground ice, shows rates from 1 to 2 m yr⁻¹ in areas without artificial shore protection. Tuktoyaktuk is one of the best-equipped coastal settlements of the western Canadian Arctic, regarding not just quantity but variety of infrastructure and services due to past military presence and oil industry (Couture et al., 2002). According to Johnson et al. (2003), the Longard tubes built in 1976 resulted in a successful protection but were destroyed in 1981. In 1987 (Aveco, 1986) a shoreline reclamation program was undertaken, and the sandbag system constructed provided protection until 1993, when a strong storm removed over 50% of the installed protection. Values of 4 to 8 m of shoreline retreat were recorded along the coastline and the north and south spits were washed over. In 1998, forty concrete slabs were constructed (Trillium, 1997), protecting approximately 100 m of coastline and still functioning nowadays. Predictions of the shoreline position were formulated by Solomon (2002) based on the historical retreat rate before the construction of the current protection measures, the physical characteristics of the standing protection systems and partition of the erosion area into segments with similar physical features. The

proposed shoreline positions for 10 and 25 years are represented in Figure 9. It is important to note that this study was done almost 20 years ago and that the present erosion rates are higher than the ones used by Solomon (2002), implying that the proposed erosion estimates could represent a conservative approach for the present situation.

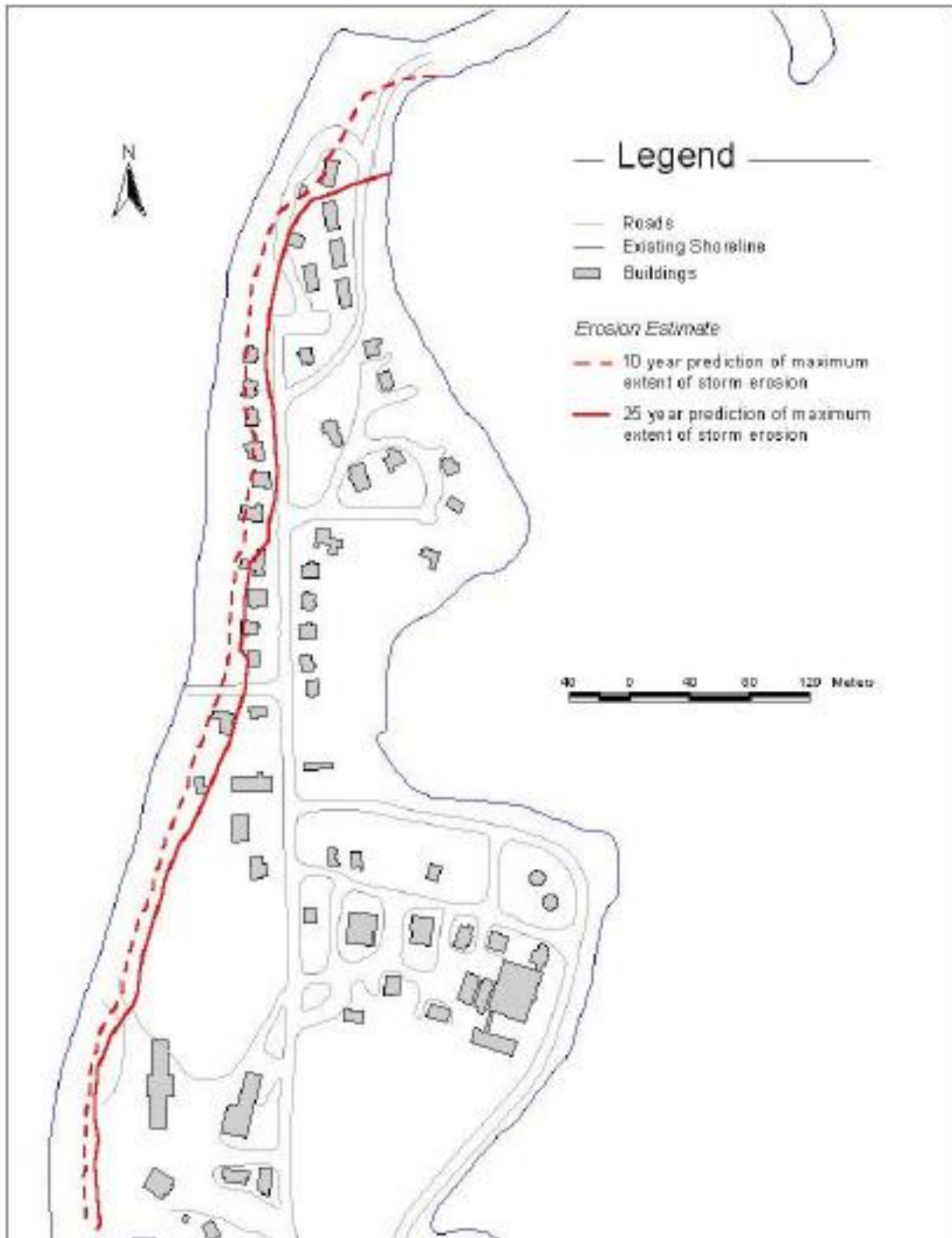


Figure 9 - Coastal erosion progression estimates (Johnson et al., 2003).

The latest higher erosion rates are possibly attributable to the increase in frequency and extremity of storm surges (Brown et al., 2003) due to changes in fetch, combined with the diminishing of sea ice, sea level rise and increases in sea surface temperature (Jones et al., 2009a) and air temperature (Günther et al., 2013b). The severe coastal erosion rates and uncertainty regarding the future positioning of the shoreline, changes in seabed topography and local wave dynamics are issues that directly impact the process of inundation mapping for longer periods of time. Consequently, there is a high demand for models and information that accurately identify areas at risk for such events in the future, as a basis for sustainable shoreline management, urban planning and development of adaptation and mitigation strategies (McLean et al., 2001). Occasional storm surges in the Beaufort Sea have been identified as potential hazard to the coastal structures (Department of Public Works, 1971; Henry, 1975; Henry & Heaps, 1976; Reimnitz & Maurer, 1978, 1979), where water levels of 2 to 3 m above mean sea level (MSL) were registered inundated considerable areas of low-lying tundra. These surges occur mostly during late summer (Harper et al., 1988). Henry (1974) studied storm surge events higher than 0.9 m for between 1962 and 1973. The frequency of severe surges was not distributed evenly in time and the highest water level ever registered by Tuktoyaktuk's tide gauge occurred on October 4, 1963. This event was observed at Barrow, Alaska, one day earlier, where the sea level rose 3 m above MSL, becoming the highest level ever observed at Barrow. Frequency and magnitude of storm surge occurrence is normally documented through the analysis of long-term tidal records. However, tidal records for Tuktoyaktuk extend back only to 1961 (Figure 10), with some significant gaps between 1981 to 1991 and 1992 to 2003, and the largest known surges, with water levels of approximately 3 m above MSL and winds up to 40-50 m/s that occurred in 1944 and 1970 (Reimnitz et al., 1979), are not part of the record.

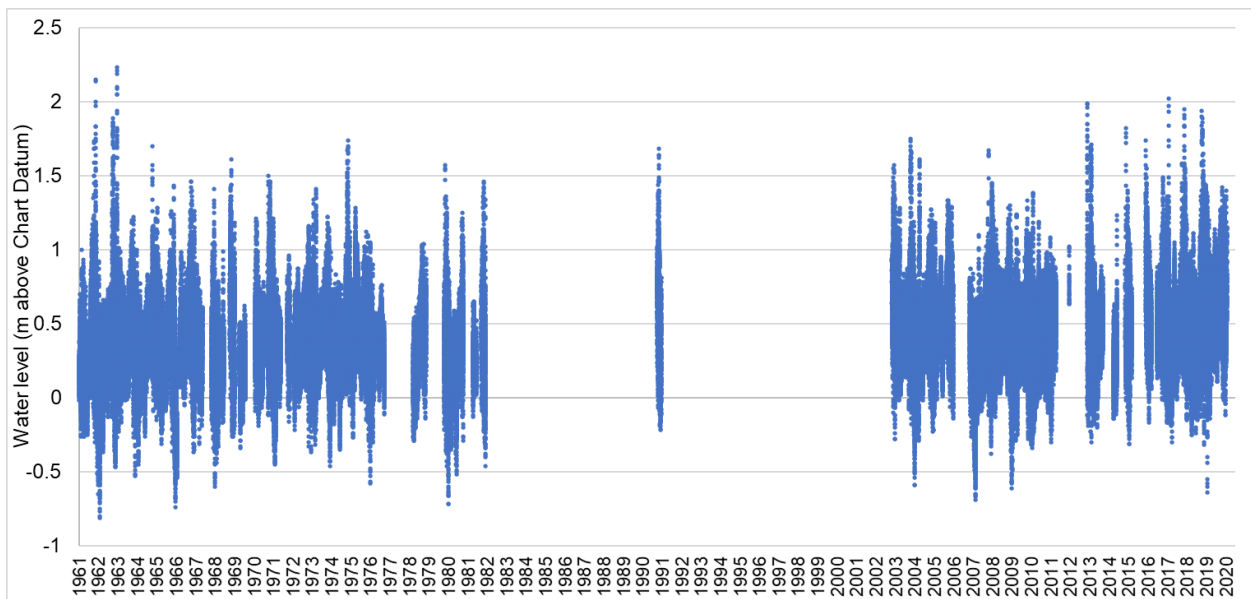


Figure 10 – Open-water season hourly water level data extracted from Tuktoyaktuk tide gauge.

An insufficient number of extreme surges have been logged to precisely estimate return periods, crucial for flood mapping. Henry (1984) suggests that an alternative approach is to use numerical models that incorporate wind stresses and pressure gradients as the driving forces, but information on extreme winds over the Beaufort Sea is very limited and field observations of water height are essential to validate the results. Manson & Solomon (2007) studied historical records of wind speeds and directions, water levels, sea-ice extent, and temperature changes to understand variability in past storm surge events and used climate modelling to predict future changes of the Beaufort Sea shorelines. The predicted increase in peak storm wind speeds lead to higher water levels, beach migration and more extreme flooding. The results of the predicted return periods of peak storm water levels are summarized in Table 1 and provide a benchmark for the storm water levels derived in this study.

Table 1 – Modelled return periods of peak storm water levels (m above CD) calculated by Manson & Solomon (2007).

Return Period (years)	2000	2050	2100
2	1.77	2.08	2.53
5	2.00	2.31	2.76
10	2.16	2.47	2.92
25	2.36	2.67	3.12
50	2.51	2.82	3.27
100	2.65	2.96	3.41

Winter surges also occur (Solomon et al., 2009), causing pressure ridge development, ice scour, breakup of ice roads and potential flooding. The phenomenon, called ice push, combined with winter surges can reach land posing risk to human life and infrastructure. In this study, only open water season storm surges were included to derive design return periods and to produce inundation maps.

4. Data and Methods

4.1. Introduction

The methodological process used for this study is summarized in Figure 11. Initially, to create the base data for modelling, the Global Navigation Satellite System (GNSS) real time kinematic (RTK) data acquired in the field during the summer of 2019 was processed and imported to GIS. Features such as water bodies, culverts and the shoreline were digitized in ArcGIS Pro using the 2018 UAV footage, and the LiDAR elevation datasets added to the geodatabase. Infrastructure data was obtained from Administration of the Territorial Land Acts System (ATLAS) map viewer (Government of Northwest Territories, 2021), a Government of Northwest Territories open geodatabase and the nautical chart used to derive bathymetry, from the Canadian Hydrographic Service. The data used for harmonics and storm surge water level analysis was gathered from Fisheries and Oceans Canada (DFO) and processed in Microsoft Excel and MATLAB and it was then combined with the IPCC local sea level rise predictions to create the simulated RCP4.5 and RCP8.5 scenarios. The collected and processed data was used for the two modelling approaches, in ArcGIS Pro for the bathtub model, and in MOHID Studio for the hydrodynamic model MOHID Water.

In a final stage, the water surface outputs from both models for the years of 2020, 2060 and 2100 were overlayed with the infrastructure data in order to identify buildings and roads affected by the different scenarios of flooding.

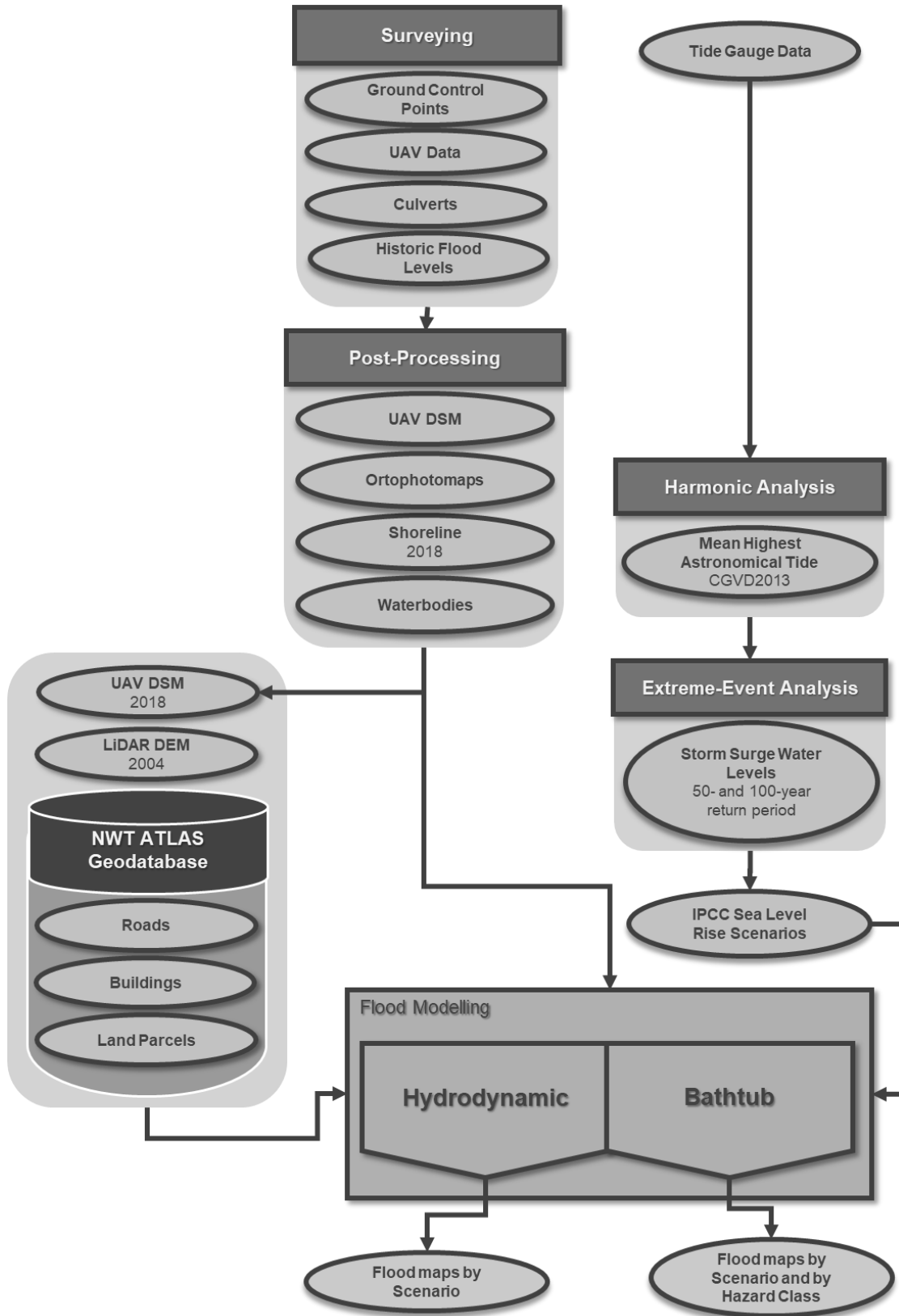


Figure 11 – Methodology flowchart.

4.2. Topographic Data

Elevation models are considered as one of the most important spatial datasets in many geographical information systems (GIS). The most used terms in literature are digital elevation model (DEM), digital terrain model (DTM) and digital surface model (DSM). Although the distinction between the terms is not clear and agreed on, some doctrines may apply. A DEM represents a “bare” land surface model, free of trees, buildings and other features that considered non-ground. A DSM is an elevation model that contains everything that is surveyed. It contains buildings, canopy, and the ground, if not covered. The DTM is a more generic term referring to a DEM that can include terrain morphology, flow and drainage patterns, and soil properties (Li et al., 2005).

Formulation of flood hazard and inundation mapping is one of the examples of preparedness phase in disaster management, by lowering possible impacts to coastal communities and providing information on how to react during flooding events (Khan et al., 2008). Identifying flooding extents and how deep the flooded area is, is required in coastal flood management and flood damage assessment. To assemble this information, elevation data that accurately represents earth’s surface is one of the key components for precise flood investigations.

Casas et al. (2006) demonstrated that the accuracy of the output of any flood model was highly dependent on the digital elevation model (DEM) quality by evaluating the effects of different DEM sources on flood modelling in terms of outputs such as inundation extents and the elevation of water surface. Thus, it is critical to know which elevation sources could provide higher vertical accuracy and spatial resolution before the selected DEM is used for the assessment of flood hazard risk (Li et al., 2010).

4.2.1. Airborne LiDAR

Li et al. (2010) showed that LiDAR proved to be an efficient method for obtaining terrain data with high resolution as compared to other sources of elevation data. According to Sampson et al. (2016), LiDAR DEMs are considered, nowadays, the most reliable terrain models used in flood modelling and the most used ones. LiDAR sensors are complex sensors for the acquisition of 3D data used for creating topographic models. They can be used during night-time or in low light conditions, with shadows or clouds and extremely versatile in tree-covered areas. This technology is composed by a sensor that emits a signal to the target object, measures the travelled time and the intensity of the returned signal, and a receiver that detects the reflected signal of the pulse, its positioning and navigation systems (GNSS) (Baltsavias, 1999; Wehr and Lohr, 1999). In Canada, a study conducted by Webster et al. (2006) used two LiDAR systems to generate high-resolution DEMs to identify areas prone to coastal flooding and erosion and possible socioeconomic and ecosystem impacts of sea level rise and storm surge events at the New Brunswick coast, this is an area highlighted in a national study by Shaw et al. (1998) as being vulnerable to sea level rise. The flood inundation and flood depth were validated by field visits to compare the results with the water levels observed during a flood event in January 2000, with the results showing that the flood extent and depth

were accurate within 10 to 20 cm. Another study using LiDAR technology in flood mapping in North Carolina, from Bales et al. (2007), achieved a difference between the measured and simulated water levels of less than 25 cm, with a LiDAR DEM with approximately 20 cm of vertical accuracy. Many other successful applications of lidar DEMs in storm surge flood risk mapping on Prince Edward Island, Canada, are published, such as McCulloch et al. (2002) and Webster et al. (2001; 2003; 2004a; 2004b).

In this study, the LiDAR DEM used was provided by the Geological Survey of Canada and it was surveyed in 2004 using a manned aircraft, producing a model with 1 m of spatial resolution. The DEM, defined on the Canadian Geodetic Vertical Datum of 1928 (CGVD28) was converted to the modernized vertical datum of CGVD2013, represented in Figure 12, using the ArcGIS Pro transformation tool. After the transformation, the LiDAR dataset was 31 cm higher (average). Véronneau (2014) studied the vertical transformation from CGVD28 to CGVD2013 across Canada, obtaining a value of -32 cm for Tuktoyaktuk.

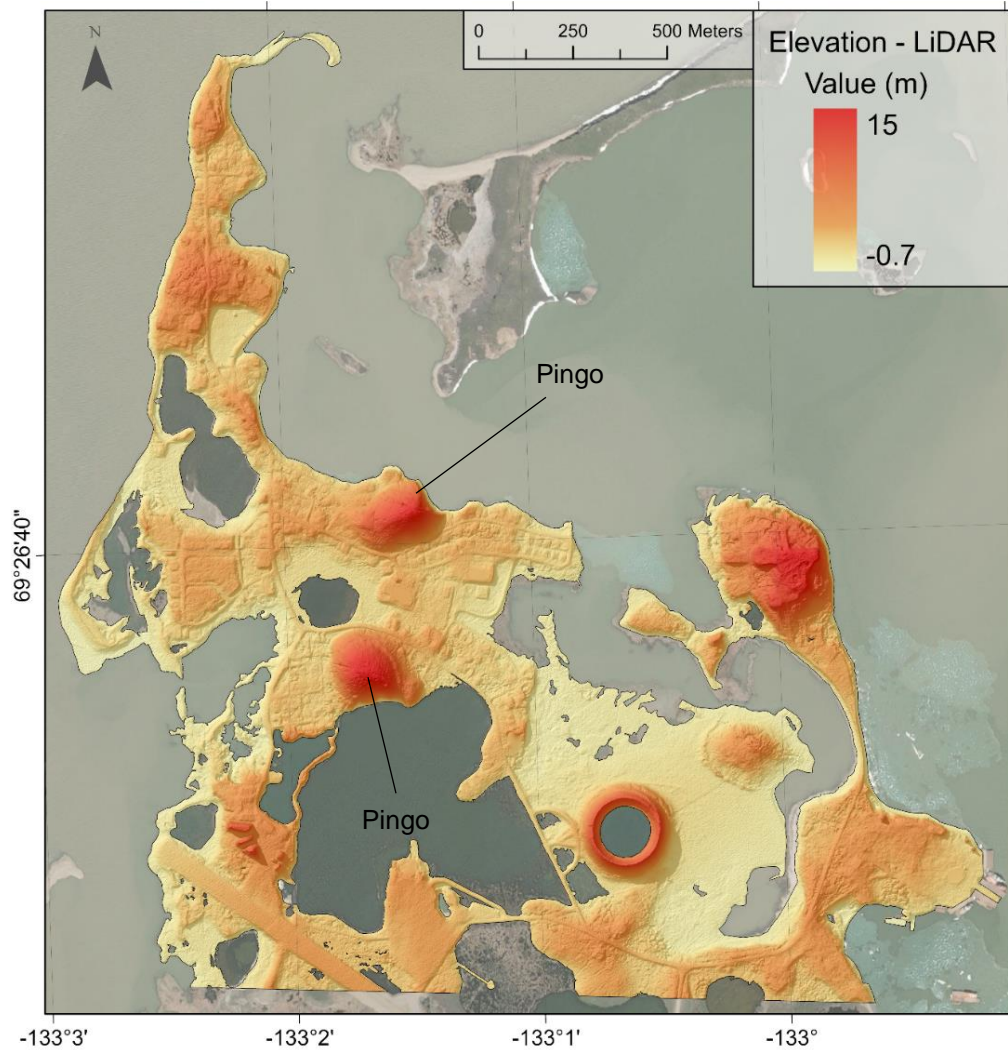


Figure 12 - 2004 LiDAR DEM of the study area in CGVD2013 and a spatial resolution of 1 meter.

4.2.2. UAV Digital Surface Model

Manned airborne platforms such as airborne LiDAR, provide both high spatial resolution and rapid sweeping times, but in practice, their use is limited by operational and logistical intricacy, safety, and high cost. It becomes feasible over medium to large areas and it remains constrained, mostly, to commercial operators. Technological advancements in UAVs created an alternative surveying method that allows capturing spatial, spectral, and temporal data with relatively small investments. Drones provide higher versatility, adaptability and flexibility compared to manned airborne platforms or satellites and can be quickly and repeatedly deployed for ultra-high spatial resolution and high temporal resolution (Pajares et al., 2015). A successful and efficient survey requires well-timed data, and the high versatility of UAVs makes them ideal tools for frequent elevation and imagery acquisition at very fine scales, and targeted surveying of rapid changes such as extreme flood events, coastal erosion, and hydrological processes. The significant cost reduction of UAVs and sensors, and current developments in processing software and computing power led to a swift expansion in drone applications in the last decade (Giordan et al., 2020; James et al., 2019). The recent developments in RTK technology for GNSS used in UAVs results in faster surveying and more accurate models with centimetric to decimetric resolutions even in large survey areas (Favalli et al., 2018). Some studies addressed the use of UAVs in environmental surveying and modelling, in particular on water flow modelling. Successful applications of UAV derived DEM as topographic input for rainstorm modelling is shown in Backes et al. (2019) and flood modelling to replicate real flood events in Mourato et al. (2017) and Langhammer et al. (2017), where limitations were found mostly in tall, highly vegetated areas, which is not the case in our study area. UAVs were used for water surface detection after a flood event by Hashemi-Beni et al. (2018). Schumann et al. (2018) compared the accuracy of a UAV-derived structure from motion (SfM) DEM, such as the one used in this study, with a LiDAR DEM and assessed its reliability for flood mapping using a bathtub approach. The results showed that both elevation models generated accurate inundated areas with less than 30 cm difference between models. Annis et al. (2020) reached a 98 % flood extension matching from UAV-DEM (0.25 m resolution and ± 0.1 m vertical accuracy) flood maps compared to 72 % obtained from a LiDAR DEM with 1 m resolution and 0.15-0.3 m vertical accuracy.

Tuktoyaktuk's high-resolution DSM and orthophotographic maps were obtained by digital photogrammetry methods linking image matching and SfM algorithms. In this study, the UAV used was a fixed wing (96 cm wingspan) eBee Plus from Sensefly. The surveys took place on the 2nd and 3rd of August 2018 where a 4.6 km² area was covered with a spatial resolution of 0.1 m. The UAV was equipped with a senseFly S.O.D.A camera with a F/2.8-11, 10.6 mm (35 mm equivalent: 29 mm) RGB lens with a resolution of 20 MP, The UAV data processing was done in Pix4D Mapper Pro using an AMD Ryzen 9 3900X 12-Core CPU with 64 GB of RAM and a Nvidia GTX 1060 Ti to perform feature detection, image matching and modelling using Pix4D's disclosed SfM algorithms. The average ground sampling distance (GSD) was 2.32 cm, the number of calibrated images 5020 out of 5955 (due to large areas with water) with 4 ground control points and a total of 12 independent checkpoints with a mean error of 0.17 m in Z. The fast-changing nature and spatial variability of environmental processes occurring in Tuktoyaktuk requires data of corresponding high

spatial and temporal resolution. The UAV SfM DSM produced after processing and corrected with ground control points (GCPs) is shown in Figure 13.

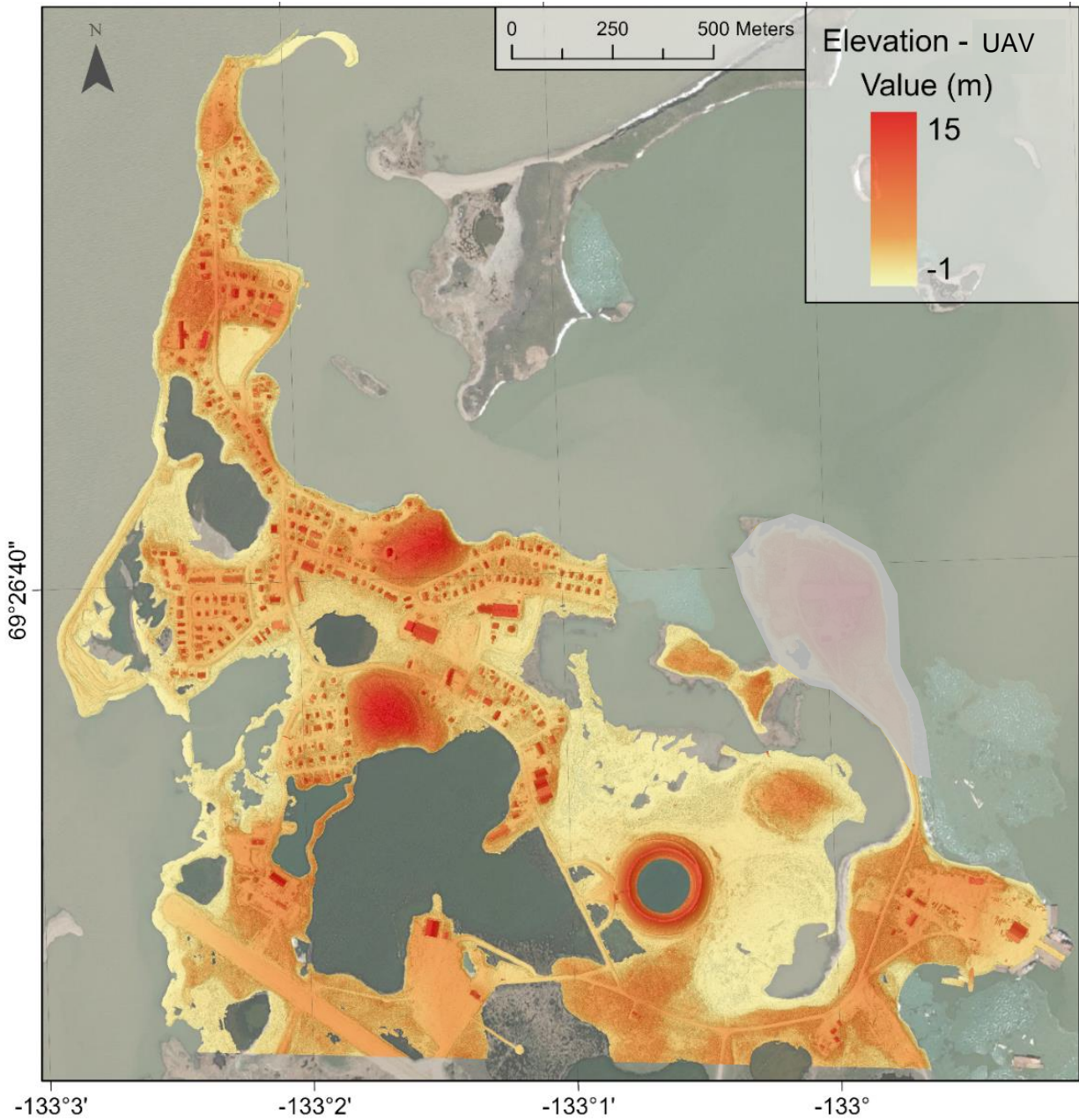


Figure 13 - DSM derived from the UAV flights and used for modelling with a cell size of 0.1 by 0.1 m.

4.2.3. Field Survey of Culverts

The surveyed culverts are represented in Figure 14. The height coordinate provided by the RTK GNSS system with a precision of approximately 3 cm in x, y and z, and the diameter measured in-situ was used to interpolate each culvert profile. It was assumed that all surveyed culverts allow the flow of water despite the condition of many was impossible to assess due to the presence of debris obstructing the section.

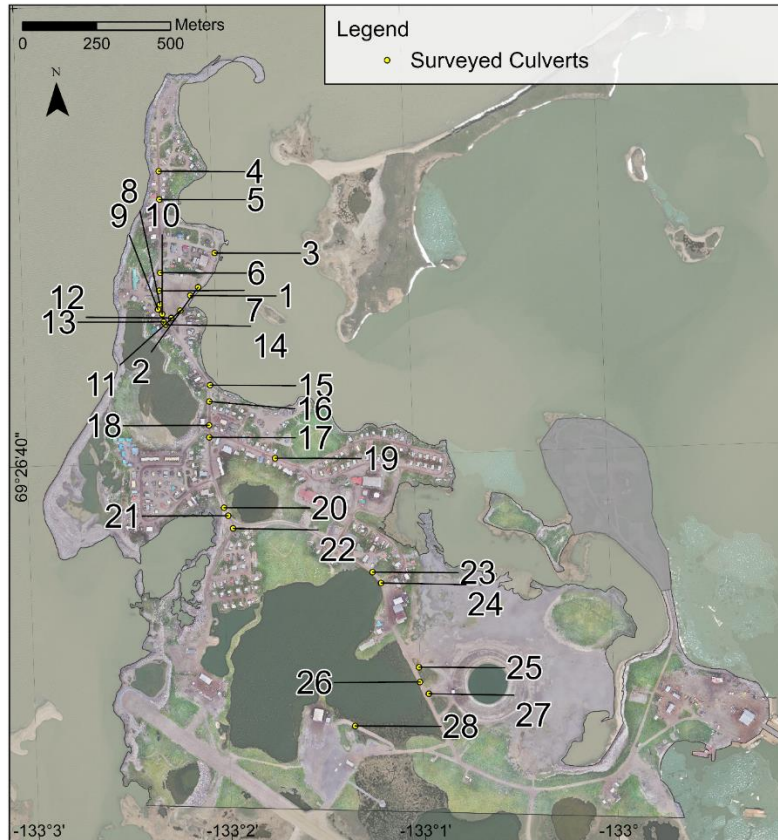


Figure 14 – Location of all the surveyed culverts included in both models.

Figure 15 shows the importance of including the culvert system in the flood modelling of Tuktoyaktuk. The visible flooded area would not be included in the model output if the surveyed culvert system was not implemented in the models.

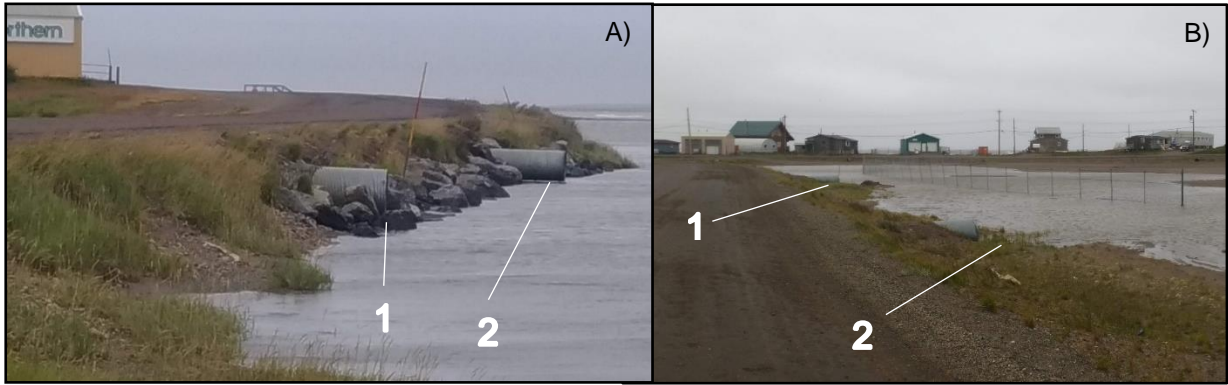


Figure 15 – Culverts 1 and 2, representing the connectivity of an area that was previously considered as unconnected in the DEMs without the incorporation of the culvert system. A) Facing North. B) Facing South.

The culverts' profiles were generated with the Trend interpolation tool in ArcGIS Pro. The geometry only reflects the diameter and length of the pipe, resulting in a projected surface in a rectangular shape. Figure 16 shows the original UAV DSM surrounding culverts 1 and 2 and a picture taken during a storm event that shows the water flowing and connecting the inner area with the sea. The changes are also visible in Figure 17, where the profile of culvert 1 is represented in detail and compared with the original elevation. This process was replicated for the elevation datasets used in MOHID after the resampling to 5 x 5 m cell size that would, otherwise, cause the generalization of the culvert features leading to the loss of connectivity.

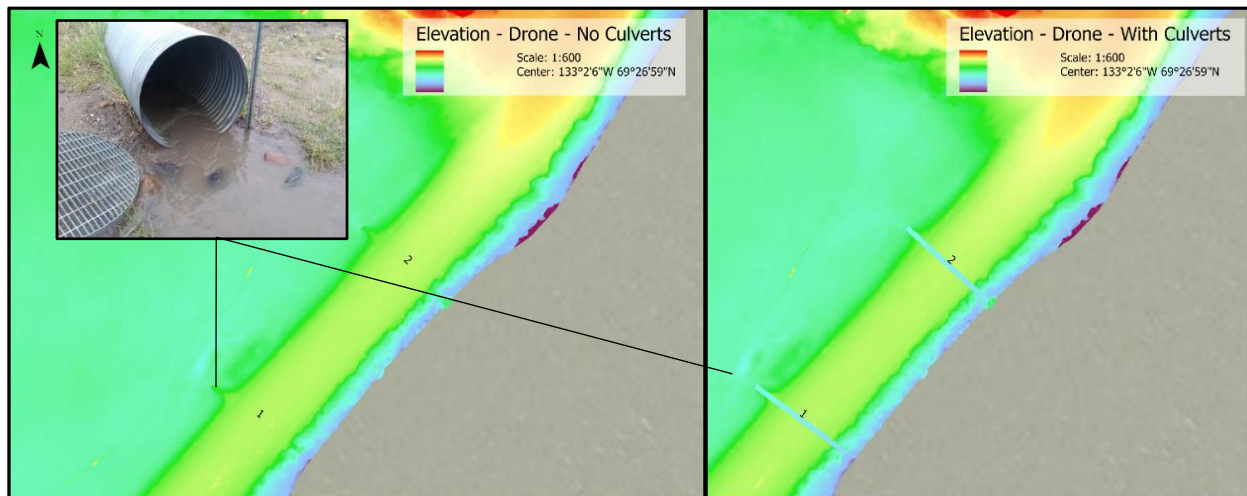


Figure 16 – Original UAV DSM with two of the surveyed culverts. Note that the topography of the culverts is visible in the DSM.

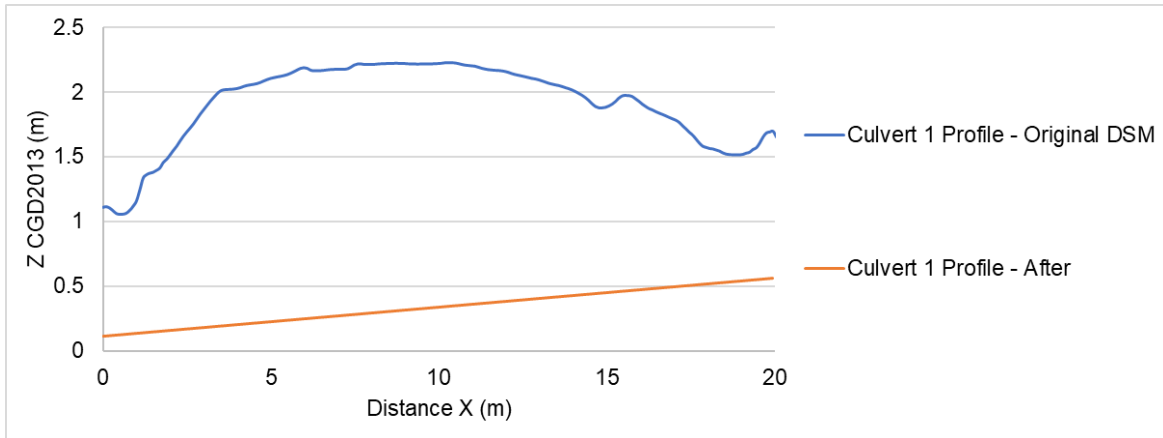


Figure 17 – Elevation changes after the implementation of linear interpolation for Culvert 1.

4.3. Tide Data and Storm Surge Assessment

The map in Figure 18 shows the location where the predicted sea level rise (SLR) scenarios data from (Church et al., 2013) used in this thesis was extracted. This location was selected because it was the closest available data to the study area. The sea level rise data used is represented in Figure 19. It is possible to see that the average values for both RCP scenarios, and its confidence intervals starts diverging more significantly after the year 2040. In 2100, the uppermost limit of the 95% confidence interval for scenario RCP8.5 indicates a threatening sea level rise of 0.95 m surrounding Tuktoyaktuk.

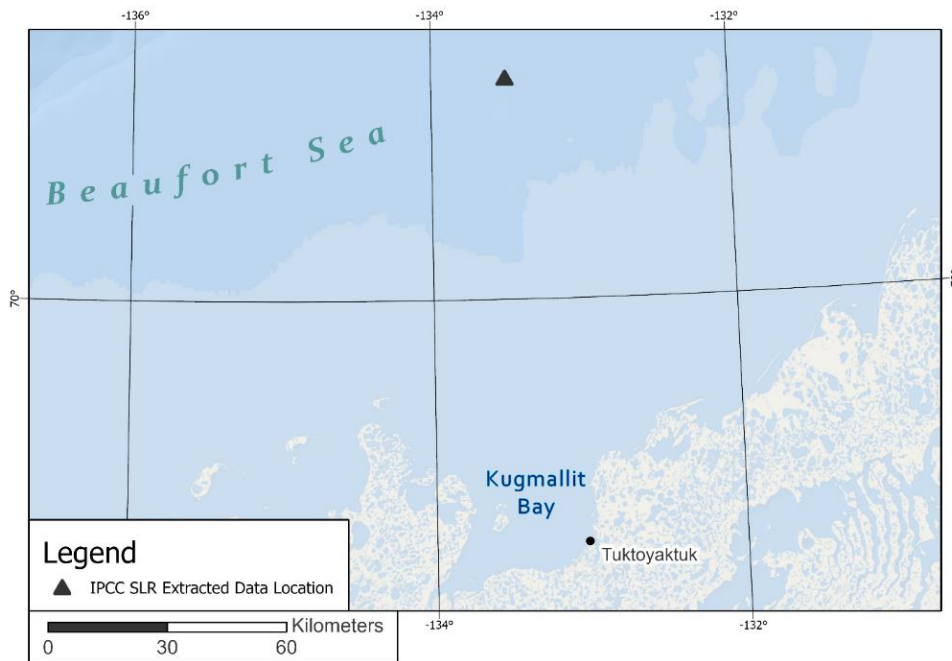


Figure 18 – Location of Tuktoyaktuk relative to the IPCC sea level rise data predictions sampling point from <https://icdc.cen.uni-hamburg.de/las/getUI.do> (Church et al., 2013).

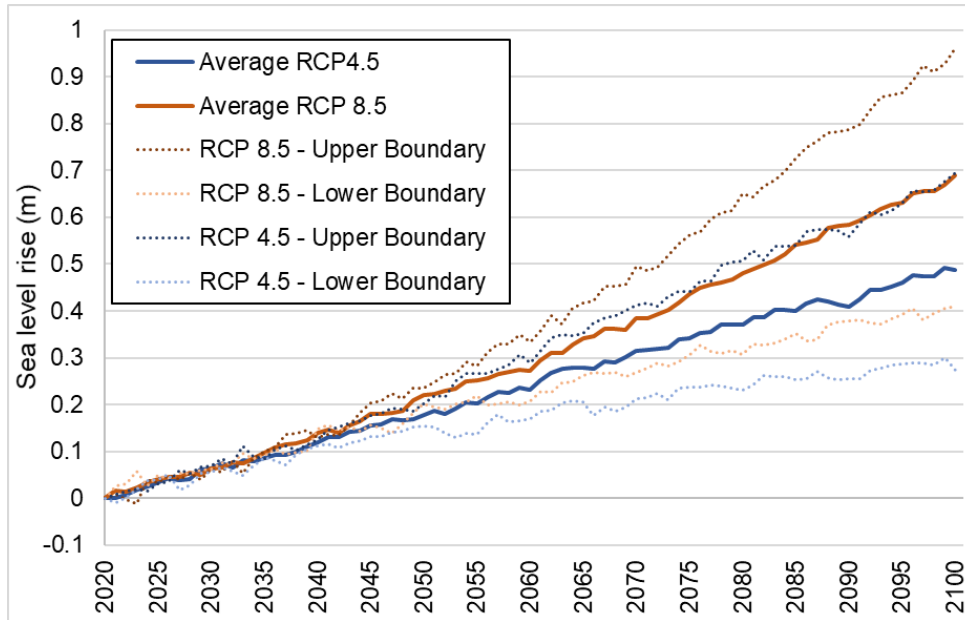


Figure 19 – Predicted sea level rise based on IPCC Scenarios RCP4.5 and RCP8.5 with a confidence interval of 95% relative to 1986-2005 for Tuktoyaktuk – extracted at 70.5 N; 133.5 W from <https://icdc.cen.uni-hamburg.de/las/getUI.do> (Church et al., 2013).

The contribution of land subsidence registered in Tuktoyaktuk is of 1.68 mm year⁻¹ (James et al., 2014), corresponding to approximately 17 cm in 100 years, but this process is not considered in the sea level rise projections in this thesis, due to the uncertainty regarding how the phenomenon affects spatially the study area. On top of the SLR scenarios two storm surge return periods were included in the flood analysis, a 50-year return period and a 100-year return period. To calculate the return periods, it was necessary to isolate the water level records from Tuk's tide gauge into their three components: mean sea level (MSL), astronomical tide and non-tidal residual (Pugh, 1987), by performing a harmonic analysis. For the harmonic analysis, only the years with 50% or more of completion data were used to estimate tide harmonics, as suggested by Parker (2007). The software package used in MATLAB was UTide (Codiga, 2021) tool. Since the harmonic function of degree zero reflects the MSL, estimated yearly, by subtracting the modelled harmonics output from the tide gauge hourly data, the resulting non-tidal residue is detrended of the SLR (Vieira et al., 2012). This process was applied to all the available water level time series of hourly data, for the open water season, in order to extract the yearly maximum of the non-tidal residual that corresponds to the storm surge water level. The yearly maximum storm surge water level was then inputted for the extreme event analysis where a simple Gumbel distribution was used to compute flood return periods for the storm surge scenarios modelled (Al-Mashidani et al., 1978).

4.4. Time-lapse Cameras for Storm Surge Analysis

To register the dynamics of a storm surge event, a PENTAX Optio WG-2 GPS camera was installed in the Tuktoyaktuk Community Learning Centre with a time-step of 5 minutes. It operated from 04/08/2019 06:50 to 05/08/2019 22:00 (local time). Pictures taken during a storm surge event on the 5th of August were also

used to visually validate the models' outputs. These locations, represented in Figure 20, were chosen because the monitored areas included distinguishable reference points in the UAV orthophotomap that facilitated the visual validation process and where the water surface was sheltered from strong wave action.

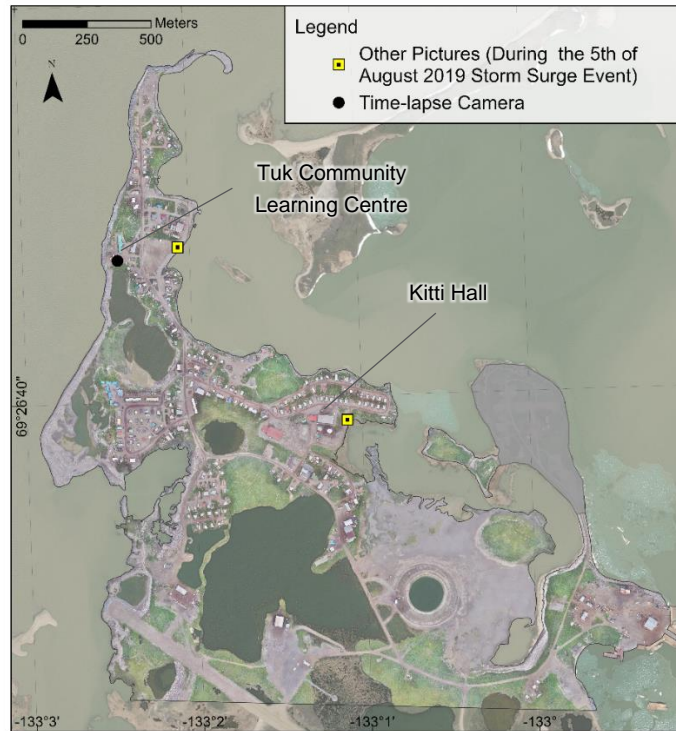


Figure 20 – Location of the time-lapse camera and other pictures taken during the storm event of the 5th of August 2019.

4.5. Driftwood Mapping

Driftwood accumulation caused by strong winds and wave action is very frequent along the shore surrounding the study area. An example of driftwood accumulation in Tuktoyaktuk is illustrated in Figure 21. The driftwood debris can serve as indicators of past flooding events (Harper, 1985; Whalen et al., 2009) and due to the high-resolution of the UAV imagery, as seen in Figure 21 B, it was possible to map these features with precision.

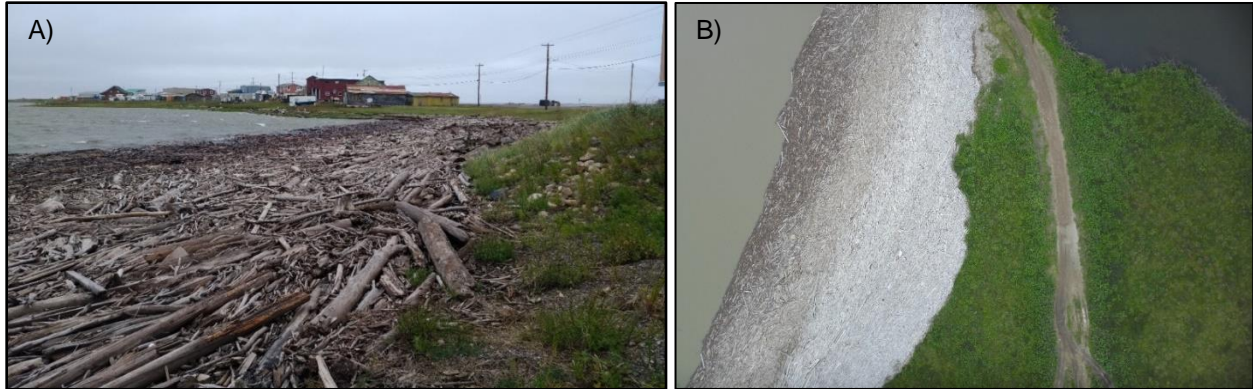


Figure 21 – Driftwood accumulation in Tuktoyaktuk. A) Picture taken during field work. B) Driftwood debris visible from UAV footage

The geographic distribution of the driftwood features, manually digitized in ArcGIS Pro along the uppermost limit of the debris as linear features using the UAV orthophoto map is available in the Appendix (See Figure A 1). Whalen (2005) used the LiDAR DSM along the Mackenzie Delta to extract the Z coordinate of the driftwood features to identify past flooding maximums. In this study the approach was based on the tide gauge data instead of the height of the driftwood features. According to the tide gauge data analyzed, the highest hourly water level registered by the tide gauge was 2.23 m above Chart Datum on the 04/10/1963 at 14:00. This water level was used as input to run simulations on both bathtub and hydrodynamic models and on both elevation datasets to test the hypothesis of the 2.23 m above Chart Datum being the highest water level that occurred in Tuktoyaktuk. To validate the results, the driftwood uppermost limit polylines were converted to points with the Generate Points Along Lines tool in ArcGIS Pro with 1 m distance from each other. The outputs of the models were overlaid by the point features to identify which points were marked as flooded and which hazard class, for the bathtub model, and flooded for the hydrodynamic model. The points that were not contained by the modelled water surface were marked as “Mismatching Points”.

4.6. Bathtub Flood Modelling

4.6.1. Model Description

Using elevation and water level data as core variables is a common practice in flood management. This simplified modelling technique is called bathtub model and there are only two variables in play: the inundation level and elevation. There are, however, several sources of uncertainty affecting the resulting inundation maps, such as the accuracy of the elevation model, the uncertainty related with the sea level rise projections, converting Chart Datum (CD) to the elevation data vertical datum, evenness of the tidal height across the study area and the uncertainty associated with the process of computing storm surge water levels and return periods.

The bathtub inundation model is based on the simplistic premise that an area with an elevation less than the input flood level will be considered as flooded. Hence, the inundated areas are identified by a simple calculation procedure over the raster elevation dataset where all cells with values lower than the input are

marked as flooded. Since only elevation data is needed for its application, estimates regarding hydrological data must be made if this data is absent, which is a common case. There are two fundamental ways to construct the bathtub model: with or without hydrological connectivity (Van de Sante et al., 2012). Models that include hydrological connectivity require that, in addition to being below the flood level, a specific cell or area must be hydrologically connected to the source of flooding, in this case the shoreline, for it to be inundated. Many studies that used bathtub models to map coastal flood inundation worldwide and both hydrologically connected and non-connected variations (Titus and Richman, 2001; Strauss et al., 2012). Van de Sante et al. (2012) suggested that the model that contemplates hydrological connectivity is better suited for coastal flood since it only affects the adjacent land zone.

The bathtub model used was designed to incorporate the measured uncertainties regarding water level and elevation data and represent them in the flood maps by using 4 classes of probability. This brief description is focused on elevation and how its associated errors affect flood maps. The bathtub model uses a single-value water elevation surface, obtained from Tuktoyaktuk's tide gauge, and, in this case, overlaid on two different sets of topography, LiDAR and UAV. Using the local CD allows adjusting elevations to a uniform tidal stage to obtain, for example, the mean highest astronomical tide (MHAT) water level, for the study area. However, converting datums creates uncertainty (Yunus et al., 2016). The tidal surface is not spatially constant. In this case only one tide gauge was used, meaning that no interpolation was made, and the same water height is applied to the study area, but it is necessary to determine the difference between the water level registered by the tide gauge in meters above CD and the vertical datum of the elevation data, CGVD2013. This was achieved by sampling different elevation points across the shore of the study area, represented in Figure 22, using the water uppermost limit, computing the differences between the CGVD2013 value of Z and the tide gauge water level in m above CD registered at the time of the survey and calculating the mean value of the differences that results in a global value of uncertainty expressed by the standard deviation of the samples.

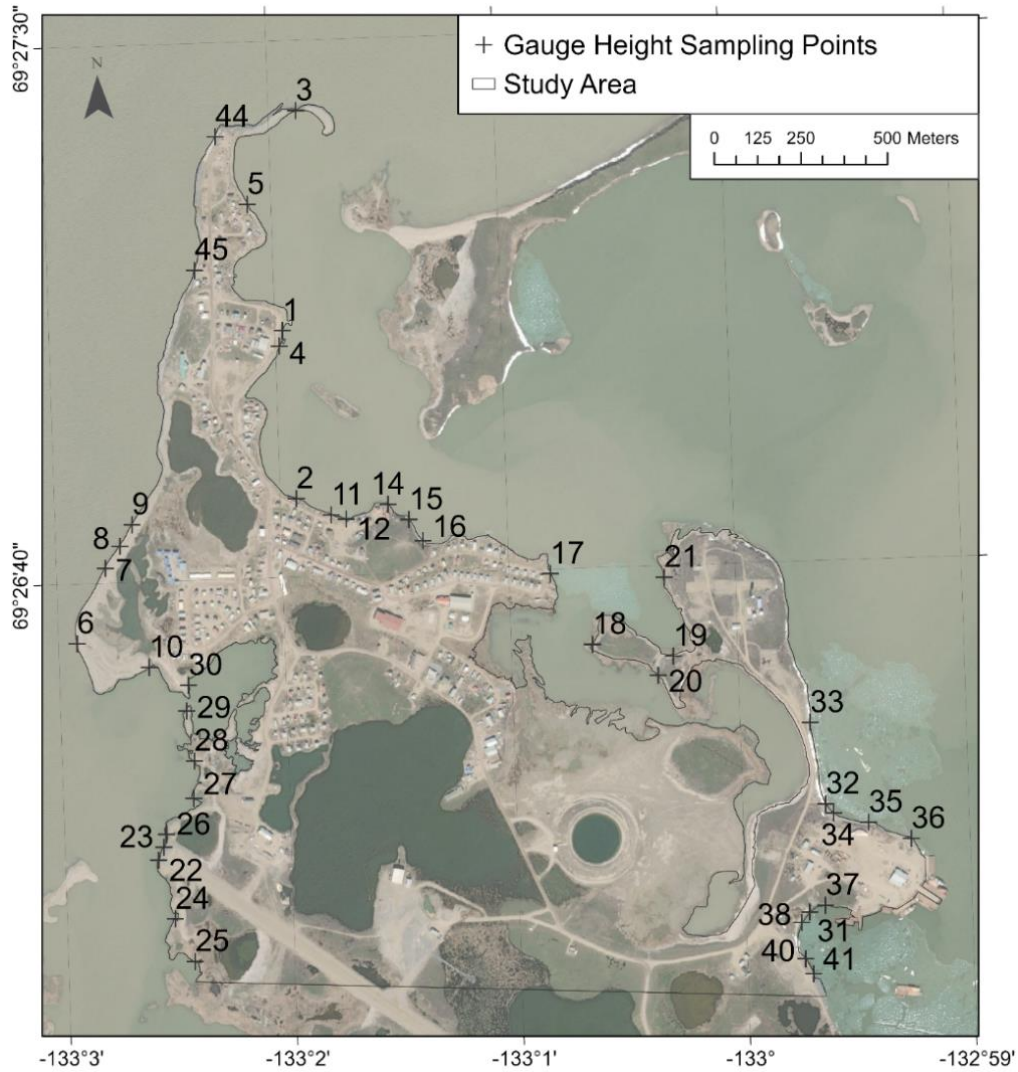


Figure 22 – Spatial distribution and location of the points used to determine the difference between Chart Datum and CGVD2013. Basemap: ESRI.

Another source of uncertainty, potentially higher and with spatial variability is the elevation data itself and its error, expressed as its RMSE. In this model, the technique used to estimate the areas of higher uncertainty is the one described by NOAA (2010). Without water level inaccuracies, the inundation from a single-value water surface is dependent only on the elevation uncertainty. The errors in elevation data are reported as the RMSE and incorporate horizontal errors (FEMA, 2003). RMSE is equivalent to standard deviation (SD) if the data is unbiased (De Smith et al., 2007). In this study it is assumed that RMSE of both elevation datasets is analogous to SD for allowing the computation of a z-score from the data incorporated in the model. The RMSE was computed for each elevation dataset, by applying the general equation:

$$RMSE = \sqrt{\frac{\sum_{i=1}^N \|y(i) - \widehat{y(i)}\|^2}{N}}$$

The locations of the points used to sample the elevation datasets were chosen randomly from a set of points surveyed in 2019 with RTK positioning with a precision of approximately 3 cm in x, y and z are represented in Figure 23.

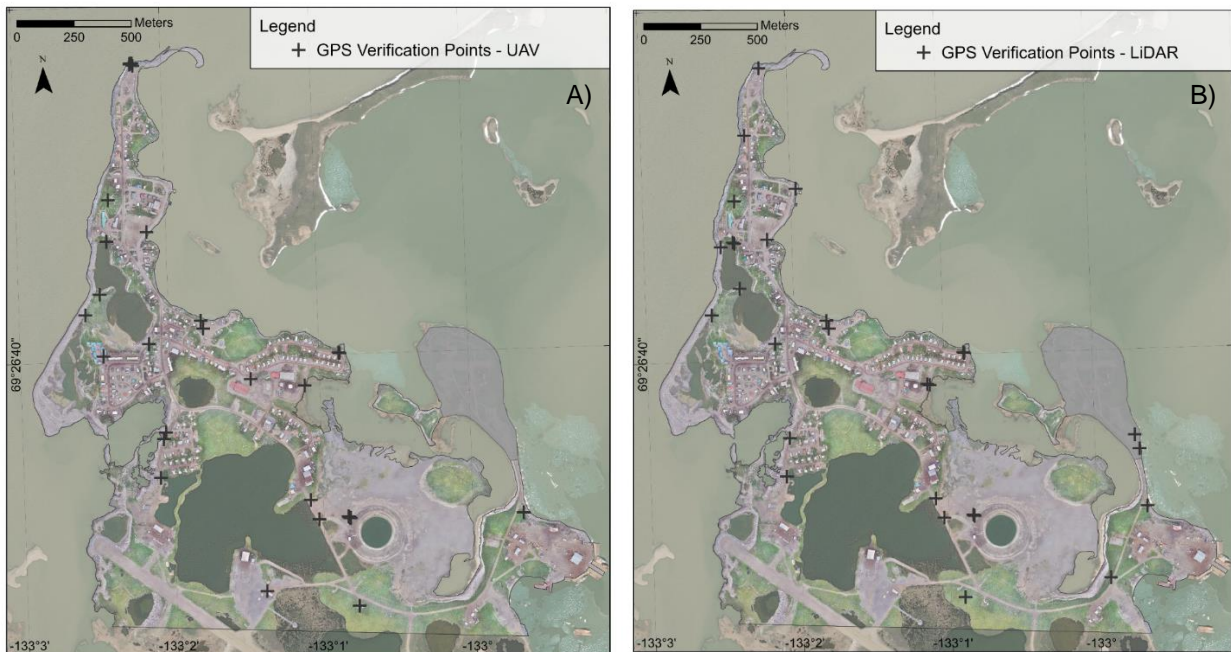


Figure 23 – Spatial distribution of the points used to determine elevation dataset RMSE. A) UAV. B) LiDAR.

To compute a z-score the RMSE must be substituted for SD as seen in Equation (1):

$$Zscore_{(value)} = (Value - Mean_{(population)}) / SD_{(population)} \quad (1)$$

The z-score is the number of standard deviations a specific value deviates from the mean as shown in Figure 24.

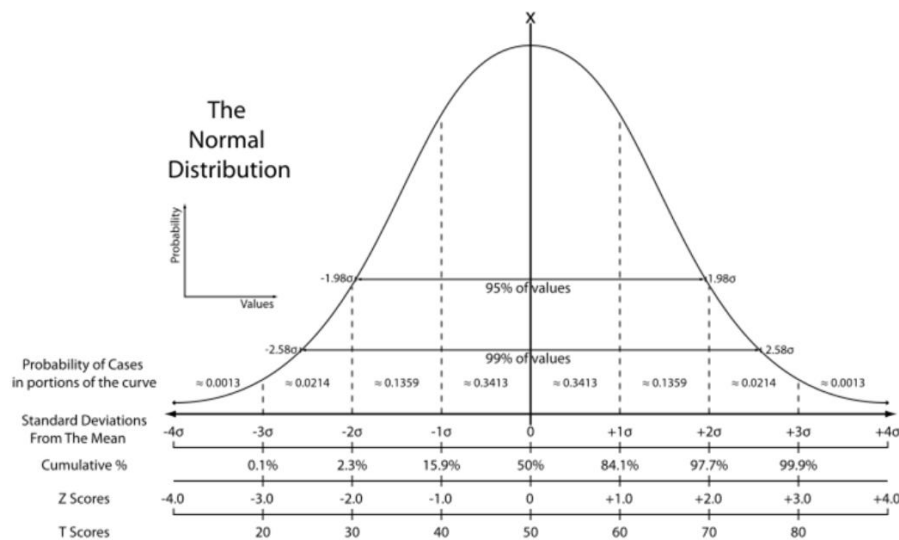


Figure 24 - Z-scores / Standard-Scores and normal distribution.

Equation (1) must be rewritten to incorporate the inundation level and the elevation at a given cell in a specific location X,Y.

$$Zscore_{(X,Y)} = (Water\ Level - Elevation_{(X,Y)})/RMSE_{(Elevation\ data)} \quad (2)$$

Applying Equation (2), the z-score is computed for any elevation data for the given water level and then used to find the percentile rank, represented as Cumulative % in Figure 24. This method uses a cumulative approach, therefore, all the area under the curve, instead of the discrete area between standard deviations and the mean. The probability is determined by centring the respective normal distribution function at the topographic profile to evaluate the input flood water level occurrence probability in a certain elevation at a given location as depicted in Figure 25. A comprehensive example is explained in NOAA (2010).

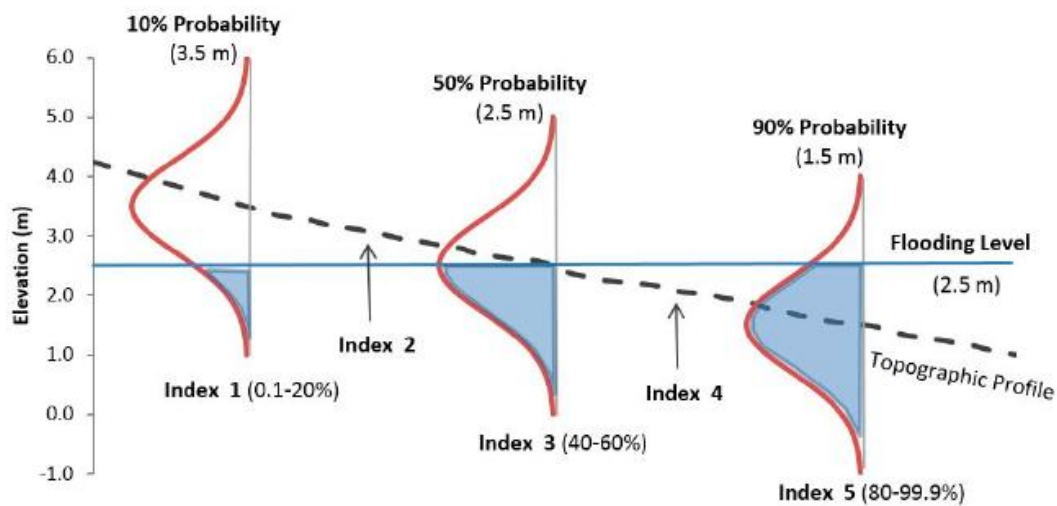


Figure 25 - Estimation of flooding probability for an inundation level of 2.5 m for different terrain elevations accounting for uncertainty by applying NOAA's Coastal Services Center method. Adapted from (Antunes et al., 2019). For the indexes, see Table 2.

The z-score outputs provide a basic understanding of the uncertainty of the flood mapping. They emphasize that uncertainty is not uniform. This plays a big role regarding slope. Areas with low slope angle have higher uncertainty, this meaning that a small vertical error will generate a large horizontal error. In areas with higher slopes, a large vertical error is limited to a certain horizontal expression of that error. In a coastal cliff, for example, large vertical errors translate in small horizontal errors. A particular flood extent can have low uncertainty for a given water level and high uncertainty for another water level. This phenomenon occurs because the second level falls at an elevation extent with lower slopes (NOAA, 2010).

In this model, the error in determining the water surface is also contemplated, with the Chart Datum conversion to CGVD2013. The error that is associated with the water surface is not linked to the elevation error, which allows a sum of squares errors to be performed as stated in Equation (3).

$$Total\ SD = (Error\ (SD)_1^2 + Error\ (SD)_2^2 + \dots + Error\ (SD)_N^2)^{0.5} \quad (3)$$

For a single-value water level model, the total SD error would be summed as seen below in Equation (4) based on the assumption that $RMSE_{(elevation)}$ is equal to $SD_{Elevation}$:

$$SD_{Inundation} = (SD_{elevation}^2 + SD_{water\ level}^2)^{0.5} \quad (4)$$

Substituting $SD_{Inundation}$ for $RMSE_{(Elevation\ Data)}$ in Equation (4) yields:

$$Zscore_{(X,Y)} = (Inundation_{(water\ surface)} - Elevation_{(X,Y)})/SD_{(Inundation)} \quad (5)$$

The errors and uncertainties associated with the sea level rise scenarios, the results from the harmonic and storm surge analyses were also incorporated by the same approach, where SD_{total} is defined as:

$$SD_{total} = (SD_{elevation}^2 + SD_{Chart\ Datum\ to\ CGVD2013}^2 + SD_{tide}^2 + SD_{sea\ level\ rise}^2 + SD_{storm\ surge}) \quad (6)$$

Substituting $SD_{(Inundation)}$ in Equation (5) for SD_{total} from Equation (6):

$$Zscore_{(X,Y)} = (Inundation_{(water\ surface)} - Elevation_{(X,Y)})/SD_{total} \quad (7)$$

Based in Marcy et al (2011), after creating the computed raster dataset with the z-scores, a first Reclassify tool converts the z-score of each cell to its respective Cumulative % with the normal distribution. A second use of the Reclassify tool changes the Cumulative % values to 4 classes of probability that depict the mapping confidence as seen in Table 2.

Table 2 – Probability range and hazard classes used for mapping. Adapted from Antunes et al. (2019).

	Low	Moderate	High	Extreme
Hazard Class Level	2	3	4	5
Flood Probability	20–40 %	40 – 60 %	60–80 %	>80 %

4.6.2. Model Setup

The bathtub model offers a simplistic approach compared to hydrodynamic modelling, which translates in a faster design and implementation. The model ran on LiDAR and UAV elevation data, based on the approach described in the previous chapter. RCP 4.5 and RCP 8.5 SLR scenarios were added on top of the derived mean highest astronomical tide and for both storm surge return periods (50-year and 100-year). The hydrological connectivity of cells was set by the Region Group tool in ArcGIS Pro with eight neighbours, meaning that the connectivity is evaluated in both orthogonal and diagonal of each input. Culverts that allow the flow of water from and to areas that would be unconnected by analysing solely the elevation data, were incorporated in both elevation datasets. A third level of hydrological connectivity is related with the shoreline. Since the focus in a bathtub approach is sea level rise (SLR), flooding will only occur if there is

connectivity to the sea. To model this phenomenon, the Buffer tool was used to the digitized shoreline of 0.5 m radius to create a polygon that is used to select polygons by location that are connected to the shoreline and remove the unconnected ones. The hydrological connectivity approach is represented in Figure 26 c).

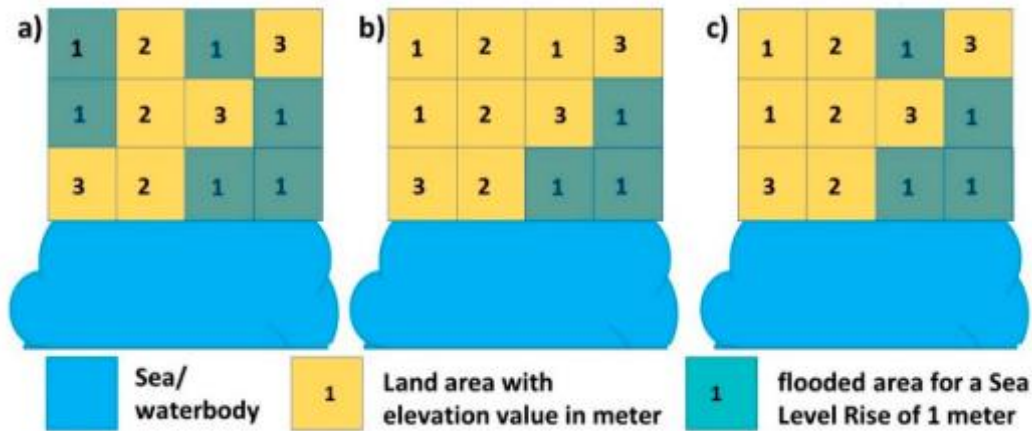


Figure 26 – Different bathtub approaches. (a) zero connectivity rule; (b) four-way connectivity in orthogonal directions, excluding cells not connected to the sea and (c) eight-way hydrological connectivity rule for 1 m SLR where a cell is flooded only if it is connected to a water body directly or via adjacent cells in either orthogonal or diagonal directions (Yunus et al., 2016).

The ArcGIS Pro Model Builder layout designed specifically for this study to automate the modelling process of the bathtub approach is represented in Figure 27. After obtaining the layer with the flooded areas by hazard class, the layers Building Footprints, Roads and Parcels were overlaid to generate maps of the affected infrastructures by hazard class.

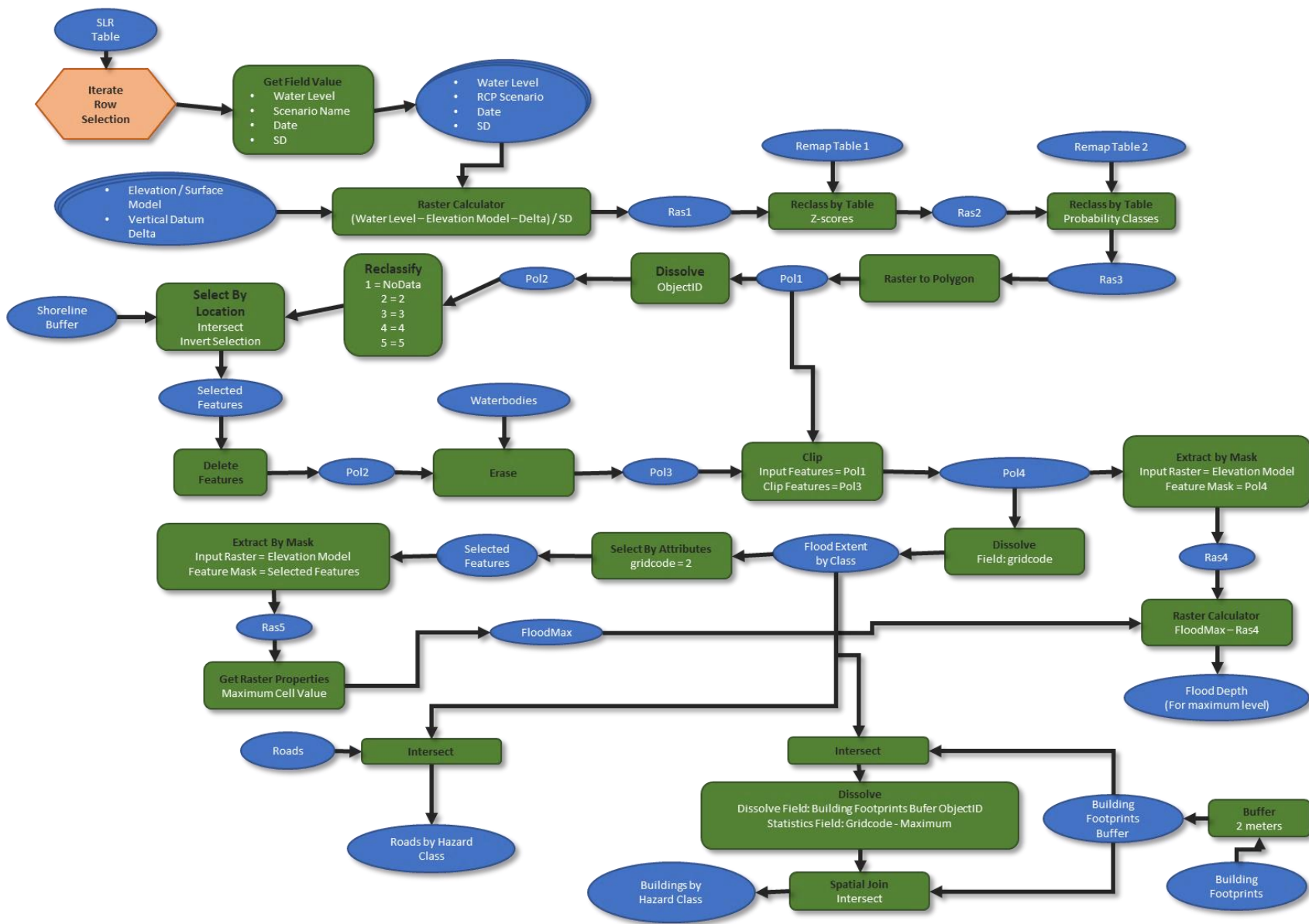


Figure 27 – ArcGIS Pro Model Builder process used for bathtub modelling.

4.7. Hydrodynamic Flood Modelling (MOHID)

4.7.1. Model description

MOHID Water is a 3D numerical model that simulates free surface water bodies developed by MARETEC (Marine and Environmental Technology Research Centre) at Instituto Superior Técnico, University of Lisbon. MOHID Studio was developed to aid the implementation of the model with a complete GUI, GIS data processing, simulation editing, visual representation of results, plotting time series and exporting tools.

The model has been used in several coastal and estuarine locations and it can simulate complex features of flows (Mateus & Neves, 2013). It started with a finite-differences approach and later incorporated baroclinic mode (Santos, 1995) and finite volumes for generic vertical coordinates (Martins, 2001).

The computation of horizontal velocities the module Hydrodynamic solves Navier-Stokes's equations using the hydrostatic approach and Boussinesq and Reynolds approximations (Franz et al. 2017):

$$\frac{\partial}{\partial t} \int_V \vec{v}_H dV = - \oint_A \vec{v}_H (\vec{v} \cdot \vec{n}) dA + \oint_A v_T (\nabla(\vec{v}_H) \cdot \vec{n}) dA - \frac{1}{\rho} \oint_A p \cdot \vec{n}_H dA + \int_V 2\vec{\Omega} \times \vec{v}_H dV + \vec{F} \quad (8)$$

Where V represents the control volume, A the surface of the control volume, $\vec{v}_H = (u, v)$ the horizontal velocity vector, $\vec{v} = (u, v, w)$ the velocity vector, \vec{n} the surface normal, \vec{n}_H the normal of the horizontal plane, v_T the turbulent viscosity, ρ the water density, p the water pressure, g the acceleration of gravity, η the water level, $\vec{\Omega}$ the earth rotation vector and \vec{F} the external forces. In Equation (8) the first component represents advection, the second diffusion, the third pressure gradient forces, the fourth Coriolis and the fifth external forces.

Water pressure is calculated by:

$$p = g \int_z^\eta \rho dz + p_{atm} \quad (9)$$

In Equation (9) z is the vertical coordinate and p_{atm} the atmospheric pressure.

To compute the density, MOHID utilizes the state equation from UNESCO (Fofonoff and Millard, 1983). The density is computed as a function of temperature salinity and pressure. The computed values are then used in the water velocity calculation, depicted in Equation (8). The hydrostatic equilibrium approximation states that the pressure in one point only depends on the weight caused by the water column in this point. This is valid when the vertical forces, excluding the gravity force, are negligible compared to the force of gravity. The Boussinesq approximation states that the differences in densities are ignored except when multiplied by the acceleration of gravity. Figure 28 represents the communication between the different modules and how they relate with the module Hydrodynamic (MARETEC, 2012).

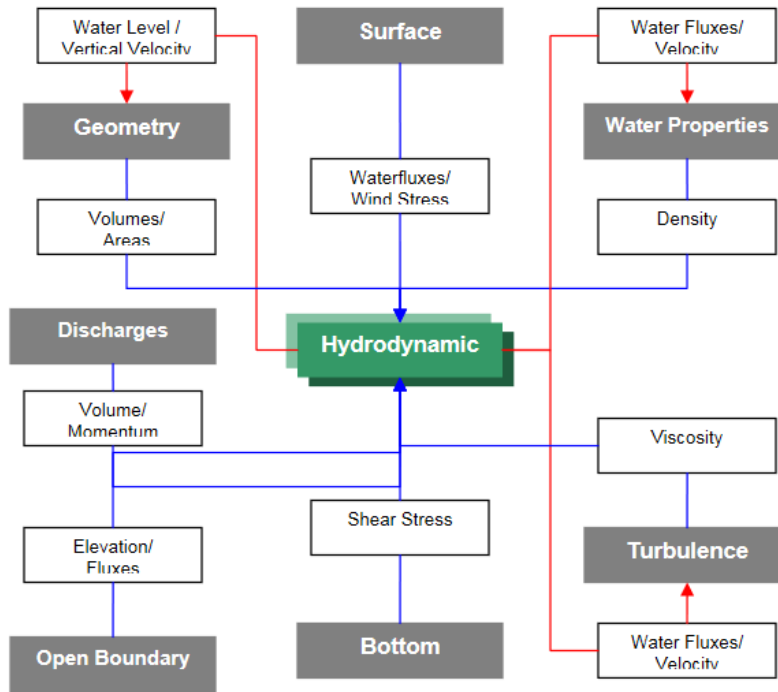


Figure 28 - Hydrodynamic Module flux of information with other modules. Adapted from MARETEC (2012).

The computation of the free surface is assured by solving the continuity equation for an incompressible fluid in 2D. The height of the free surface is determined only by the horizontal fluxes of flow and any other sources or sinks of water resulting in (Leitão 2002):

$$\frac{\partial}{\partial t} \int_V \rho dV = \oint_A \rho (\vec{v}_H \cdot \vec{n}) dA + Sources - Sinks \quad (10)$$

In Equation (10) the control volume is unknown, ρ is known and the horizontal velocities were computed, but since the horizontal grid is well defined, the equation is solvable with only one unknown left which is the free surface height. To compute the vertical velocity, it is necessary to apply the divergence theorem and Leibniz integral rule to the continuity equation for an incompressible fluid resulting in Equation (11) (Leitão 2002), where h is the depth.

$$w(z) = \int_{-h}^{\eta} \left(\frac{\partial u(z)}{\partial x} + \frac{\partial v(z)}{\partial y} \right) dz \quad (11)$$

The equations' spatial discretization achieved by the finite volumes' method. The discretized equations are applied to a control volume where the solution is independent of cells' geometry. For the horizontal spatial discretization, an Arakawa-C (Arakawa, 1966) is used. Water properties are computed at the cells' centre while velocities are computed at the surfaces. Since the solution of the equations is independent of the

geometry of the cells, it is possible to use a generic vertical discretization (Martins et al. 1998), allowing different types of layers in the same model's domain. Sigma layers (Figure 29) adapt to bathymetry and to the water height. Utilizing sigma layers for the water surface is useful given its advantage in adapting to the change of the water level.

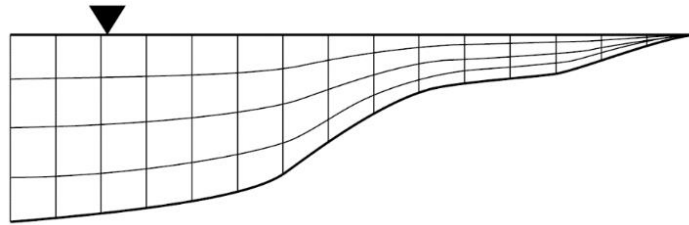


Figure 29 – Sigma layers with 4 layers. Adapted from MARETEC (2012)

The temporal discretization of equations is made possible by an ADI (Alternating Direction Implicit) algorithm proposed by Leendertse (1967).

4.7.2. Model Setup

MOHID modules are selected and combined according to the geometrical requirements and state variables. The modules used were, Atmosphere, Geometry, Hydrodynamic, InterfaceWaterAir, Model (core module), Tide, Turbulence and WaterProperties. For this study, the adopted geometry was composed by 3 sigma-type layers with 0.4, 0.3 and 0.3 relative thickness, from bottom to top. Since the main interest was the behaviour of the water surface, the layer geometry was kept at 2D. All other water properties were set as default. To maintain model stability, the horizontal viscosity (VISCOSITY_H) was set at 0.001 m²/s. A simplified workflow for the hydrodynamic modelling process is represented in Figure 30.

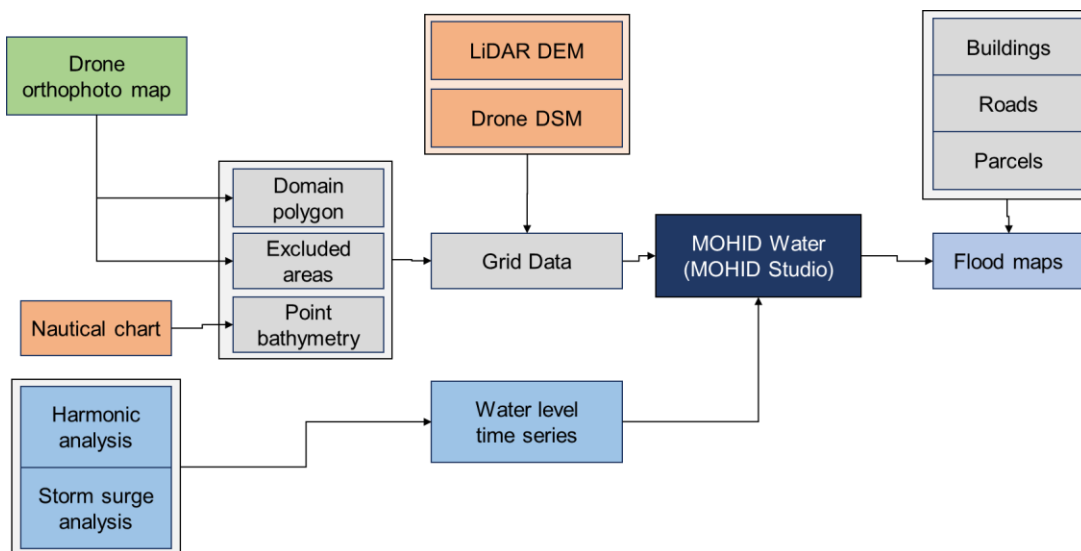


Figure 30 –Hydrodynamic modelling workflow diagram.

The hydrodynamic model grid was set with a regular cell size of 5 x 5 m and an extent as seen in Figure 31. Since the study area is surrounded by shallow waters and the hydrodynamics of the model are based in tidal forcing, designing a smaller model extent has the advantage of using a smaller grid cell size and, therefore, decreasing elevation data loss to resampling algorithms.

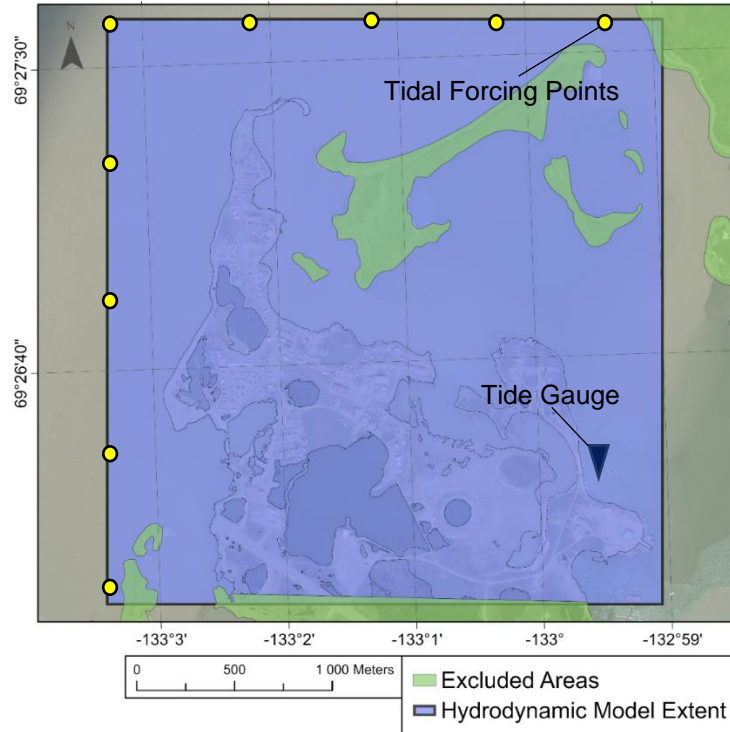


Figure 31 – Hydrodynamic model extent and excluded areas.

The Tidal Forcing Points shown in Figure 31, represent the locations where MOHID Studio’s Tidal Tool was used. The water level used for each simulation was forced in these points to generate the tide and then validated at the Tide Gauge point. The location of Tidal Forcing Points on the western and northern limits of the hydrodynamic grid is justified by the fact that these are considered the open boundaries of the system, so the model accurately represents flow direction as tide changes. The water level was read at 69°26’19.18”N, 132°59’36.51”W. Bathymetry data was derived from the nautical chart “Chart 7685 – Tuktoyaktuk Harbour and Approaches” obtained from the Canadian Hydrographic Service website. The points given in height above Chart Datum with known depth were digitized manually and interpolated using the inverse distance weighted (IDW) method. The output is represented in Figure 32.

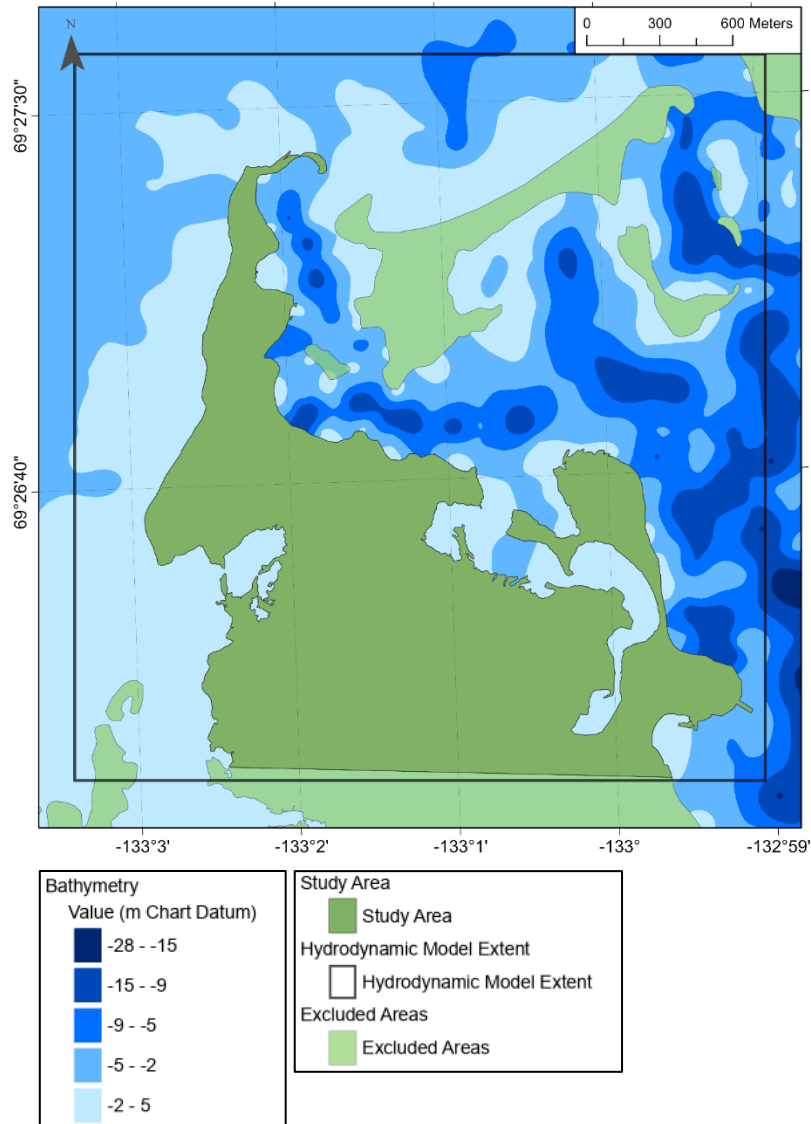


Figure 32 – Interpolated bathymetry surface used in the hydrodynamic modelling.

MOHID reads elevation data as DAT format (.dat). Two combined raster datasets of bathymetry and elevation models were created. One composed by the LiDAR elevation model and bathymetry and the other by the UAV surface model and bathymetry. This data transformation was done on ArcGIS Pro by replacing the values of the elevation on the bathymetry raster, creating a continuous and gapless dataset that was exported to MOHID Studio as XYZ files (.xyz). To this point, the LiDAR dataset kept the original 1 x 1 m cell size and the UAV dataset 0.1 x 0.1 m. After importing the XYZ files, a grid with a cell size of 5 m by 5 m was created (Figure 32) in MOHID Studio and the XYZ data converted to DAT by the built-in tool “xyz to grid data”. Both elevation datasets were resampled to 5 x 5 m cells using the IDW interpolation option after applying the Construct Grid Data tool, resulting in the following general parameters:

```

COORD_TIP           : 5
ILB_IUB             : 1 600
JLB_JUB             : 1 570
ORIGIN              : 576161.36 7703933.37
GRID_ANGLE          : 0
CONSTANT_SPACING_X  : 1
CONSTANT_SPACING_Y  : 1
DX                  : 5
DY                  : 5
FILL_VALUE          : -99

```

The grid data datasets are represented in the Appendix for UAV (see Figure A 3) and for LiDAR (see Figure A 4).

4.8. Validation of the Model Results

4.8.1. Local Knowledge and Field Observations

Knowledge shared by the local community allowed the validation process of the inundation models. The information was provided in form of geodata provided by the staff of the Hamlet of Tuktoyaktuk (see Figure A 2), informal interviews and testimonials by locals. Several visits to the most affected areas were arranged by the Hamlet where detailed information regarding reference points from previous flood events were recorded. The contribution of Calvin Pokiak (Hamlet of Tuktoyaktuk) was essential for this study, his enthusiasm, interest, and knowledge were vital to better understand the dynamics and the impacts of past flooding events in Tuk.

4.8.2. UAV Imagery Analysis and Chart Datum Conversion

The use of the georeferenced aerial footage facilitates the process of validation due to the high number of pictures taken along the shoreline. The timestamp of each picture was used to relate the shoreline water height with the water level given by the tide gauge at the locations represented in Figure 33. These points were used to establish the correspondence between Chart Datum and the vertical datum of both DSM and DEM, CGVD2013, by extracting the value of Z from the UAV DSM at the uppermost limit of the water surface to compute the difference between the water level recorded at the tide gauge at the time of the picture taken by the UAV.

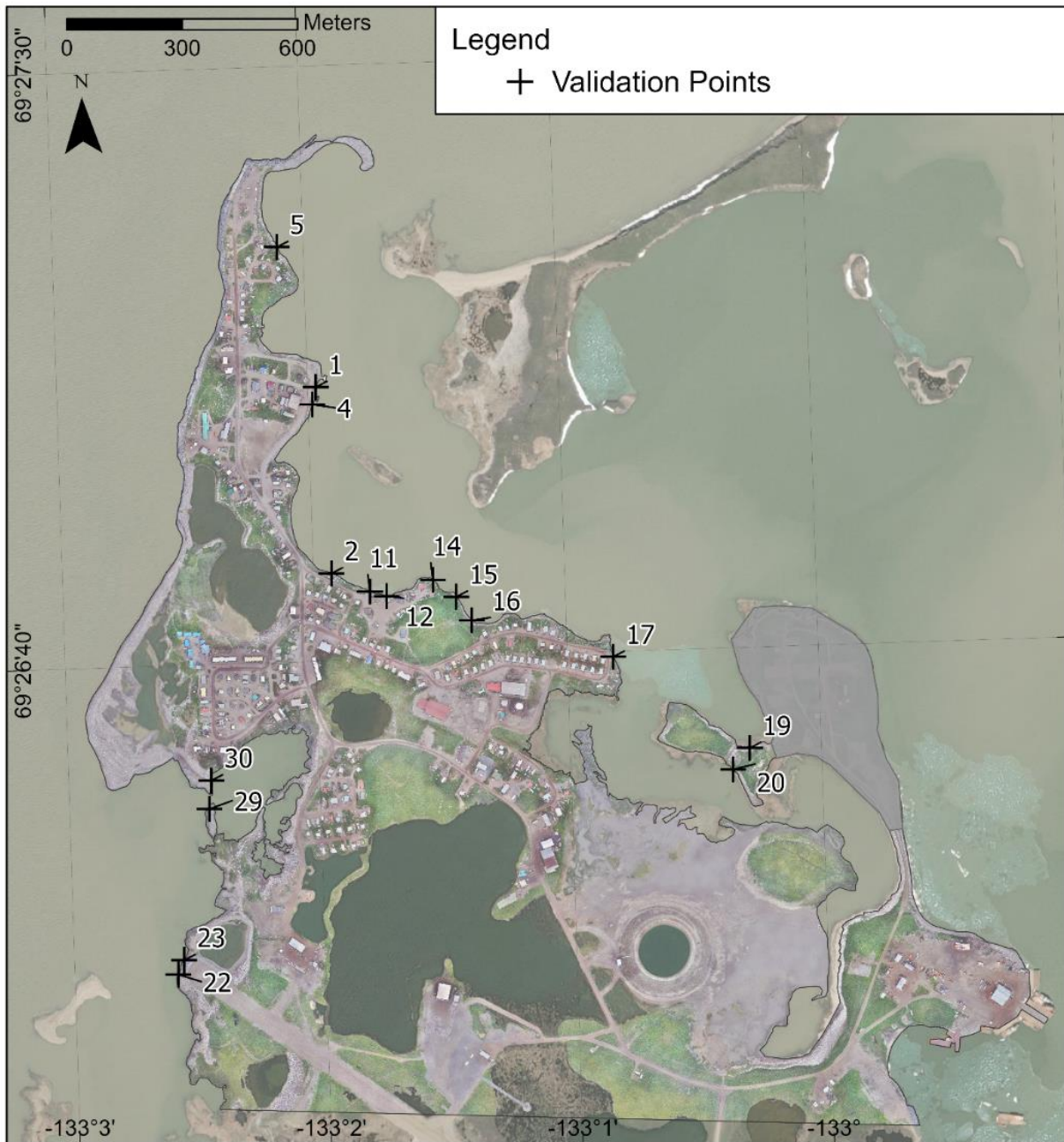


Figure 33 – Location of the points used to validate the inundation models.

To effectively compare the models, the points are located along shore segments that did not change significantly from the LiDAR DEM to the UAV DSM, thus the reduction in sample size compared to the points used to convert the Chart Datum to CGVD2013.

5. Analysis and Discussion of the Results

5.1. Data Uncertainty Assessment

5.1.1. Chart Datum Conversion to CGVD2013

Figure 34 shows the location of the points where the tool Sample was used to determine the difference between Chart Datum and CGVD2013 and the spatial variability of the absolute error computed for each sampling point in relation to the average value of 0.61 m. The smaller numbers represent the point identifier while the numbers with the white halo are the values of the absolute error for a given point. The results show a high spatial and numerical variability in the computed differences. These differences can be explained by the weather conditions that disrupt the water surface and cause waves, the difficulty in identifying the exact location of the uppermost limit of the water surface in the images, the inherent vertical and horizontal errors of the surface model and the travel time of the tidal wave to the tide gauge.

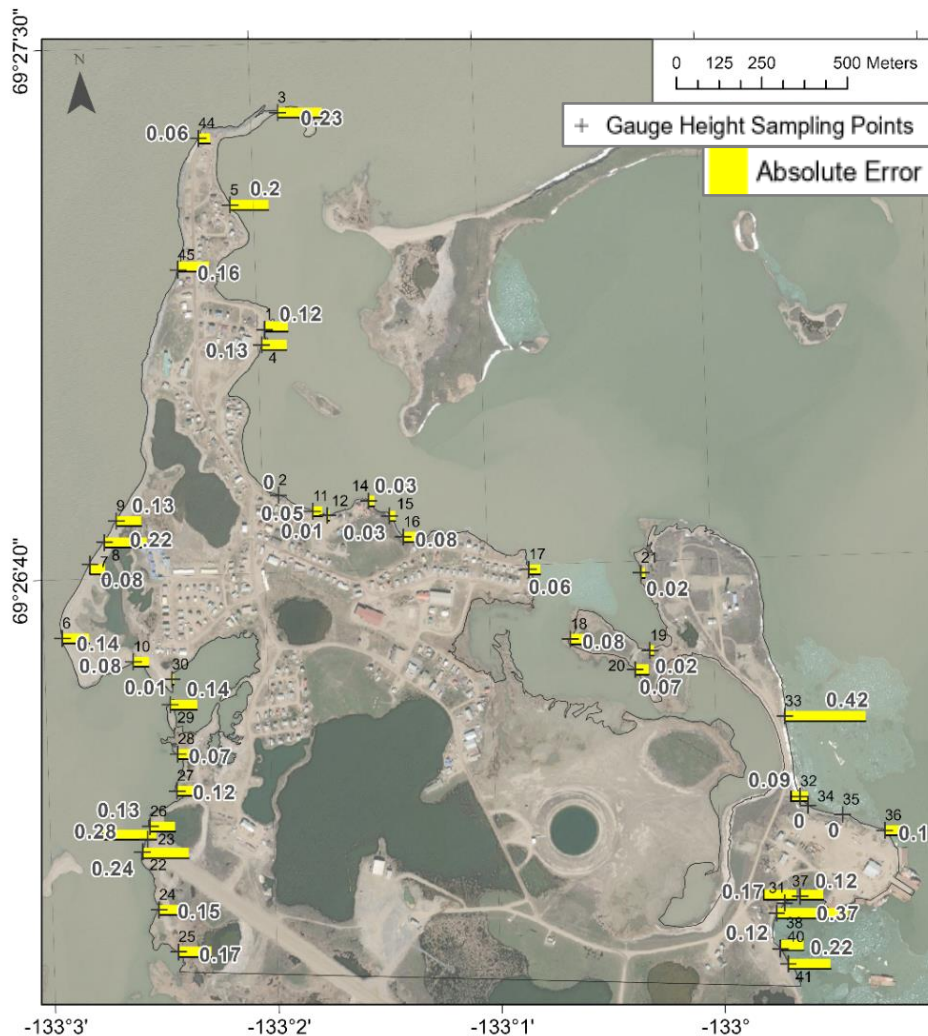


Figure 34 - Absolute error in meters by gauge height sampling point.

OBJECTID	Img	Date (UTC)	Hour (UTC)	Hour (UTC-6)	Flight Number	Z Drone (m)	Tide Gauge Water Level (m above Chart Datum)	Difference (m)	Absolute Error (m)	Relative Error (m)	Squared Error	WindSpeed (km/h)	Wind Direction (10s Deg)
1	EP-11-32389_0032_0162	01/08/2018	18:49:00	12:49:00	1	-0.217	0.51	0.73	0.12	0.20	0.01	8	11
2	EP-11-32389_0032_0110	01/08/2018	18:46:00	12:46:00	1	-0.100	0.51	0.61	0.00	0.00	0.00	8	11
3	EP-11-32389_0032_0145	01/08/2018	18:48:00	12:48:00	1	-0.327	0.51	0.84	0.23	0.38	0.05	8	11
4	EP-11-32389_0032_0228	01/08/2018	18:56:00	12:56:00	1	-0.229	0.51	0.74	0.13	0.22	0.02	7	11
5	EP-11-32389_0032_0345	01/08/2018	19:00:00	13:00:00	1	-0.294	0.51	0.80	0.20	0.32	0.04	7	11
6	EP-11-32389_0033_0017	01/08/2018	19:50:00	13:50:00	2	0.057	0.52	0.46	0.14	0.36	0.02	7	10
7	EP-11-32389_0033_0058	01/08/2018	19:53:00	13:53:00	2	-0.005	0.52	0.53	0.08	0.21	0.01	7	10
8	EP-11-32389_0033_0093	01/08/2018	19:55:00	13:55:00	2	0.134	0.52	0.39	0.22	0.14	0.05	7	10
9	EP-11-32389_0033_0119	01/08/2018	19:56:00	13:56:00	2	-0.217	0.52	0.74	0.13	0.08	0.02	7	10
10	EP-11-32389_0033_0148	01/08/2018	19:58:00	13:58:00	2	-0.004	0.52	0.52	0.08	0.01	0.01	7	10
11	EP-11-32389_0034_0086	01/08/2018	23:18:00	17:18:00	3	0.248	0.81	0.56	0.05	0.05	0.00	10	9
12	EP-11-32389_0034_0167	01/08/2018	23:23:00	17:23:00	3	0.195	0.81	0.62	0.01	0.04	0.00	10	9
14	EP-11-32389_0034_0254	01/08/2018	23:28:00	17:28:00	3	0.243	0.82	0.58	0.03	0.13	0.00	10	9
15	EP-11-32389_0034_0261	01/08/2018	23:29:00	17:29:00	3	0.239	0.82	0.58	0.03	0.09	0.00	10	9
16	EP-11-32389_0034_0338	01/08/2018	23:33:00	17:33:00	3	0.289	0.82	0.53	0.08	0.13	0.01	10	9
17	EP-11-32389_0035_0036	02/08/2018	00:18:00	18:18:00	4	0.319	0.87	0.55	0.06	0.04	0.00	15	8
18	EP-11-32389_0035_0122	02/08/2018	00:16:00	18:16:00	4	0.343	0.87	0.53	0.08	0.12	0.01	15	8
19	EP-11-32389_0035_0214	02/08/2018	00:25:00	18:25:00	4	0.297	0.88	0.58	0.02	0.04	0.00	15	8
20	EP-11-32389_0035_0249	02/08/2018	00:27:00	18:27:00	4	0.347	0.88	0.53	0.07	0.40	0.01	15	8
21	EP-11-32389_0035_0268	02/08/2018	00:28:00	18:28:00	4	0.248	0.88	0.63	0.02	0.46	0.00	15	8
22	EP-11-32389_0037_0367	02/08/2018	17:15:00	11:15:00	5	-0.192	0.66	0.85	0.24	0.25	0.06	15	5
23	EP-11-32389_0037_0463	02/08/2018	17:21:00	11:21:00	5	-0.235	0.65	0.88	0.28	0.28	0.08	15	5
24	EP-11-32389_0037_0178	02/08/2018	17:05:00	11:21:00	5	-0.089	0.67	0.76	0.15	0.22	0.02	15	5
25	EP-11-32389_0037_0175	02/08/2018	17:05:00	11:05:00	5	-0.095	0.68	0.78	0.17	0.20	0.03	15	5
26	EP-11-32389_0039_0081	02/08/2018	17:56:00	11:56:00	7	-0.162	0.58	0.74	0.13	0.12	0.02	10	1
27	EP-11-32389_0039_0243	02/08/2018	18:05:00	12:05:00	7	-0.160	0.57	0.73	0.12	0.22	0.02	10	1
28	EP-11-32389_0039_0308	02/08/2018	18:09:00	12:09:00	7	-0.120	0.56	0.68	0.07	0.02	0.01	10	1
29	EP-11-32389_0039_0418	02/08/2018	18:16:00	12:16:00	7	-0.194	0.55	0.74	0.14	0.28	0.02	10	1
30	EP-11-32389_0039_0470	02/08/2018	18:19:00	12:19:00	7	-0.043	0.55	0.59	0.01	0.14	0.00	10	1
31	EP-11-32389_0041_0022	02/08/2018	19:35:00	13:35:00	9	0.040	0.48	0.44	0.17	0.69	0.03	12	4
32	EP-11-32389_0042_0358	02/08/2018	20:12:00	14:12:00	10	-0.041	0.48	0.52	0.09	0.00	0.01	13	3
33	EP-11-32389_0042_0097	02/08/2018	19:57:00	13:57:00	10	0.293	0.48	0.19	0.42	0.00	0.18	13	3
34	EP-11-32389_0042_0434	02/08/2018	20:17:00	14:12:00	10	-0.126	0.48	0.61	0.00	0.17	0.00	13	3
35	EP-11-32389_0042_0500	02/08/2018	20:20:00	14:20:00	10	-0.128	0.48	0.61	0.00	0.20	0.00	13	3
36	EP-11-32389_0042_0577	02/08/2018	20:25:00	14:25:00	10	-0.221	0.49	0.71	0.10	0.60	0.01	13	3
37	EP-11-32389_0043_0154	02/08/2018	20:54:00	14:54:00	11	0.022	0.51	0.49	0.12	0.20	0.01	10	5
38	EP-11-32389_0043_0179	02/08/2018	20:56:00	14:56:00	11	0.269	0.51	0.24	0.37	0.37	0.13	10	5
40	EP-11-32389_0043_0203	02/08/2018	20:57:00	14:57:00	11	0.024	0.51	0.49	0.12	0.09	0.01	10	5
41	EP-11-32389_0043_0233	02/08/2018	20:59:00	14:59:00	11	0.126	0.51	0.38	0.22	0.27	0.05	10	5
44	EP-11-32389_0032_0463	01/08/2018	19:07:00	13:07:00	1	-0.153	0.51	0.66	0.06	0.24	0.00	7	11
45	EP-11-32389_0032_0510	01/08/2018	19:09:00	13:09:00	1	-0.259	0.51	0.77	0.16	0.14	0.03	7	11

Table 3 – Gauge height sampling point data summary used for Chart Datum conversion.

Table 3 summarizes all the timestamps of the UAV footage, coordinates and heights for each point utilized in the process. The box plot in Figure 35 shows the statistics obtained for the difference between the value measured at the tide gauge in Chart Datum the sampling from the UAV DSM in CGVD2013. The boxplot reflects the variability of the data with a standard deviation equal to 15 cm ($SD_{CD\ to\ CGVD2013}$), but during the validation process, the value adopted of 0.61 m (mean) for the conversion of the tide gauge data in Chart Datum to CGVD2013 resulted in high precision in the modelled water-surfaces.

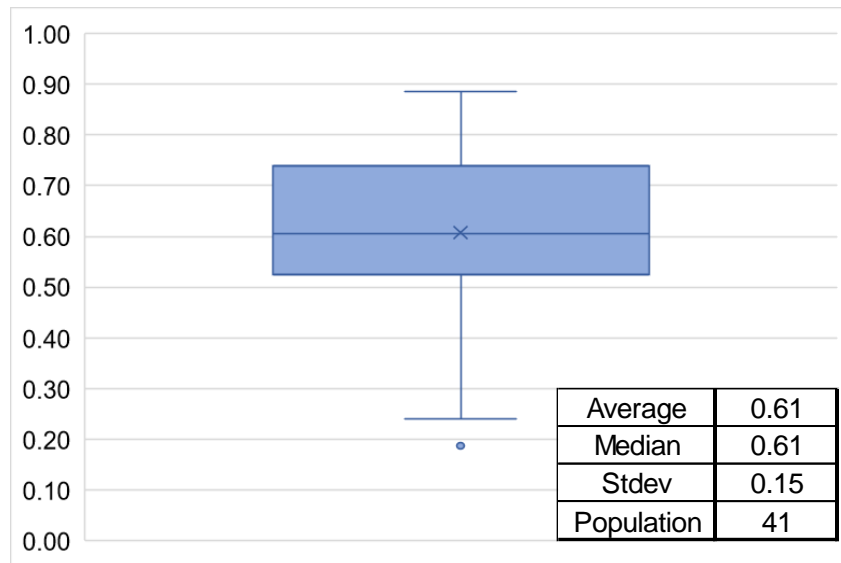


Figure 35 – Boxplot of Gauge Height Sampling Points difference between CGVD2013 and Chart Datum.

Elevation Data

For the bathtub model, as explained in Chapter 3, the RMSE was calculated for both UAV and LiDAR elevation datasets. The computed RMSE and spatial distribution obtained by the IDW tool of the squared differences is expressed in Figure 36.

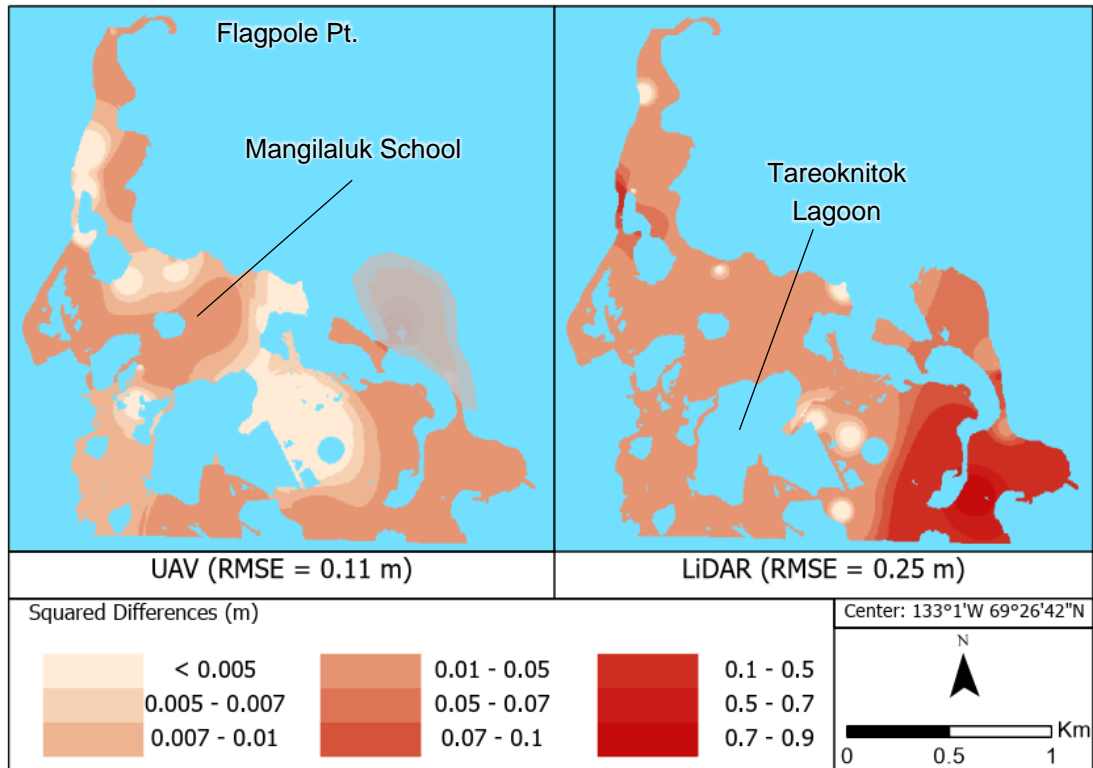


Figure 36 – Spatial distribution of the squared differences of Z-GPS and Z-DSM and Z-DEM in CGVD2013.

The RMSE in meters of the LiDAR dataset is higher, resulting in a higher overall uncertainty and, therefore, an increase in area of flood hazard classes of lower probabilities. Figure 36 shows that the interpolated surfaces of the squared differences of the different elevation models is very distinct and that varies significantly from location to location. A notorious deviation can be observed in the LiDAR DEM, especially in southeast region of the study area where the values ranging from 0.1 to 0.9, translating in larger flood extents associated with lower probability hazard classes. There are, however, areas where the UAV DSM has the same magnitude of deviation as the LiDAR DEM, indicating where the model could use more GCPs to improve its vertical accuracy, such as Flagpole Point, the area surrounding Mangilaluk School and the south shore of Tareoknitok Lagoon.

The output of subtracting the two elevation datasets is shown in Figure 37. As expected, the higher differences represent the shrub-vegetated areas and features such as cars, boats, and buildings, that are eliminated in the generalization process of creating a DEM, as opposed to a DSM. Although, it is possible to identify an overall agreement of the LiDAR elevation by Flagpole Point (areas in light blue) with differences ranging from -50 to -10 cm. In areas without vegetation or buildings, both datasets show the lowest differences in absolute value, as it represents the areas where both models are expected to represent the same surface. The uncertainty regarding the conversion from CGVD28 to CGVD2013 of the LiDAR dataset could explain some of the deviations, but since the phenomenon is not uniform across the study area, it can be a consequence of localized poorer vertical accuracy. Another possible cause is related with soil subsidence and, since there is no vegetation contributing to higher elevations for the UAV DSM in the sectors with negative values. The dark red areas highlight not just the buildings that are included in the UAV DSM, but also indicate deposition of new sediments along the western shoreline, while the dark blue shows where coastal erosion processes had been the most effective. It is worth mentioning the positive effects of the concrete slabs installed in Flagpole point on protecting the shore from shoreline retreat caused by erosion.

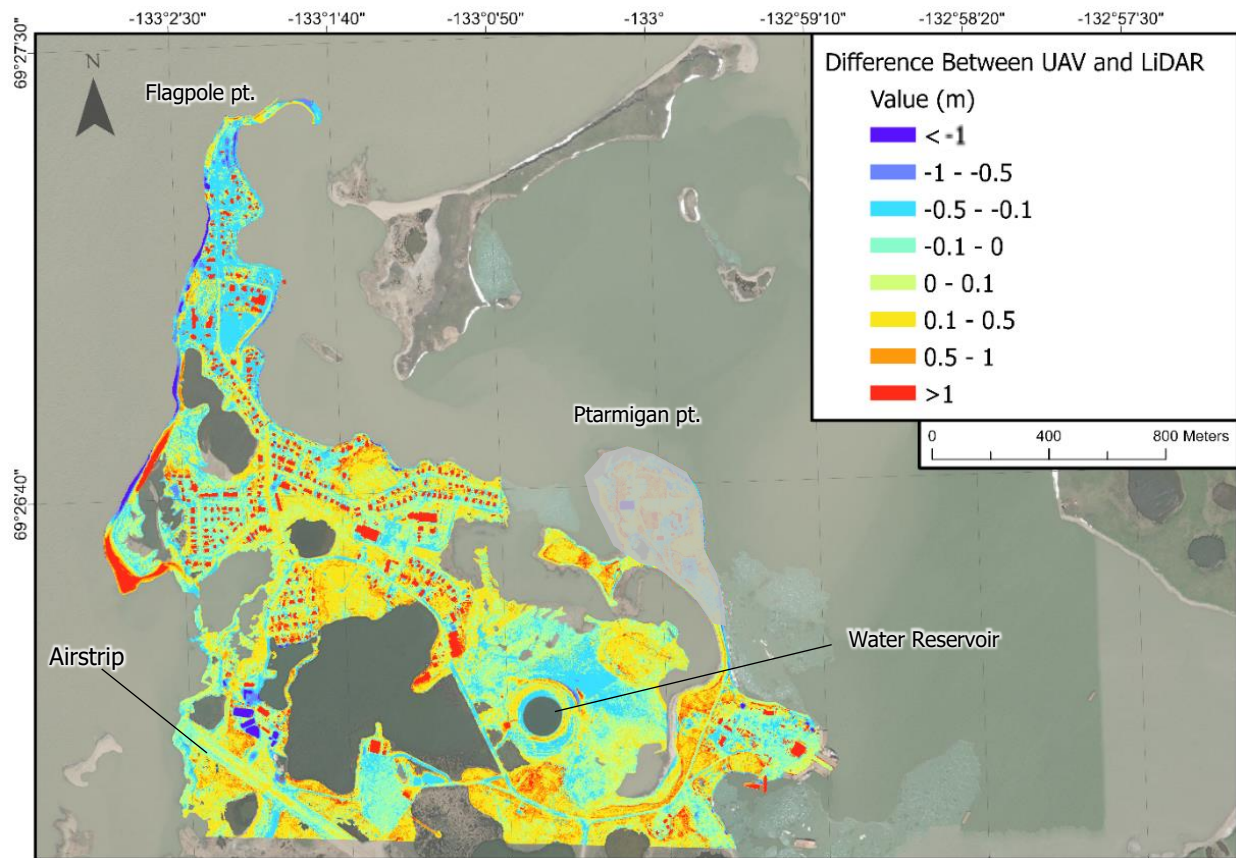


Figure 37 – Difference between UAV DSM and LiDAR DEM in CGVD2013.

5.2. Harmonic Analysis of the Tides

Figure 38 shows the hourly harmonized time series data and tidal range for the open water season obtained with UTide. It reflects the rise of mean sea level and applying a linear trend fit to the data resulted in a value of approximately 2.2 mm/year of mean sea level rise with a $R^2 = 0.938$, as shown in Figure 39. This value is lower than the most recent data published by NOAA that sets the value for mean sea level rise in Tuktoyaktuk as 2.75 ± 1.07 mm/year from 1961 to 2018 and 3.5 ± 1.1 mm/year from 1961 to 2007 published by Manson & Solomon (2007).

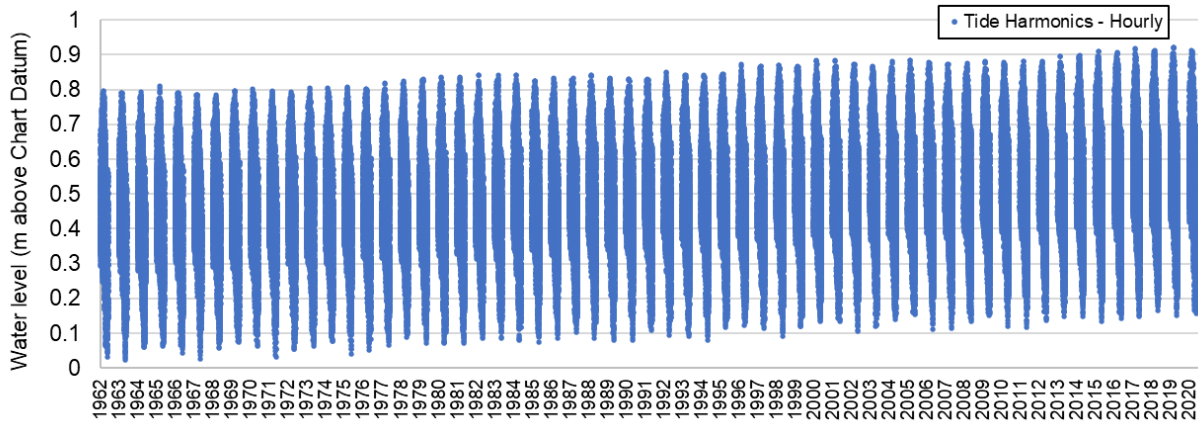


Figure 38 – Output of harmonic analysis for Tuktoyaktuk tide gauge in meters above Chart Datum.

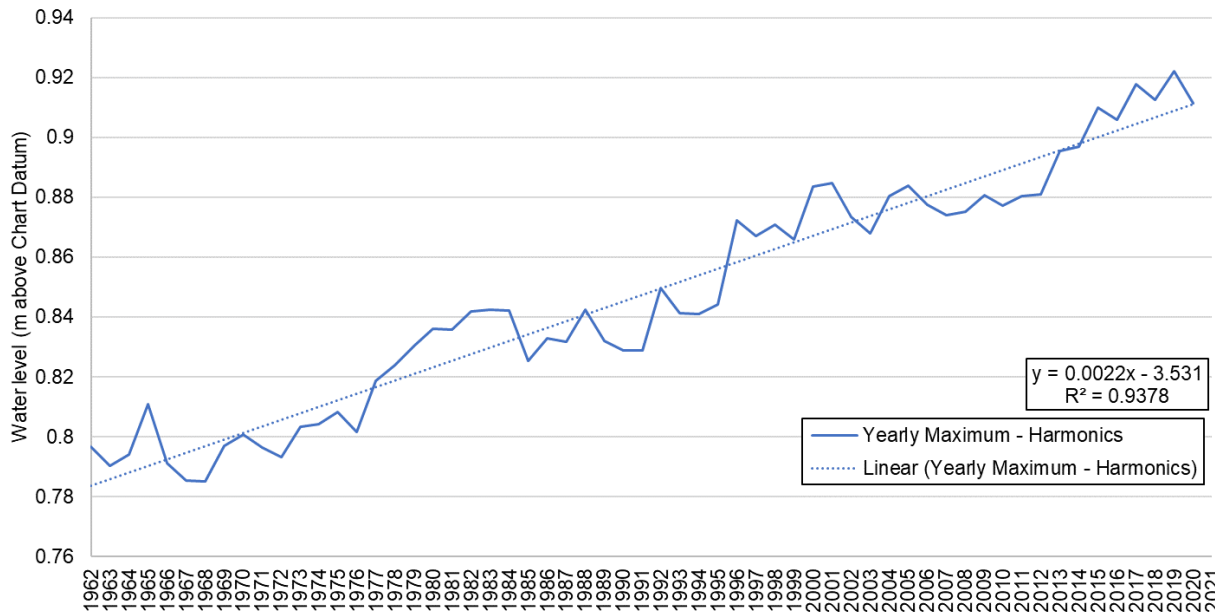


Figure 39 – Yearly maximum tide height and linear trend in meters above Chart Datum derived from the harmonic analysis.

The adopted Mean Highest Astronomical Tide (MHAT) water level was 0.92 m above chart datum (0.31 m in CGVD2013) and a value of SD of 0.02 m (SD_{Tide}) obtained from UTide summary output. The water level used to define the MHAT was obtained by computing the mean of the maximum tide height of the years 2017 to 2020. The yearly maximum values are represented in Figure 39 and occur usually between mid-July to mid-August.

5.3. Storm Surge Analysis

The hourly residual water levels in Figure 40 were then used in the extreme event Gumbel analysis that requires the highest water level recorded by year.

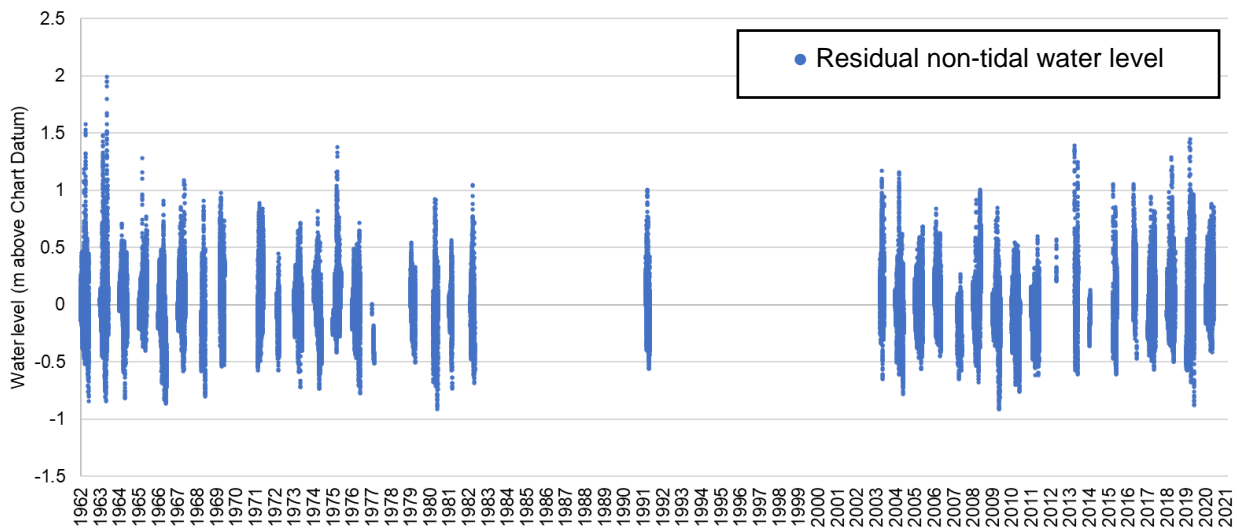


Figure 40 – Residual non-tidal hourly water level plotted after removing the astronomical tide and MSL obtained by harmonic analysis.

The non-exceedance probability plot and the quantile-quantile plot (Figure 41) reflect the significant gaps in data and inputs with similar water levels by the two slight deformities between quantiles 0.7 and 1.2.

The outputs from the Flood Frequency Distribution (FFD) package for the Gumbel distribution (Benkaci, 2021) are represented in Figure 42. The values used for flood mapping were the average values of 50-year return period and 100-year return period and correspond to 1.9 and 2.1 m, respectively. The uncertainty associated to the Gumbel distribution was set as the SD derived from the 95% confidence interval and a value of 0.35 and 0.44 m ($SD_{Storm Surge}$) to represent the higher uncertainty, larger intervals, of higher return periods. The storm surge water levels obtained for different return periods are summarized in Table 4. Distribution parameters, correlation coefficient and $RMSE_{Gumbel}$ extracted from FFD are summarized in Table 5.

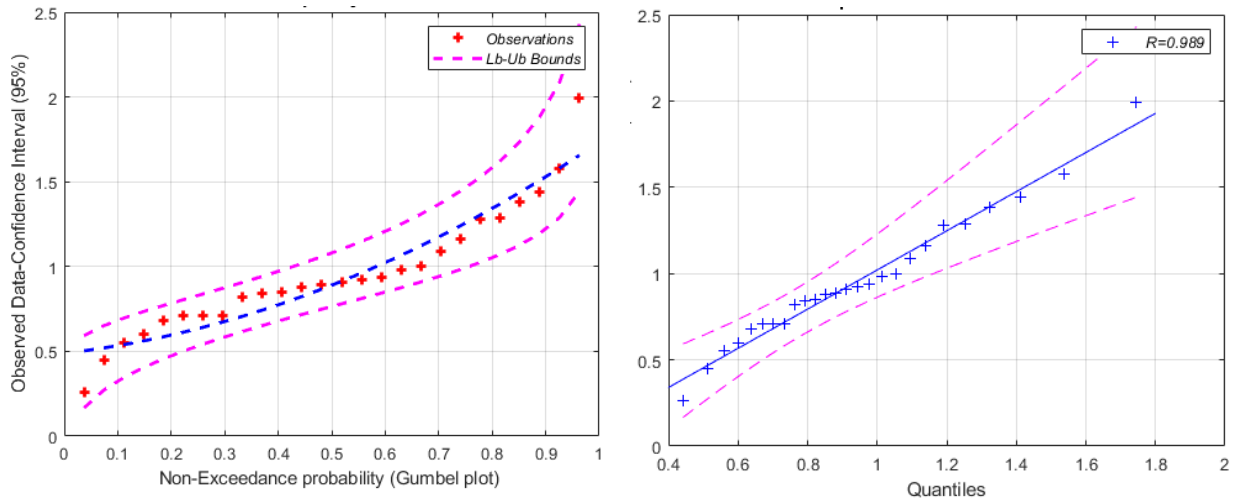


Figure 41 – Gumbel frequency distribution and QQ-plot from the Gumbel distribution.

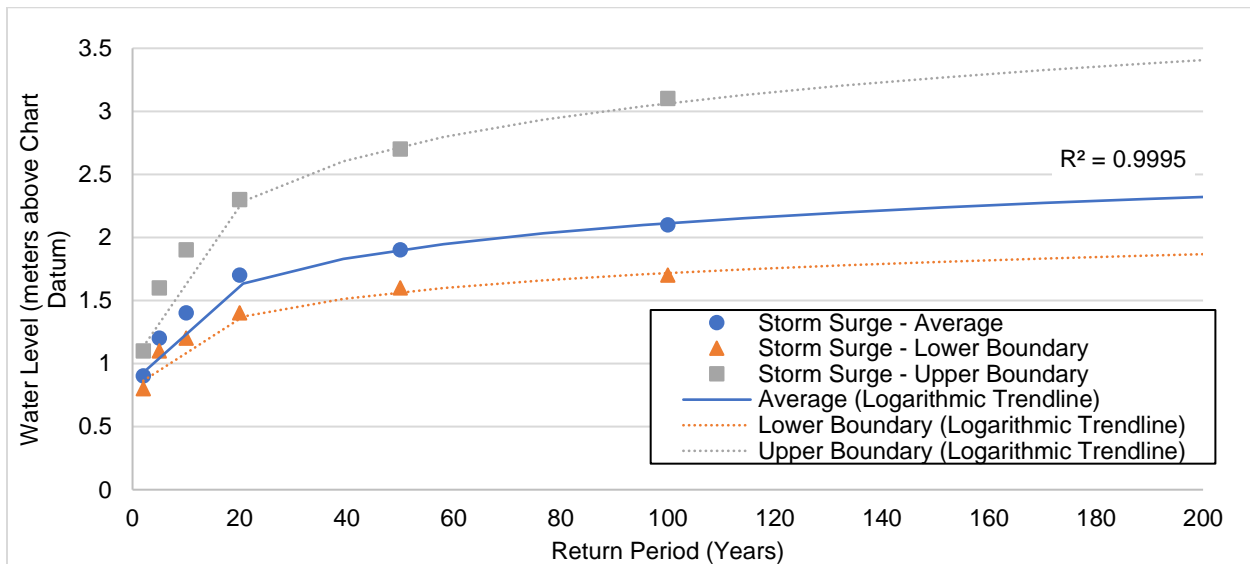


Figure 42 – Gumbel distribution output of the storm surge water levels obtained from MATLAB Flood Frequency Distribution package.

Table 4 – Average storm surge water level by return period with a 95% confidence interval.

Return Period (years)	Non-Exceedance Probability	Quantile (%)	Lower Boundary	Upper Boundary
2	0.5	0.9	0.8	1.1
5	0.8	1.2	1.1	1.6
10	0.9	1.4	1.2	1.9
20	0.95	1.7	1.4	2.3
50	0.98	1.9	1.6	2.7
100	0.99	2.1	1.7	3.1
500	0.998	2.6	2.1	3.9
1 000	0.999	2.8	2.2	4.2
10 000	0.9999	3.5	2.7	5.3

Table 5 – Gumbel distribution summary output.

Gumbel Distribution Parameters	a	0.8
	b	0.3
Correlation Coefficient	0.989	
Root Mean Squared Error (RMSE_{Gumbel})	0.07	

5.4. Validation of the Models

5.4.1. UAV Imagery Analysis

The results of the visual validation process of both bathtub and hydrodynamic models for the LiDAR and UAV elevation datasets are presented as a summary, due to the high number of point-by-point analysis performed. Figure 43 serves as an example of the validation of the bathtub model for the points 1 and 4 for the LiDAR DEM (A) and UAV DSM (B) highlighting the differences between the outputs as the UAV produces a centimetric alignment with the manually digitized shoreline interface. The water surface simulated by the bathtub model on the LiDAR DEM shows precise positioning along the shoreline segment, even with a 1 x 1 m cell size, but the main difference resides in the flood probability classes returned by each elevation dataset. The UAV displays an almost perfect alignment with the shoreline feature, with hazard classes 5 and 4 limiting the water surface, while the LiDAR data outputs a similar flooded extent, the hazard classes range from 2 to 3 in both sides of the water-land interface. The phenomenon illustrated in Figure 43 is verified in the majority of the points used for validation (1, 2, 4, 5, 12, 19, 20, 22, 23, 29 and 30) with hazard class 4 and 5 describing almost perfectly the shoreline, however there are exceptions where the hazard class that better describes the shoreline feature drop to 3 or even 2, that is the case of points 11, 14, 15, 16 and 17 that are all located in central sector of the study area facing north, indicating that, especially in this area, all the probability classes should definitely be considered for flood mapping. For all the points validated the LiDAR only matched the water surface with classes not higher than 3 although the simulated water surface showed an overall accuracy as depicted in Figure 43 and not exceeding 5 m further inland from the shoreline.

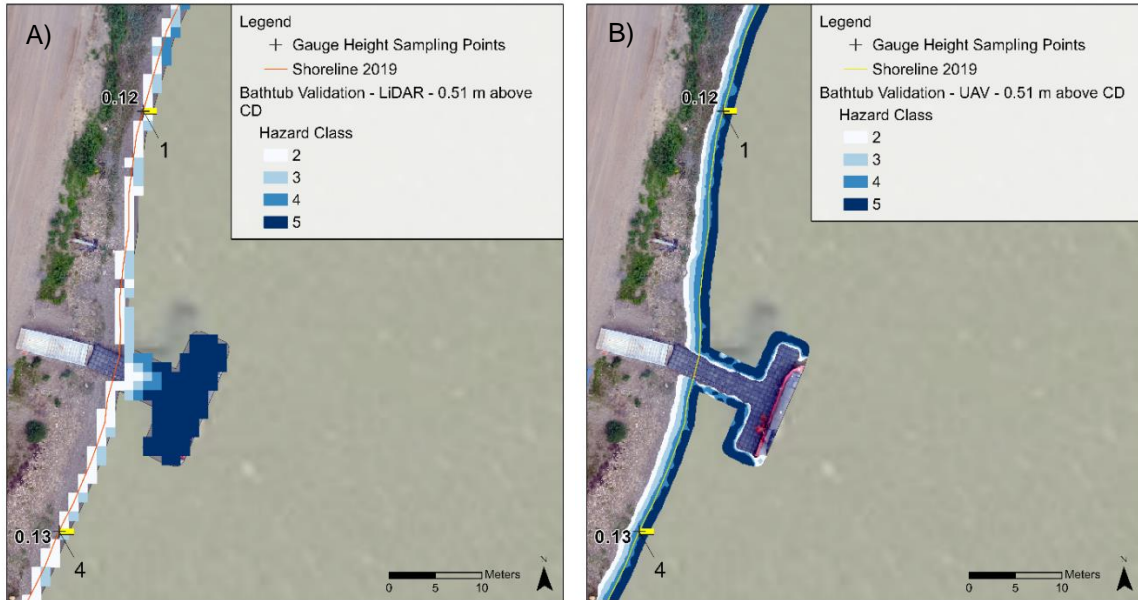


Figure 43 – Bathhtub model validation and shoreline prediction for sampling points 1 and 4. A) LiDAR DEM. B) UAV DSM

Figure 44 illustrates the accuracy of MOHID coupled with LiDAR (A) and UAV (B) elevation datasets for the validation points 15 and 16 showing the situation when, due to the resampling algorithm used in changing cell sizes to 5 x 5 m, the flooded extents are extremely similar, where only 3 cells differ, with the LiDAR flooding additional 75 m². The hydrodynamic model ran on both elevation datasets returned very similar extents for the remaining shoreline of the study area with a precision such as the one illustrated in Figure 44. The UAV model only estimated flood extents further inland when compared to the LiDAR surrounding point 5 in Flagpole Point, where it is known that the UAV typically shows elevation values below the LiDAR DEM. The simulated extents for the points and surrounding shoreline segments analysed did not show deviations from the shoreline polyline feature higher than 15 m for both UAV and LiDAR.

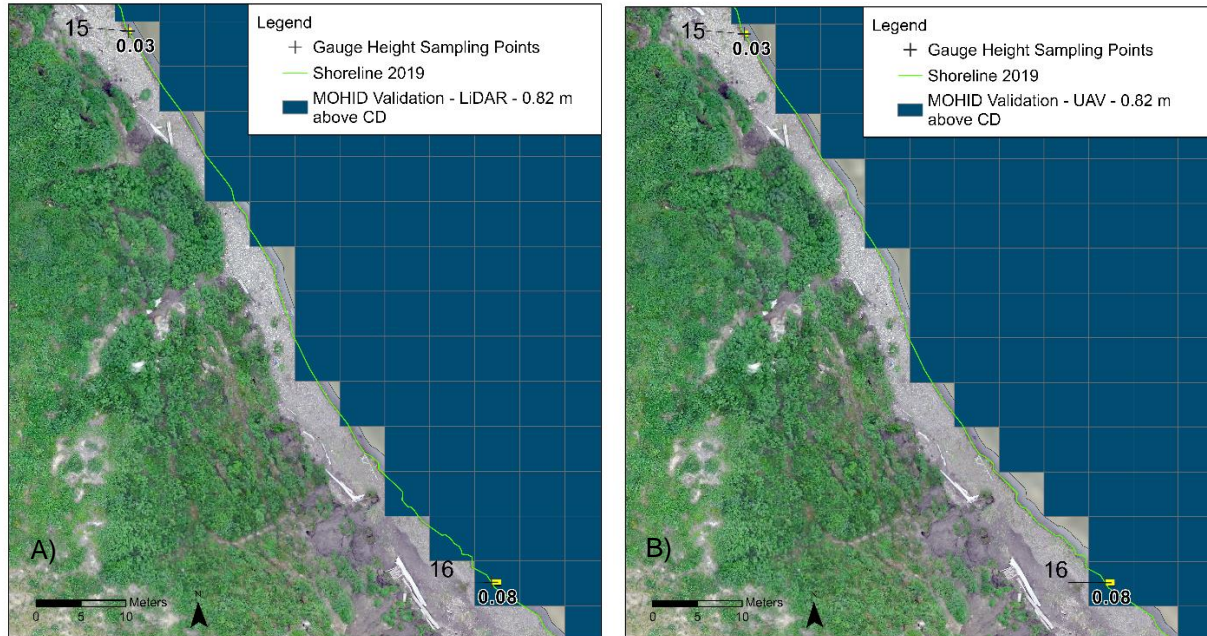


Figure 44 - MOHID validation and shoreline prediction for sampling points 15 and 16. A) LiDAR DEM. B) UAV DSM.

5.4.1. Storm Surge Time-lapse Analysis

a) Flood event: 4th of August 2019

It is possible to differentiate the water level caused by the storm surge from the wave set-up and run-up by using as reference the water level of the inner bay. Both models create a highly detailed and accurate representation of the water surface. The circle shapes were used as reference points to aid the comparison of the different models. In the distance it is possible to see a small strand close to the buildings in Figure 45 that gets flooded by the water level registered at 17:40. Both models show an accurate flood extent up to the patch of grass. There is a noticeable difference in the output flood maps. The LiDAR DEM produces an evident overestimation compared to the UAV DSM,

Figure 46 A) and C), in the bathtub model. This overestimation is higher in the bathtub model. The hydrodynamic model provided similar results on both UAV and LiDAR datasets for this event.

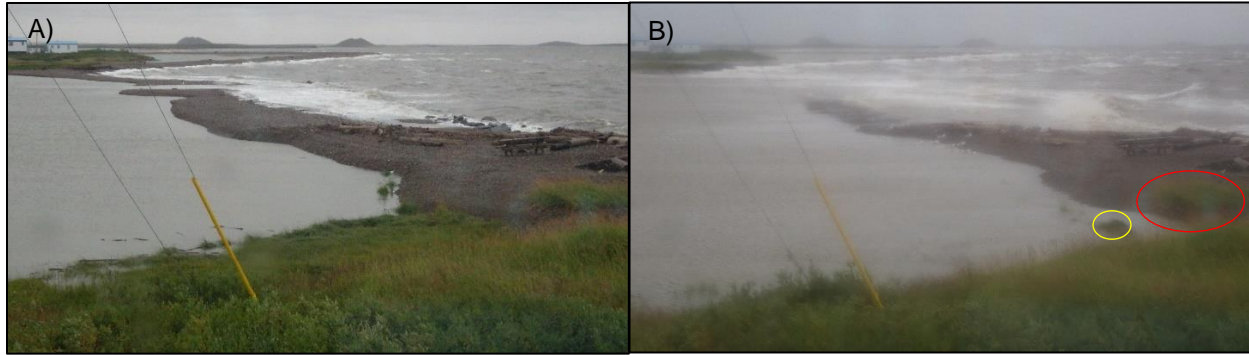


Figure 45 – Time-lapse pictures taken during the storm surge event on the 4th of August 2019. A) 07:05. B) 17:40. (Local time)

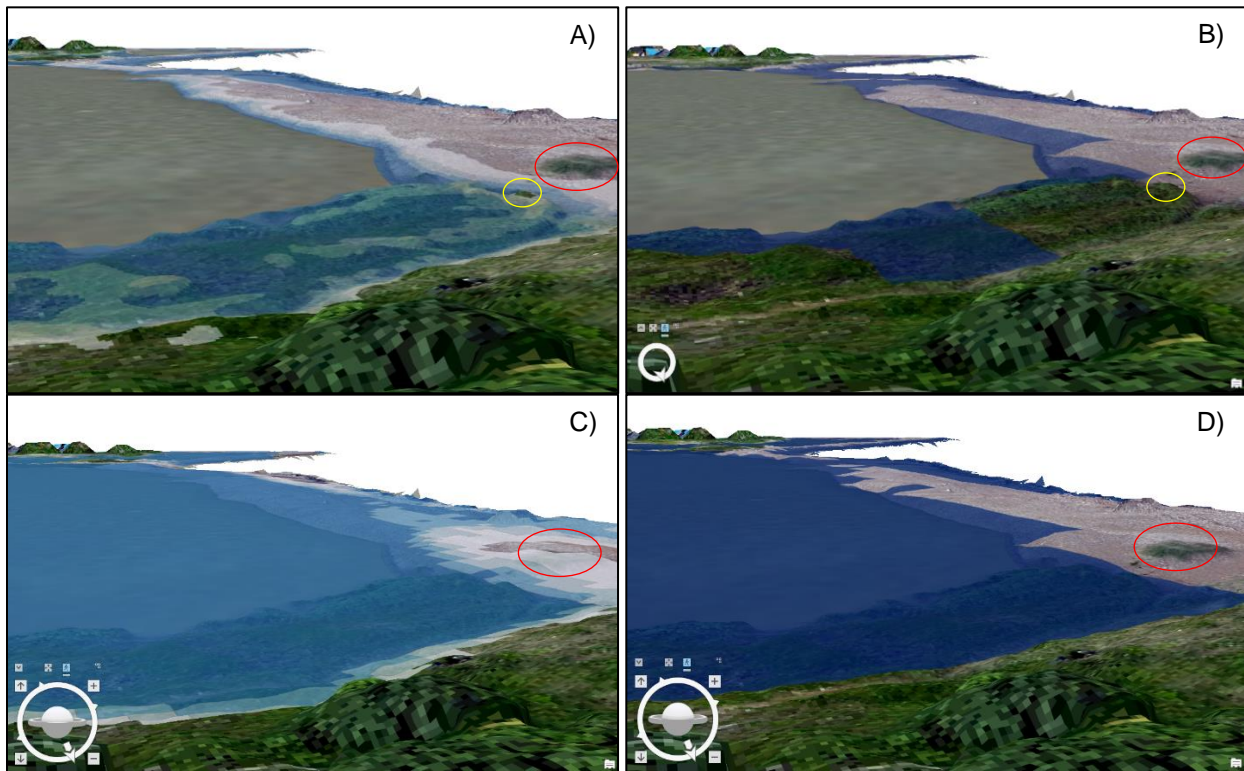


Figure 46 – Results of both flood models ran on the different elevation datasets rendered in ArcGIS Pro at the time-lapse camera position for the water-level read at 17:40. A) Bathhtub model and UAV DSM. B) MOHID and UAV DSM. C) Bathhtub model and LiDAR DEM. D) MOHID and LiDAR DEM.

b) Flood event: 5th of August 2019

It is possible to see in the yellow circled areas (Figure 47 and Figure 48) the increased detail and accuracy of the UAV surface model depicting the tallest vegetation above the water level with a lower probability class than 5. The same result is visible where the road is flooded, estimated with probability classes of 5, 4 and 3, versus a class 2 of the LiDAR dataset over a larger extent. Figure 49 shows an example where the LiDAR model is not able to achieve the same quality of results as the UAV DSM. Despite its tendency to over-estimate flooded areas, in this specific location, the less accurate elevation leads to the creation of an

unconnected area that is floodable by the given water level but discarded due to no hydrological connectivity.



Figure 47 – Picture taken on Tuktu Road by Kitti Hall on the 5th of august 2019 at 9:47 AM (GMT -6:00) during a storm surge event with a water level of 1.39 m above Chart Datum.

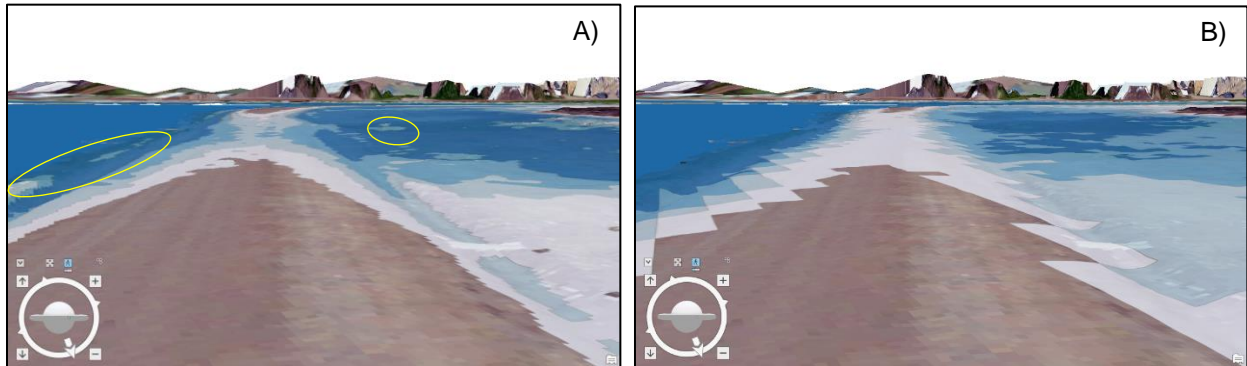


Figure 48 - Bathtub model output for the same water level as Figure 47 by hazard class, rendered in ArcGIS Pro. A) UAV DSM B) LiDAR DEM

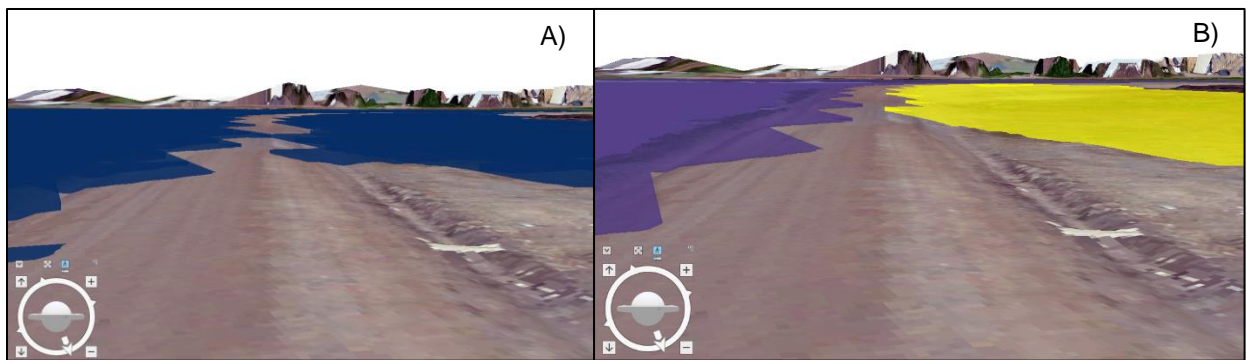


Figure 49 - Hydrodynamic model output at the same location and same time as Figures 64 and 65, rendered in ArcGIS Pro. A) UAV DSM. B) LiDAR DEM. The yellow polygon represents an unconnected area, therefore classified as not flooded.

5.4.2. Historical Flood Event: 1963 – Highest Water Level Recorded

The results of using the uppermost limit of the driftwood located in the study area, which is assumed as representing this extraordinary flood event, is represented for the bathtub model in Figure 50 for both elevation datasets.

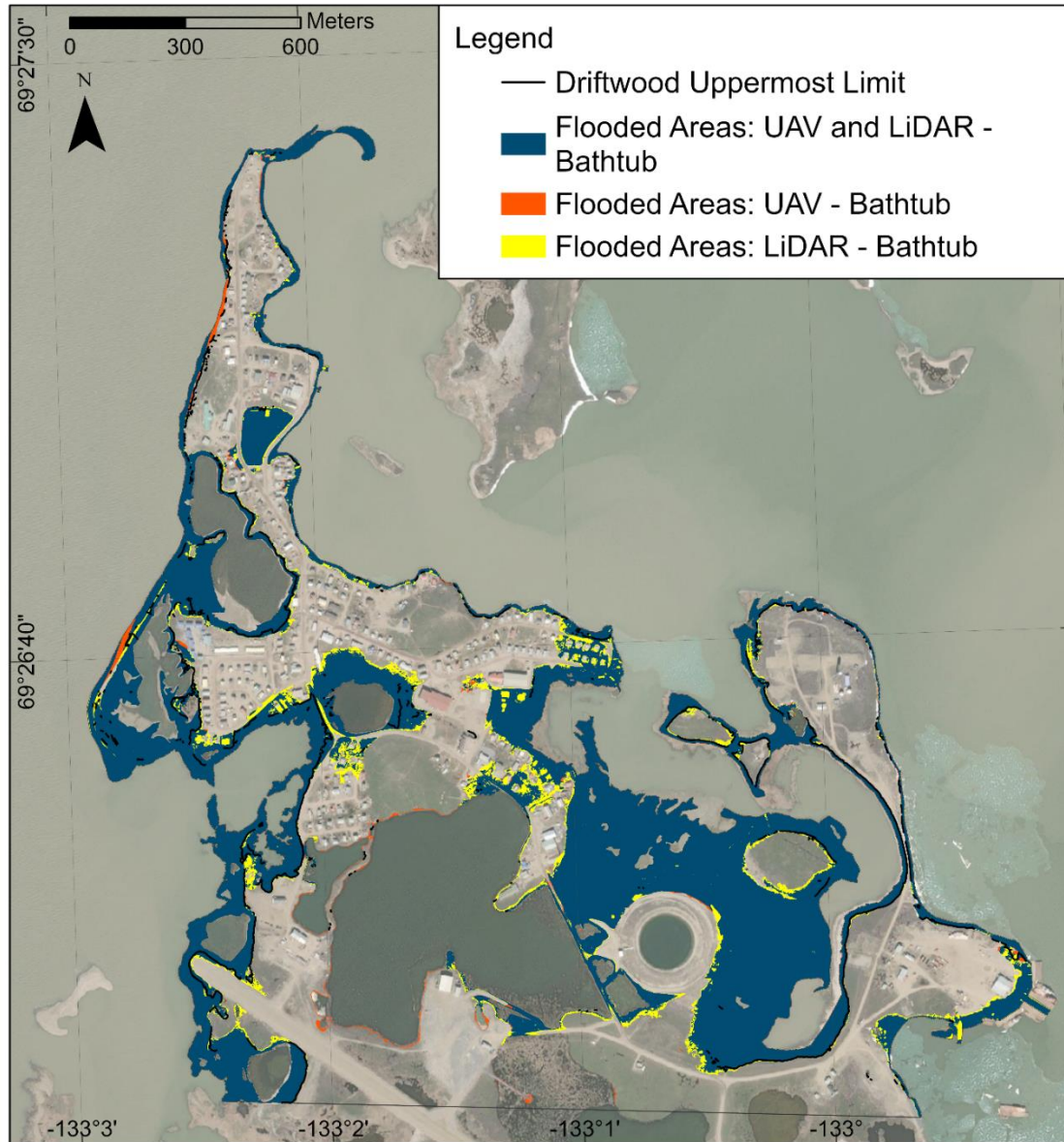


Figure 50 – Bathtub model output for UAV DSM, LiDAR DEM and the areas estimated by both datasets for all hazard classes (2 to 5), for the water level of 2.23 m above CD registered at 2:00 PM on 4/10/1963.

Figure 50 shows that the flooded areas obtained by the bathtub model applied on both elevation datasets correspond with great accuracy, to the uppermost limit of the driftwood. There are no significant driftwood features above the estimated flooded areas, and in many locations the uppermost limit of the flooded areas aligns, with centimetric precision, with the debris.

To illustrate the accuracy of both elevation datasets a side-by-side comparison of the UAV and LiDAR outputs is showed in Figure 51. The north-western coastline segment shows a significant number of mismatching points near Flagpole Point. This area is particularly exposed to strong winds and wave action that combined with the high slopes may result in higher wave run up that can push the driftwood debris higher and further inland. Both models perform similarly in terms of the total number of matching points, the UAV identified 85.5% and LiDAR 86.1% from a total of 106 333 points. While the LiDAR identifies a higher total number of matching points due to the larger flood extent caused by higher overall uncertainty value, the UAV model can identify more flooded points in the class with flood probability of >80% (Figure 52).

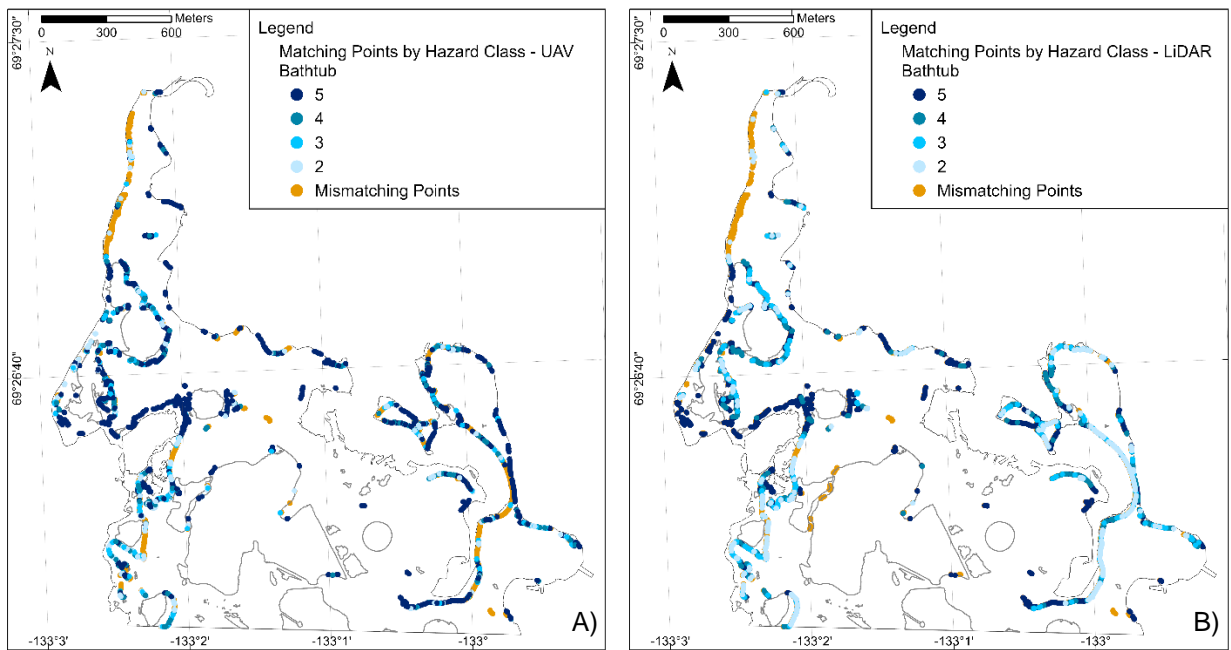


Figure 51 – Matching driftwood locations by hazard class and mismatching points for the bathtub model for the water level of 2.23 m above CD registered at 2:00 PM on 4/10/1963. A) UAV DSM and B) LiDAR DEM.

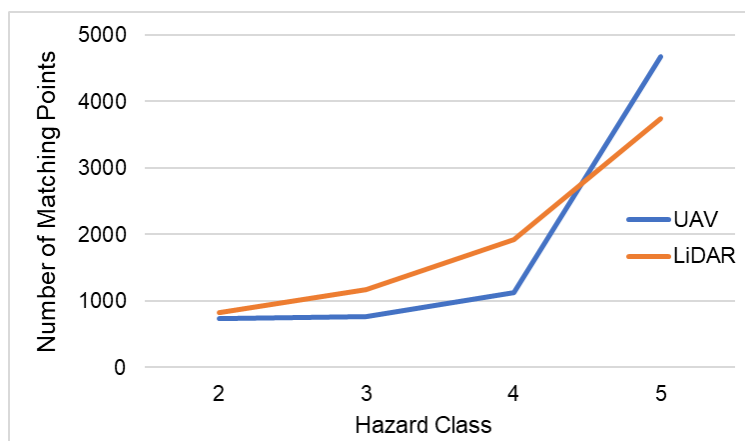


Figure 52 – Number of driftwood points identified as matching points by the elevation dataset and by hazard class for the bathtub model.

The analysis performed for the bathtub model was replicated for the hydrodynamic model and the results are illustrated in Figure 53 . The model ran on the UAV DSM identified 8 494 (87.5%) points and the LiDAR 9428 (88.7%) from a total of 106333 driftwood points. Both elevation models show that most of the mismatches occur around Flagpole point, also seen in the bathtub model. Despite the incorporation of a wave module to simulate and include wave run up could increase the matching rate surrounding Flagpole point, all the models performed well by successfully marking the driftwood debris as flooded, with the UAV bathtub model being the most conservative compared to the other models, but, with higher probability areas identified. The results of both hydrodynamic and bathtub models sustain the possibility of the storm that occurred in 1963, or a storm with a similar magnitude, that was not recorded by the tide gauge, as the highest water level historically registered in Tuktoyaktuk.

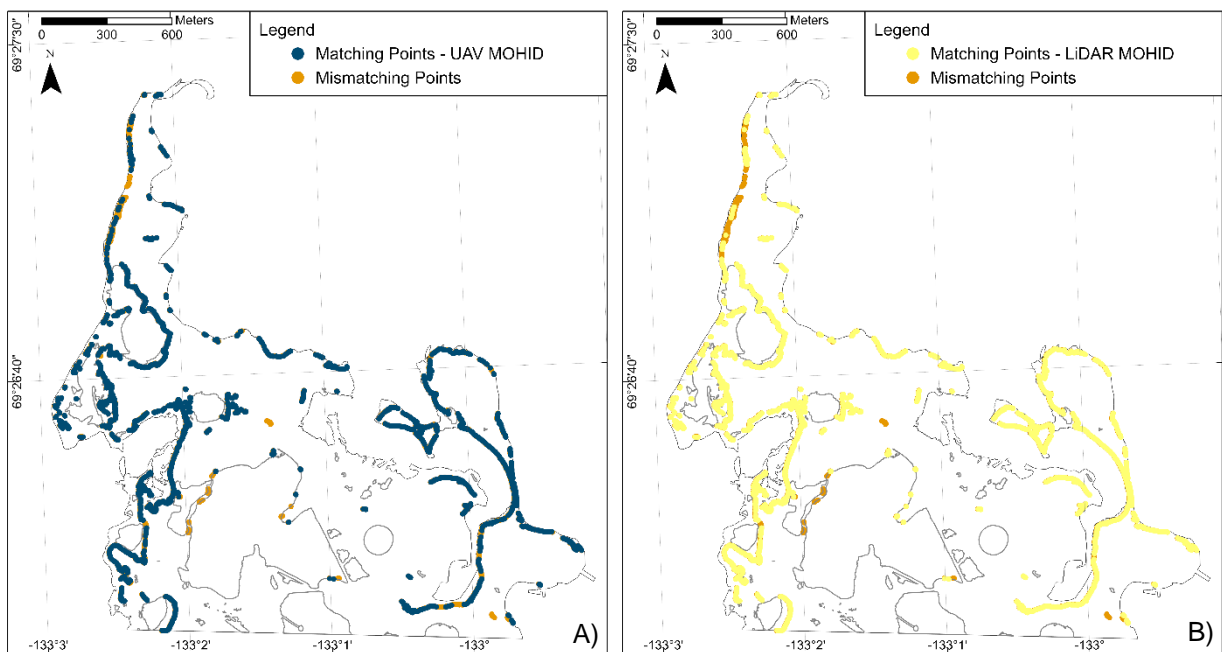


Figure 53 - Matching driftwood locations and mismatching points for the hydrodynamic model for the water level of 2.23 m above CD registered at 2:00 PM on 4/10/1963. A) UAV DSM and B) LiDAR DEM.

5.5. Sea Level Change and Shore Line Retreat in the 21st Century

Tables Table 6, Table 7, Table 8 and Table 9 summarize the computed inputs for bathtub and hydrodynamic models. Tables Table 7 and Table 9 include the water level measured at 69°26'19.18"N 132°59'36.51"W and Δ , in m, which represents the difference between the imposed tide water level and the model output for each epoch. The registered differences between the input and the output water surface level ranged from 3 to 7 mm for the hydrodynamic model.

Table 6 – UAV DSM bathtub model inputs used for the sea level rise simulations by scenario, all SD values are in m.

Scenario	Year	Water Level Input (m CGVD2013)	σ Scenario	σ Chart Datum to CGVD2013	σ Tide	σ Total
	2020	0.31		0.15	0.02	0.19
RCP 4.5	2060	0.54	0.07	0.15	0.02	0.20
	2100	0.79	0.14	0.15	0.02	0.24
RCP 8.5	2060	0.58	0.07	0.15	0.02	0.20
	2100	0.99	0.14	0.15	0.02	0.24

Table 7 – UAV DSM hydrodynamic model water level inputs and outputs for the sea level rise simulations by scenario.

Flood Scenario	Year	Mean Highest Astronomical Tide (m above Chart Datum)	Sea Level Rise (m)	Storm Surge Water Level (m)	Water Level (m above Chart Datum)	Water Level Input (m - CGVD2013)	Model Output (m - CGVD2013)	Δ (m)
	2020		0.00		0.92	0.31	0.31	-0.004
RCP 4.5	2060	0.92	0.23	0	1.15	0.54	0.54	-0.005
	2100		0.49		1.40	0.79	0.79	0.005
RCP 8.5	2060	0.92	0.27	0	1.19	0.58	0.58	-0.003
	2100		0.69		1.60	0.99	0.99	0.007

Table 8 – LiDAR DEM bathtub model inputs used for the sea level rise simulations by scenario, all SD values are in m.

Scenario	Years	Water Level Input (m CGVD2013)	σ Scenario	σ Chart Datum to CGVD2013	σ Tide	σ Total
	2020	0.31		0.15	0.02	0.29
RCP 4.5	2060	0.54	0.07	0.15	0.02	0.30
	2100	0.79	0.14	0.15	0.02	0.33
RCP 8.5	2060	0.58	0.07	0.15	0.02	0.30
	2100	0.99	0.14	0.15	0.02	0.33

Table 9 – LiDAR DEM hydrodynamic model water level inputs and outputs for the sea level rise simulations by scenario.

Flood Scenario	Year	Mean Highest Astronomical Tide (m above Chart Datum)	Sea Level Rise (m)	Storm Surge Water Level (m)	Water Level (m above Chart Datum)	Water Level Input (m - CGVD2013)	Model Output (m - CGVD2013)	Δ (m)
	2020		0.00		0.92	0.31	0.31	-0.004
RCP 4.5	2060	0.92	0.23	0	1.15	0.54	0.54	-0.004
	2100		0.49		1.40	0.79	0.79	0.007
RCP 8.5	2060	0.92	0.27	0	1.19	0.58	0.58	-0.003
	2100		0.69		1.60	0.99	0.99	0.007

Figure 54 illustrates the total sum, in m², of the flooded areas computed by each model, by scenario and by elevation dataset. The “all classes” represents the total sum of the areas identified as hazard classes 2, 3, 4 and 5. The values for 2020 do not correspond to any RCP scenario, since there is no effect of sea level rise. Instead, the computed areas set the baseline for the comparison of the models based on the mean highest astronomical tide value of 0.92 m above CD.

The total flood extent obtained by the bathtub model is higher than by MOHID for every simulation, especially for the years 2060 and 2100 because of sea level rise projections that introduce more uncertainty to the model as it increases in the inundated areas of lower probabilities by also increasing the effective water level for each different hazard class. For the year 2020, MOHID estimates that the percentage of the study area flooded is 7.7 and 9.1% for the UAV and LiDAR models respectively, while the bathtub model values are 16.3% for the UAV and 19.5% for LiDAR. In 2060, for the scenario RCP4.5, the difference between the hydrodynamic model results and the bathtub increases when compared to 2020, MOHID predicts 8.9 and 10.6% for the UAV and LiDAR, respectively, but the bathtub model outputs 22.4% for the UAV and 25.7% for the LiDAR. The same trend is visible for the RCP8.5, representing 9.3% for UAV and 11% for LiDAR in MOHID, compared to the bathtub's 23.5 and 26.6 % for UAV and LiDAR, respectively. For the flooded areas predicted for the year of 2100, the same trend applies, where the hydrodynamic model (RCP4.5) returns 14.4 and 16.8% of the study area flooded for the UAV and LiDAR, respectively, and 16.1 and 18.8% for RCP8.5. The bathtub model estimates for the scenario RCP4.5 29.2% for the UAV and 31.5% for LiDAR, while the most extreme scenario represented by RCP8.5 shows that the UAV estimates 32.2% and the LiDAR 35.9% of the study area as flooded. Figures Figure 55 and Figure 56 show the fraction of total flooded extent for each hazard class by scenario and elevation dataset, by year. The year 2020 is not considered a RCP scenario, since there is no sea level rise. The computed area for class 5 is higher for the UAV DSM, which results from the higher robustness of the UAV data compared to the LiDAR DEM. This occurred in all simulations and is explained by the overall lower uncertainty of the UAV data compared to LiDAR. The model ran on UAV produces an overall smaller extent compared to LiDAR, except for class 5. For the year 2020 a total of 273 816 m² is computed by for UAV and 327 089 m² for LiDAR, where the most notable differences are explained by the changes in the western beach profile from 2004 to 2018 and the intertidal areas surrounding the water reservoir.

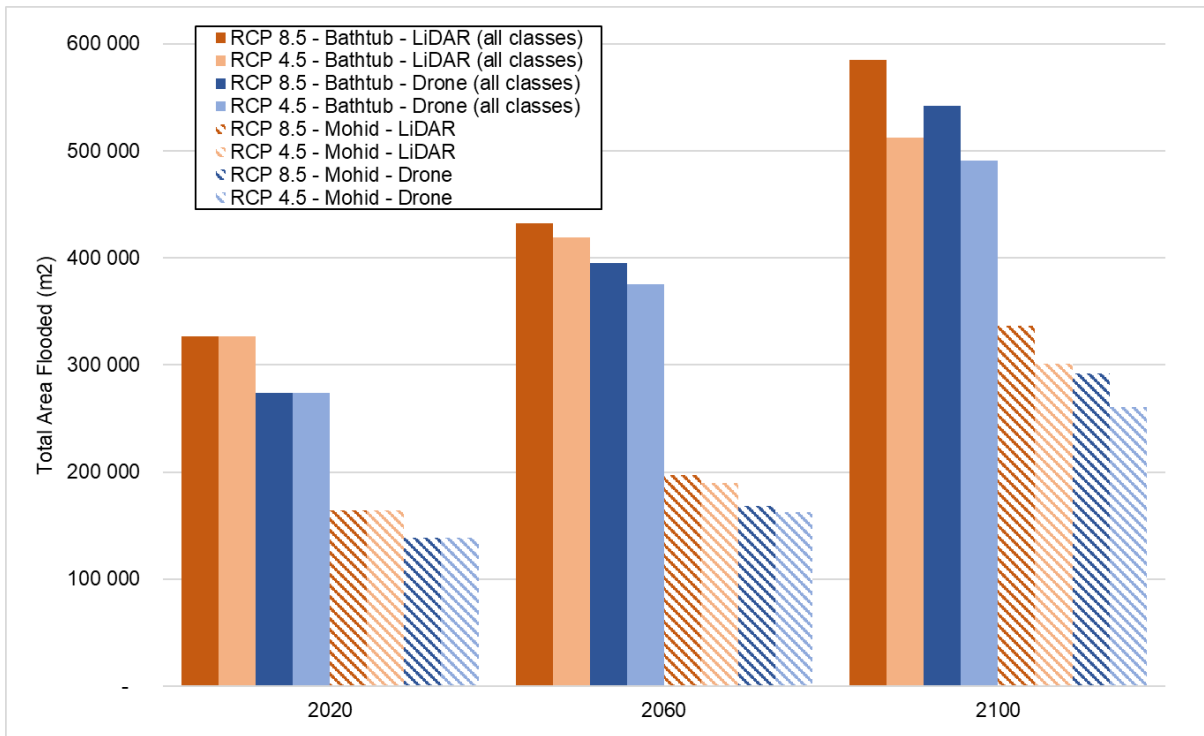


Figure 54 – Comparison of the total area flooded (m²) of both models for LiDAR and UAV by scenario. The year 2020 does not correspond to any RCP scenario and only represents the mean highest astronomical tide added to the 2020 mean sea level. The “all classes” classification stands for the grouping of the hazard classes from 5 to 2.

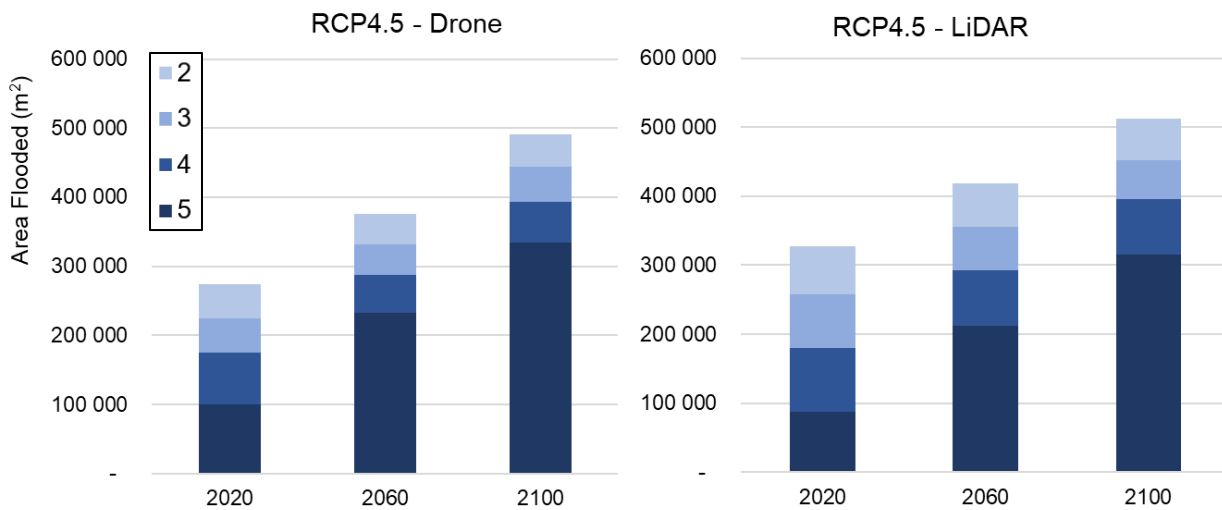


Figure 55 – Bath tub model results comparison between the total area flooded by hazard class for the RCP4.5 scenario.

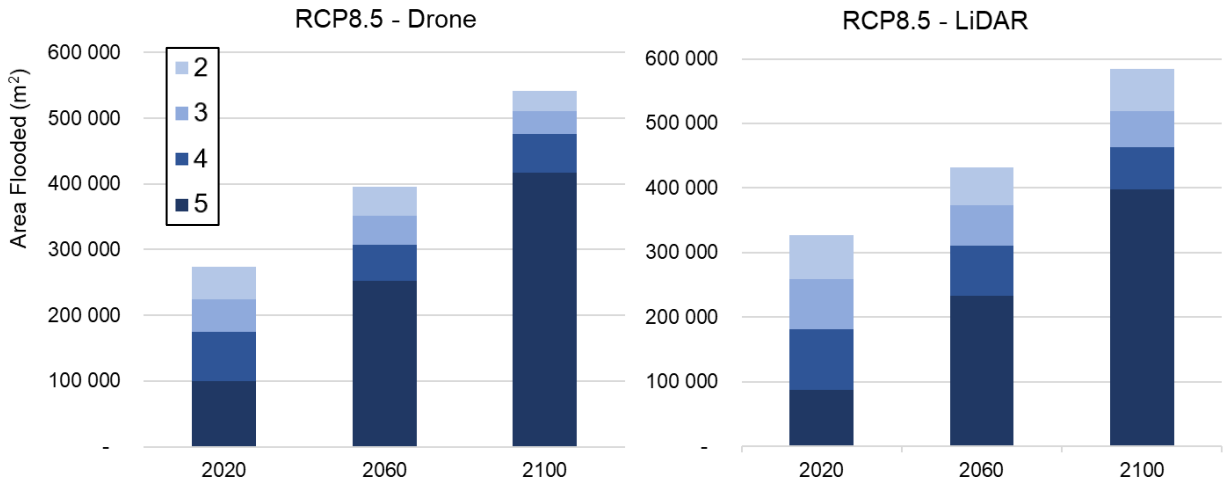


Figure 56 - Bathtub model results comparison between the total area flooded by hazard class for the RCP8.5 scenario.

Figure 57 and Figure 58 show that the predicted flooded areas have similar extents for classes 4 and 5, but for the LiDAR elevation dataset, classes 2 and 3 cover more area compared to UAV. This is more evident in scenario RCP8.5 due to higher values of uncertainty associated with the modelled scenario, represented as 1 and 2 in Figure 58. The differences stated in the analysis for the year 2020 are still visible in the western beach area, where the LiDAR floods a larger area compared to the UAV. Even for the RCP8.5 scenario, the beach extent is not considered as flooded by the UAV DSM. The differences between UAV and LIDAR outputs for the year 2100 and the scenario RCP8.5 on the bathtub model are available in the Appendix (see Figure A 5). There are a few areas where only the UAV model classifies as flooded namely a small extent by the water reservoir and the sports field.

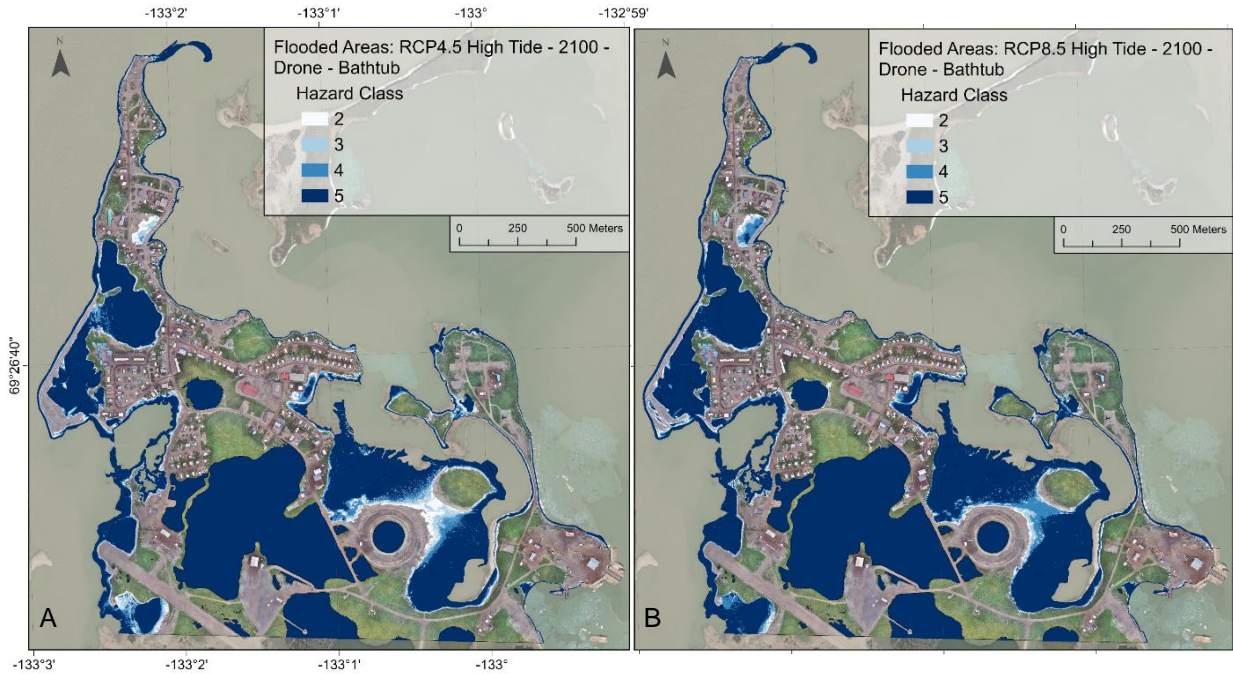


Figure 57 –Bathtub model predicted highest astronomical tide for the year 2100 by hazard class on UAV DSM. A) RCP4.5 and B) RCP8.5

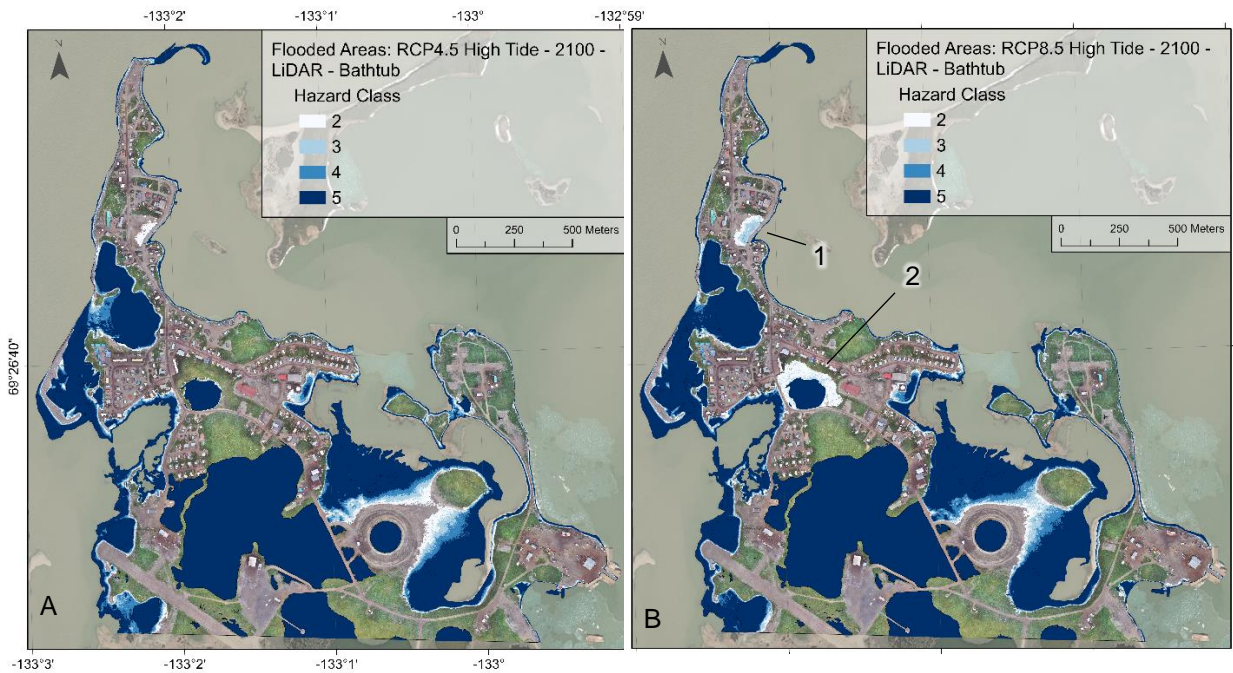


Figure 58 – Bathtub model predicted highest astronomical tide for the year 2100 by hazard class on LiDAR DEM. A) RCP4.5 and B) RCP8.5.

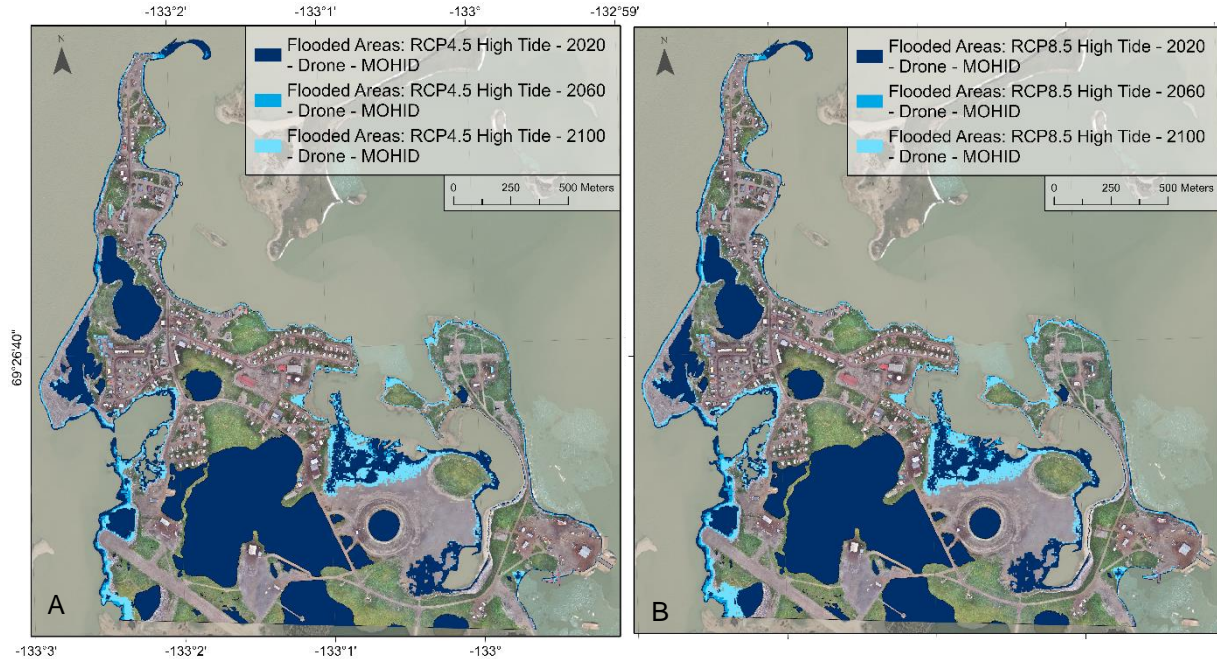


Figure 59 - Hydrodynamic model predicted highest astronomical tide in 2020 and for 2060 and 2100 based on the UAV DSM. A) RCP4.5 and B) RCP8.5.

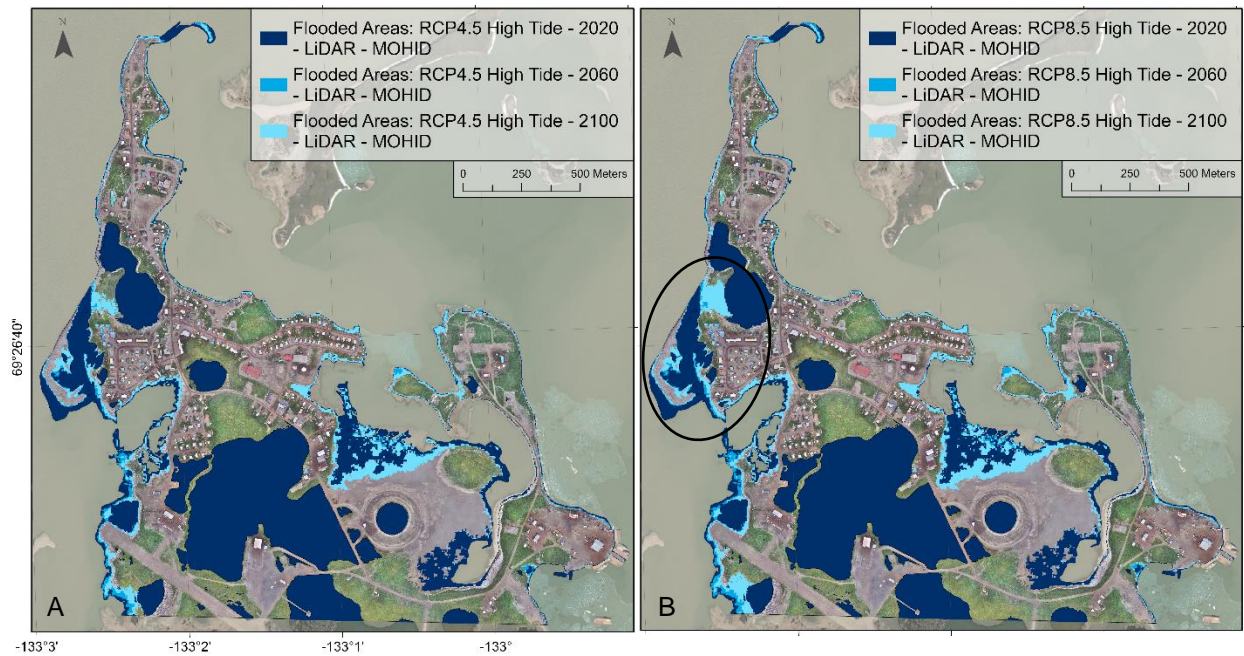


Figure 60 - Hydrodynamic model predicted highest astronomical tide in 2020 and for 2060 and 2100 based on the LiDAR DEM. A) RCP4.5 and B) RCP8.5.

The results of the hydrodynamic model for 2100 coincide with the uppermost limit of hazard class 3 of the bathtub model outputs for the current flooding events. This means that the estimated sea-level rise in 2100 will generate a permanent situation, at least as bad as the current flooding events, and without considering the coastal erosion effects, nor the effects of the isostatic subsidence and permafrost degradation. The

differences in the water surfaces generated from UAV and LiDAR for both hydrodynamic and bathtub approaches are represented in Figure 61. While the hydrodynamic model overlaps the bathtub model classes 5 to 3 in the majority of the coastline, exceptions are found around the water reservoir, Kitt Hall and the sports field, where the bathtub model (for both UAV and LiDAR datasets) shows high probability of flooding, but not the MOHID.

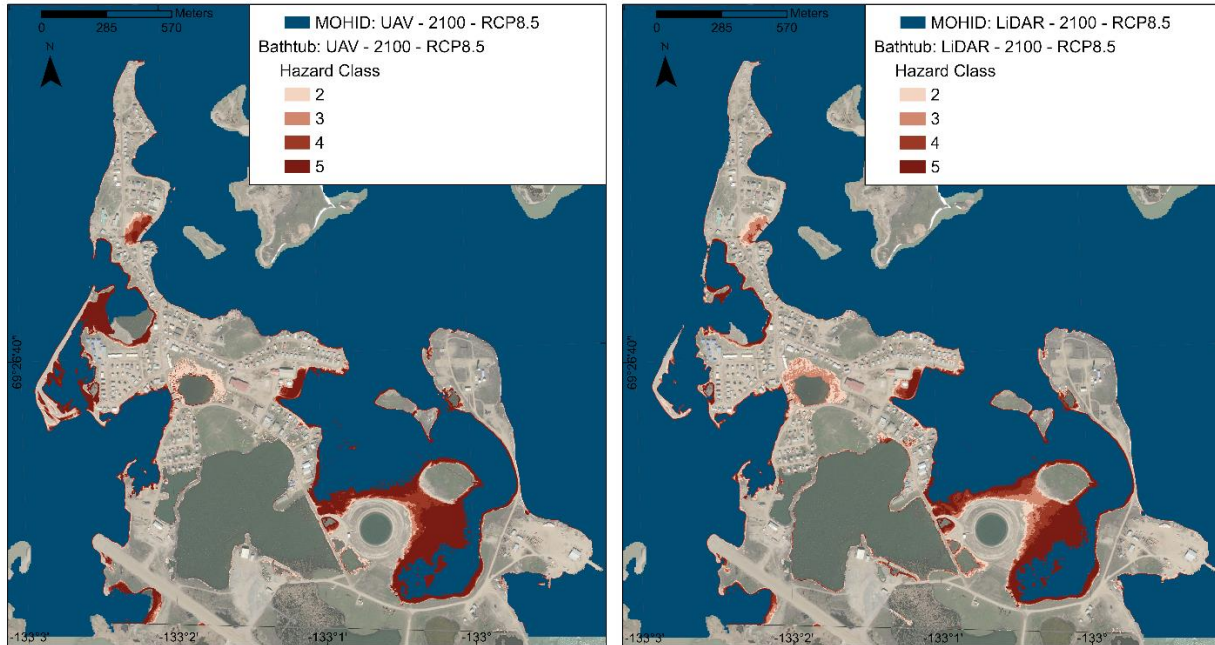


Figure 61 – Differences between MOHID and bathtub models for the year 2100 on a RCP8.5 scenario. A) UAV DSM. B) LiDAR DEM.

5.6. Storm Surge Flood Modelling in the 21st Century

5.6.1.50-year Return Period Storm Surge Event

a) Synthesis of results

Tables Table 10, Table 11, Table 12 and Table 13 summarize the input and output data obtained from the bathtub and hydrodynamic models for the two elevation datasets, when a storm surge event with a 50-year return period is added to the MHAT and sea level rise scenarios RCP4.5 and RCP8.5 are used.

Table 10 – UAV DSM bathtub model inputs used for the sea level rise and a 50-year return period storm surge by scenario.

Scenario	Years	Water Level Input (m CGVD2013)	σ Scenario	σ Chart Datum to CGVD2013	σ Tide	σ Storm Surge	σ Total
	2020	2.21		0.15	0.02	0.35	0.40
RCP 4.5	2060	2.44	0.07	0.15	0.02	0.35	0.40
	2100	2.69	0.14	0.15	0.02	0.35	0.42
RCP 8.5	2060	2.48	0.07	0.15	0.02	0.35	0.40
	2100	2.89	0.14	0.15	0.02	0.35	0.42

Table 11 - UAV DSM bathtub model inputs used for the sea level rise and a 50-year return period storm surge by scenario.

Flood Scenario	Year	Mean Highest Astronomical Tide (m above Chart Datum)	Sea Level Rise (m)	Storm Surge Water Level (m)	Water Level (m above Chart Datum)	Water Level Input (m - CGVD2013)	Model Output (m - CGVD2013)	Δ (m)
RCP 4.5	2020	0.92	0.00	1.9	2.82	2.21	2.21	-0.004
	2060		0.23		3.05	2.44	2.41	0.031
	2100		0.49		3.30	2.69	2.67	0.025
RCP 8.5	2060	0.92	0.27	1.9	3.09	2.48	2.54	-0.061
	2100		0.69		3.50	2.89	2.88	0.015

Table 12 – LiDAR DEM bathtub model inputs used for the sea level rise and a 50-year return period storm surge by scenario.

Scenario	Years	Water Level Input (m CGVD2013)	σ Scenario	σ Chart Datum to CGVD2013	σ Tide	σ Storm Surge	σ Total
RCP 4.5	2020	2.21	0.07	0.15	0.02	0.35	0.46
	2060	2.44		0.15	0.02	0.35	0.46
	2100	2.69		0.15	0.02	0.35	0.48
RCP 8.5	2060	2.48	0.07	0.15	0.02	0.35	0.46
	2100	2.89	0.14	0.15	0.02	0.35	0.48

Table 13 - LiDAR DEM hydrodynamic model water level inputs and outputs for the sea level rise and a 50-year return period storm surge by scenario.

Flood Scenario	Year	Mean Highest Astronomical Tide (m above Chart Datum)	Sea Level Rise (m)	Storm Surge Water Level (m)	Water Level (m above Chart Datum)	Water Level Input (m - CGVD2013)	Model Output (m - CGVD2013)	Δ (m)
RCP 4.5	2020	0.92	0.00	1.9	2.82	2.21	2.21	-0.004
	2060		0.23		3.05	2.44	2.41	0.031
	2100		0.49		3.30	2.69	2.67	0.025
RCP 8.5	2060	0.92	0.27	1.9	3.09	2.48	2.54	-0.061
	2100		0.69		3.50	2.89	2.88	0.015

b) Flood mapping

The total area flooded, in m², for the 50-year return period simulations, reflects the same trend in estimating larger flood extents by both bathtub and hydrodynamic models ran on LiDAR data and smaller inundated areas calculated by MOHID compared to bathtub model. For the year 2020, MOHID, shows that 47.5% of the study area is considered flooded using the UAV and 52.3% for the LiDAR, while the bathtub model results range from 57.1 to 65.8% for the UAV and LiDAR, respectively. In 2100, with a projected sea level rise of 0.69 m for the RCP8.5 scenario, the UAV bathtub model covers 76.2% and the LiDAR 83.7% of the study area with all four hazard classes while the hydrodynamic model, shows a range from 50.6% (UAV) to 59.4% (LiDAR) which correspond approximately to the bathtub model's classes of 4 and 5 combined. The year 2020, as stated in chapter 5.5, does not resemble any RCP scenario, since it represents the highest astronomical tide added to the mean sea level and the 50-year return period storm surge water level of 1.9 m.

Figure 62 illustrates the differences of the total area flooded for 2100 between elevation datasets for the bathtub model. The differences between the LiDAR and the UAV partially reside in the fact that the LiDAR does not include features such as buildings, sheds and sizeable containers used as storage units or even cars and boats that are possible to identify in the UAV DSM. These features are easily identifiable but there are other significant differences across the study area where the LiDAR model inundates further inland, namely, in the island formed south of the water reservoir, around the DEW-Line peninsula and the western shore near the airstrip. Overall, both elevation models show similar uppermost limits for the given flood scenario. The areas where the UAV DSM floods further inland (red) are located primarily in the northern sector of the study area where the average distance from the LiDAR uppermost limit is less than 10 m.

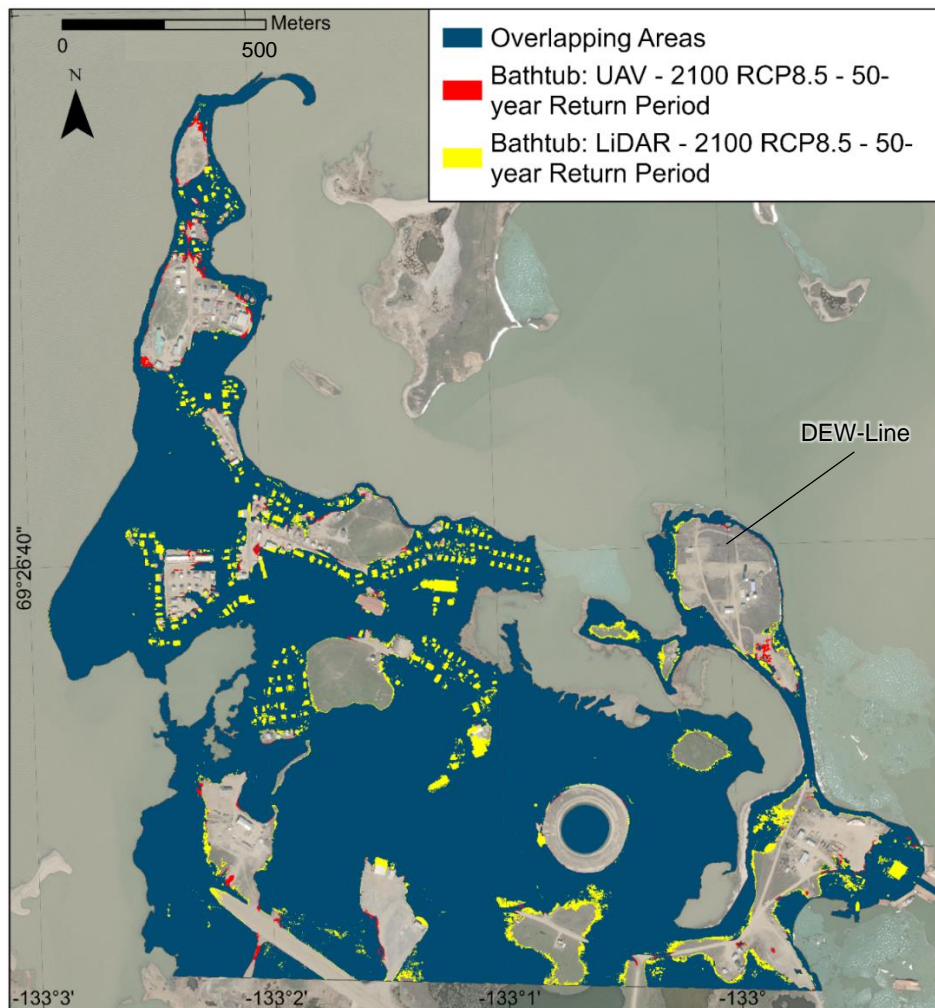


Figure 62 - Comparison between total area flooded by elevation dataset for the bathtub model. The scenario represented is RCP8.5 for the year of 2100 and a 50-year return period storm surge.

The map in Figure 63 represent the outputs of the hydrodynamic model for the 50-year return period storm surge simulations on UAV DSM. The results of the model on both elevation datasets show a significant overlap of the computed flooded extents, following the previous results analysed. For that reason, only the

UAV results are shown from now on. The maps derived from LiDAR data and RCP 4.5 scenario are available in the Appendix (see Figures Figure A 6, Figure A 7 and Figure A 8).

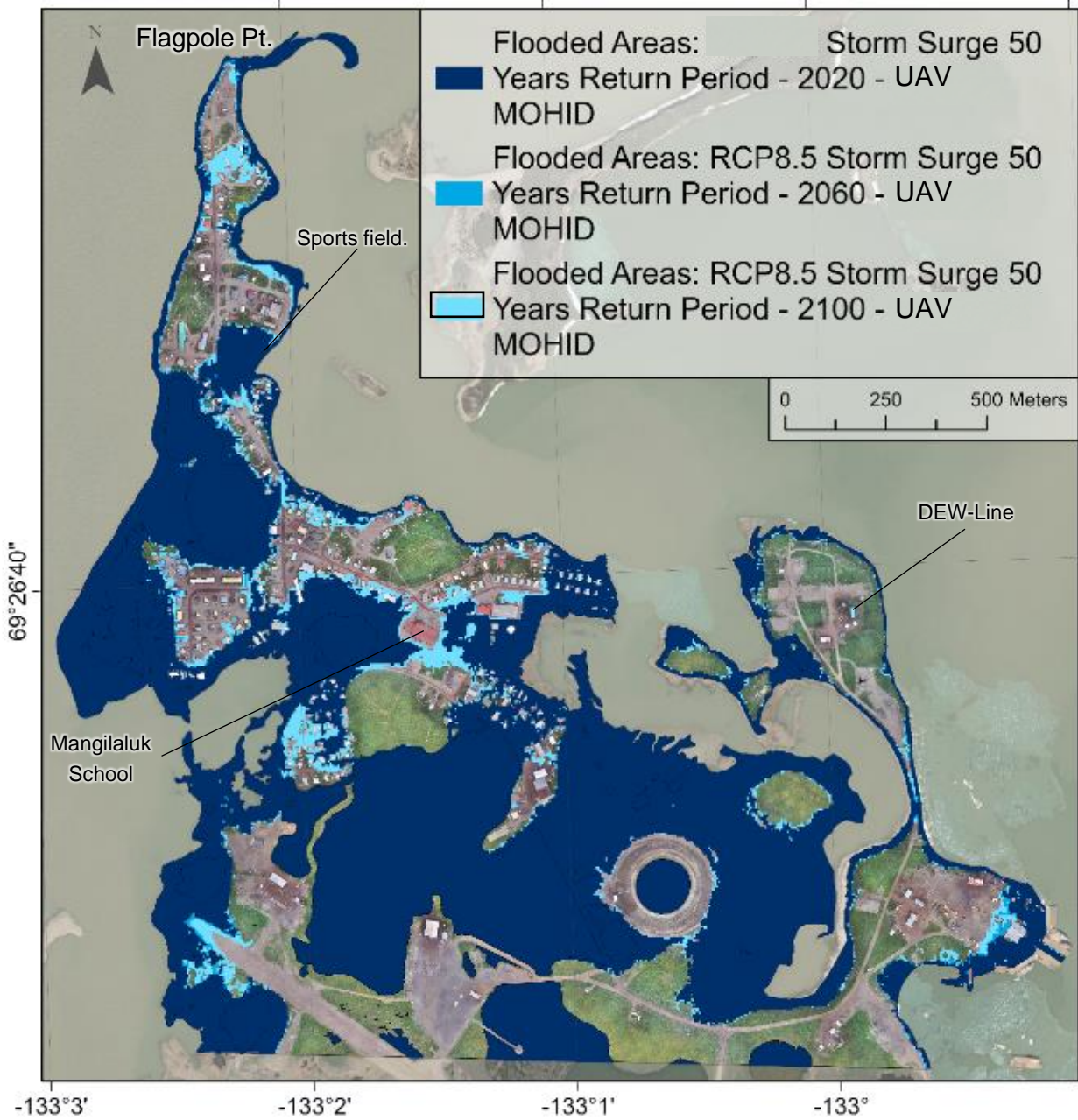


Figure 63 - MOHID flooded areas for 2020, 2060 and 2100 for the RCP8.5 scenario with a 50-year return period storm surge on UAV DSM.

A 50-year return period (1.9 m above CD) storm surge results in a complete separation of Tuktoyaktuk and the DEW-Line peninsula from mainland even in 2020 if synchronized with a high late-summer tide. By 2100, for the scenario RCP8.5 (Figure 63), Flagpole Point becomes isolated, and another breakage is formed by Mangilaluk School, representing the most significant differences between the scenarios RCP4.5 and RCP8.5.

c) Exposure of infrastructure to flooding

The overlay of the flood maps obtained from the UAV surface model and local infrastructure is shown in Figure 64 and Figure 65 for bathtub and hydrodynamic models for the scenario RCP8.5. The results for RCP4.5 are available in the Appendix (see Figure A 14 and Figure A 15). The results from the hydrodynamic model match 82% of the buildings identified by the bathtub model and classified as hazard class 5. but the remaining buildings from class 5 and the ones belonging to hazard classes 2, 3 and 4 by the bathtub model are not considered affected by flooding by MOHID due to the larger extents outputted by the static model, that creates a higher effective flood water level due to the incorporation of uncertainty of each simulation, resulting in a higher total of buildings affected by flooding. The differences between the flood extents obtained by both models and RCP scenarios reflect the differences in the buildings identified by each simulation because it is an overlay of the modelled water surface with the existing building footprints layer. By comparing the results for the year 2100 on a RCP4.5 scenario by affected buildings, it is clear the conservative approach of the bathtub model that can identify 432 individual features, where 280 correspond to a hazard class 5 (> 80% probability of being flooded), versus MOHID with only a total of 230 features. The areas with the most notable differences are located south of Flagpole Point, the area surrounding Kitti Hall, and Mangilaluk School marked by the buildings with classes ranging from 2 to 4, not visible in MOHID.

The results for the RCP8.5 scenario depicted in Figure 64 for the UAV DSM reveal a total of 381 buildings are affected by a 50-year return period storm surge according to MOHID while the bathtub model identifies total of 493, where 332 belong to hazard class 5, 78 with class 4, 52 with class 3 and 31 with class 2. In comparison with RCP4.5 there is an increase in matching where MOHID matches all the hazard class 5 buildings and 49 belonging to hazard class 4. The most notable differences, where the bathtub model identifies additional features compared to MOHID are located between Flagpole point and the sports field in the north sector of the study area, the area surrounding the school and Kitti Hall, and the western area marked with the black circle in Figure 64 A). It is important to note that the water level for this scenario also correspond to a 100-year return period storm over a RCP4.5 scenario for the year 2100.

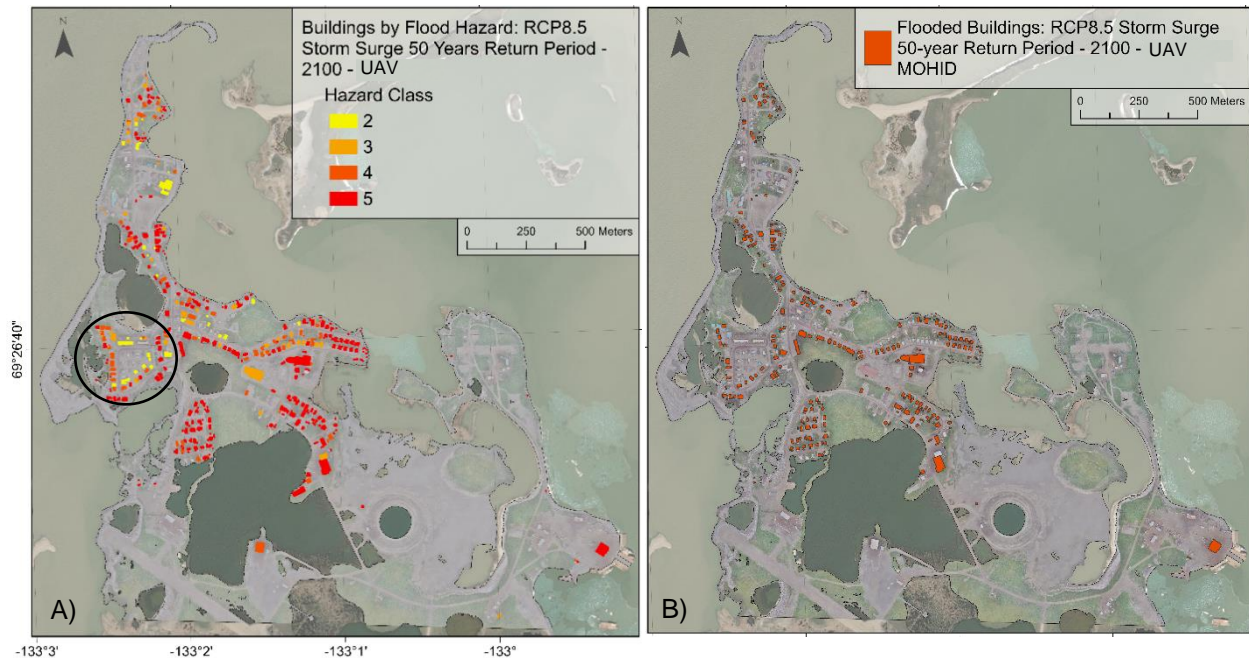


Figure 64 – Flooded buildings by model for the year 2100 and scenario RCP8.5 with a 50-year return period storm surge event on UAV DSM. A) Bathtub. B) MOHID.

Highlighting the transportation network becomes a useful way to visualize which road segments require most attention when it comes to prioritize road maintenance operations such as the ones performed frequently across Tuktoyaktuk during the warmer months, such as oil spraying the dirt road surfaces to decrease dust clouds by vehicles and promote water drainage, and deposition of new material to maintain the centre of the road higher and mitigate the effects of erosion caused by the traffic. The flood depth maps available in the Appendix (see Figures Figure A 12 and A Figure A 13) were used to assess the severity of flooding across the road network. In 2100, the concordance between models for RCP4.5 scenario with a 50-year return period storm surge over the UAV DSM shows that all the main roads in Tuktoyaktuk's transportation network become severely disrupted by flooding across the study area, isolating many different areas from road access. Some roads can still be traversed even if considered flooded depending on the water depth. The most dramatic depths, ranging from 1 to 2 m, in several points of Beaufort Road, Kitti Lane and Tuktu Road, Old Airport Road and Tingmivik Road, meaning that they become untraversable. For the scenario RCP8.5, the results show a significant increase in the affected road network for all classes when compared to RCP4.5 across all the study area. Such event can push the water further inland covering more than 200 m in the end of the airstrip facing northwest. The flood depth maps, generated from the bathtub model coupled with the UAV DSM, allowed the identification of new road segments that are now untraversable (Figure 65) when compared to the RCP4.5 scenario, such as the Beaufort Road segment and Centennial Road by the sports field, Ocean View Road and the only access to the DEW-Line, Quimavik Road.

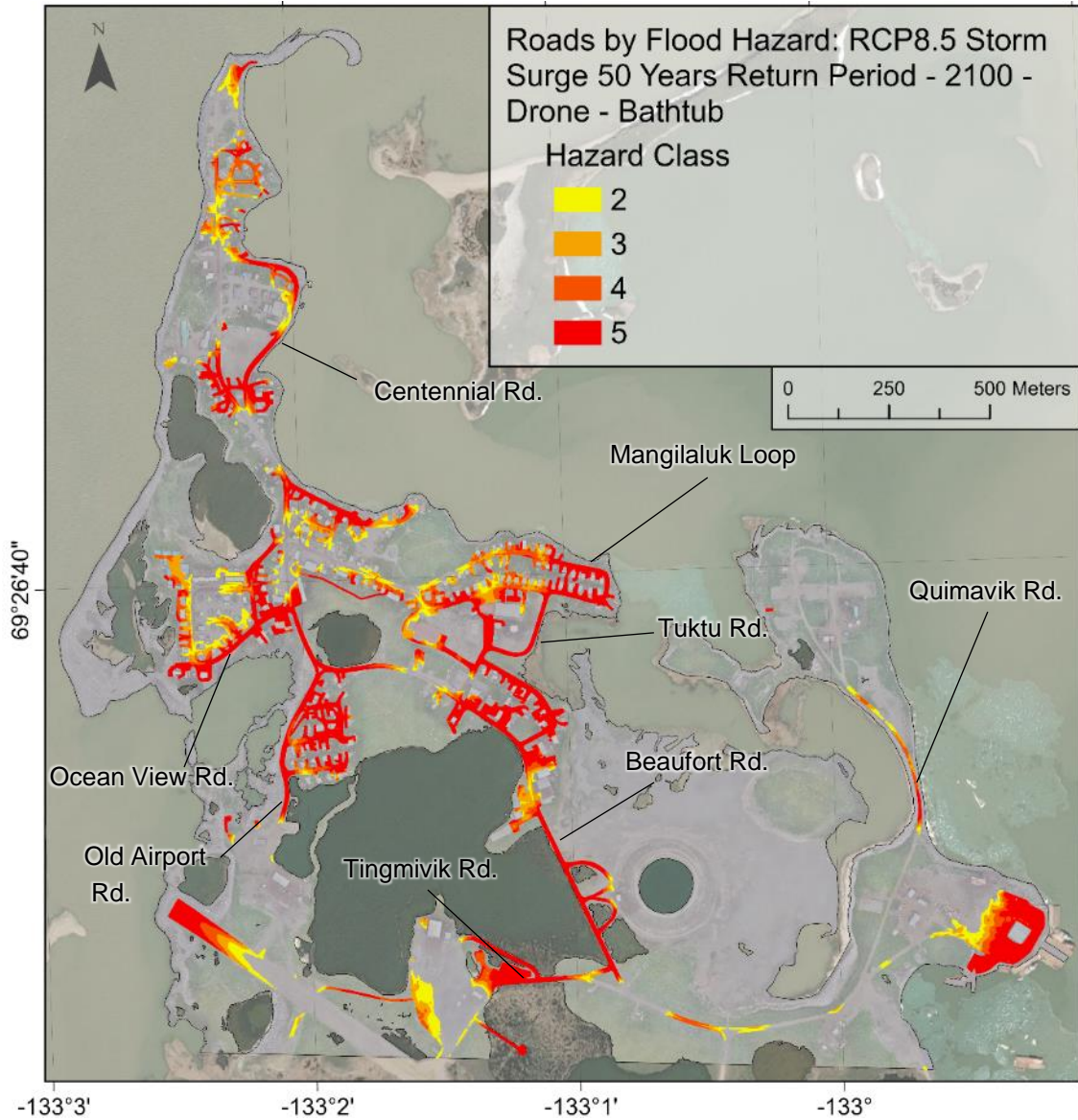


Figure 65 – Flooded roads obtained from bathtub model for the year of 2100 and RCP8.5 scenario for a 50-year return period storm surge event on UAV DSM.

5.6.2. 100-year Return Period Storm Surge Event

a) Synthesis of results

The inputted data and outputs regarding the 100-year return period storm surge for both bathtub and hydrodynamic models over the sea level rise scenarios RCP4.5, RCP8.5 and the MHAT are summarized in Tables Table 14, Table 15, Table 16 and Table 17.

Table 14 – UAV DSM bathtub model inputs used for the sea level rise and a 100-year return period storm surge by scenario.

Scenario	Years	Water Level Input (m CGVD2013)	σ Scenario	σ Chart Datum to CGVD2013	σ Tide	σ Storm Surge	σ Total
RCP 4.5	2020	2.41	0.07	0.15	0.02	0.44	0.48
	2060	2.64					
	2100	2.89					
RCP 8.5	2060	2.68	0.14	0.15	0.02	0.44	0.48
	2100	3.09					

Table 15 – UAV DSM hydrodynamic model inputs used for the sea level rise and a 100-year return period storm surge by scenario.

Flood Scenario	Year	Mean Highest Astronomical Tide (m above Chart Datum)	Sea Level Rise (m)	Storm Surge Water Level (m)	Water Level (m above Chart Datum)	Water Level Input (m - CGVD2013)	Model Output (m - CGVD2013)	Δ (m)
RCP 4.5	2020	0.92	0.00	2.1	3.02	2.41	2.41	-0.001
	2060		0.23		3.25	2.64	2.67	-0.031
	2100		0.49		3.50	2.89	2.88	0.014
RCP 8.5	2060	0.92	0.27	2.1	3.29	2.68	2.67	0.011
	2100		0.69		3.70	3.09	3.08	0.013

Table 16 – LiDAR DEM bathtub model inputs and outputs used for the sea level rise and a 100-year return period storm surge by scenario.

Scenario	Years	Water Level Input (m CGVD2013)	σ Scenario	σ Chart Datum to CGVD2013	σ Tide	σ Storm Surge	σ Total
RCP 4.5	2020	2.41	0	0.15	0.02	0.44	0.53
	2060	2.64					
	2100	2.89					
RCP 8.5	2060	2.68	0.14	0.15	0.02	0.44	0.53
	2100	3.09					

Table 17 – LiDAR DEM hydrodynamic model inputs and outputs used for the sea level rise and a 100-year return period storm surge by scenario.

Flood Scenario	Year	Mean Highest Astronomical Tide (m above Chart Datum)	Sea Level Rise (m)	Storm Surge Water Level (m)	Water Level (m above Chart Datum)	Water Level Input (m - CGVD2013)	Model Output (m - CGVD2013)	Δ (m)
RCP 4.5	2020	0.92	0.00	2.1	3.02	2.41	2.41	-0.001
	2060		0.23		3.25	2.64	2.63	0.003
	2100		0.49		3.50	2.89	2.89	-0.001
RCP 8.5	2060	0.92	0.27	2.1	3.29	2.68	2.67	0.006
	2100		0.69		3.70	3.09	3.08	0.012

b) Flood mapping

The computed total area flooded in m² for all the simulations regarding the 100-year return period storm surge and follows the same trend identified for the 50-year return period with LiDAR data returning larger flooded extents than the UAV and the bathtub model flooding more areas than MOHID. The year 2020 is not considered a RCP scenario, since it represents the current sea level conditions. The results show that

a 100-year return period storm, equivalent to 2.1 m above CD added to the MHAT, inundates 57.1% (UAV) and 65.8% (LiDAR) of the study area by using the bathtub model and 47.5% (UAV) and 52.3% (LiDAR) by MOHID. In 2060 all the percentages increase from 1 to 3% with the higher values corresponding to RCP8.5 scenario for the LiDAR simulations. For the year 2100, the bathtub model returns 80.7% (UAV) and 90.1% (LiDAR), while MOHID water surface covers 60 and 65% for the UAV and LiDAR, respectively. Figure 66 depicts the differences between the outputs of the bathtub model for the 100-year return period storm surge event, coupled to the sea level rise projections for the year 2100 according to scenario RCP8.5. The results align with the previous storm surge scenarios analysed for the 50-year return period, where the difference in the areas calculated for the two elevation datasets reside in building footprints being accounted for in the LiDAR DEM and few distinct patches of shrub-vegetated land in the southern and south-eastern sectors of the study area where the difference between UAV and LiDAR is higher. The areas flooded only in the UAV DSM represent a very small fraction of the total area and they are located in Flagpole Point, reaching 10 m on average further inland compared to the LiDAR, and an even smaller extent by the DEW-Line.

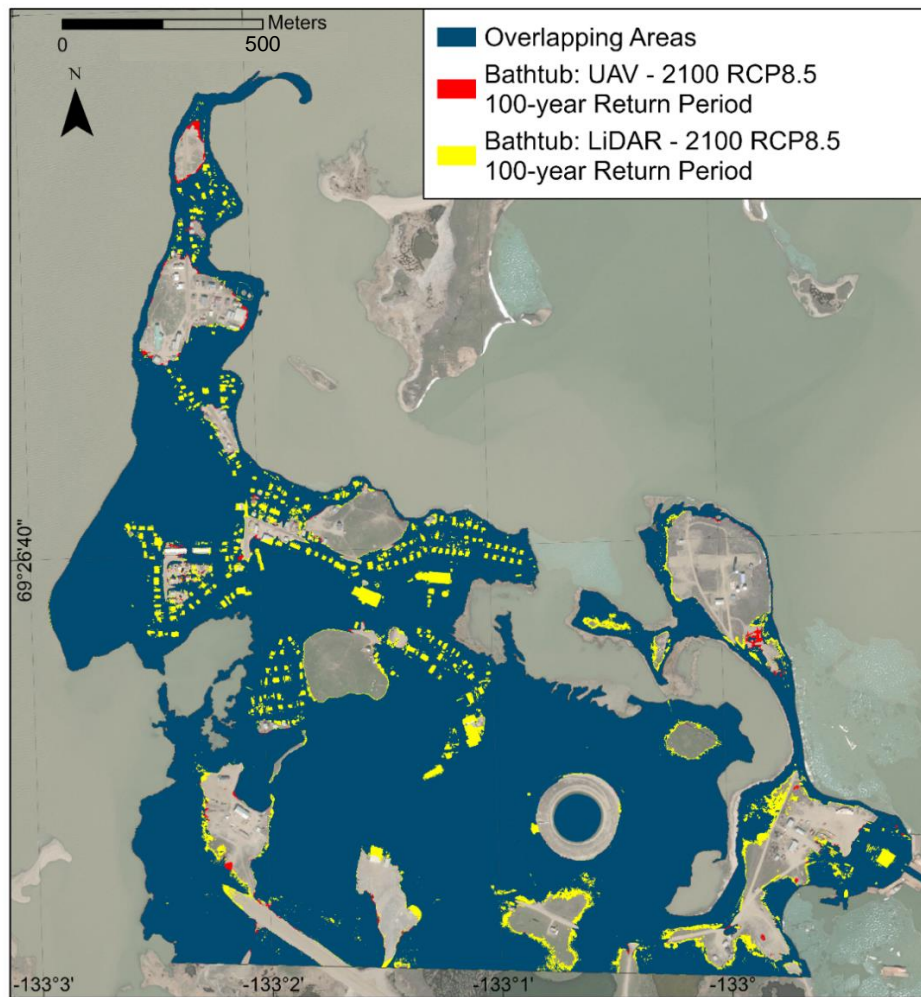


Figure 66 – Comparison between the UAV DSM and LiDAR DEM outputs from the bathtub model for the year 2100 and scenario RCP8.5 for a 100-year return period storm surge event. Hazard classes (2 to 5) are grouped as one single class.

The differences between the outputs of MOHID for the two elevation datasets are represented in Figure 67, As observed for the bathtub model, the LIDAR DEM larger extent is explained by the building footprints and patches of vegetated land located in the south of the study area and along the shore of Tareoknitok Lagoon, while the UAV DSM shows that most of the additional flooded areas are located in the north sector, where the difference between UAV and LiDAR displays the lowest values.

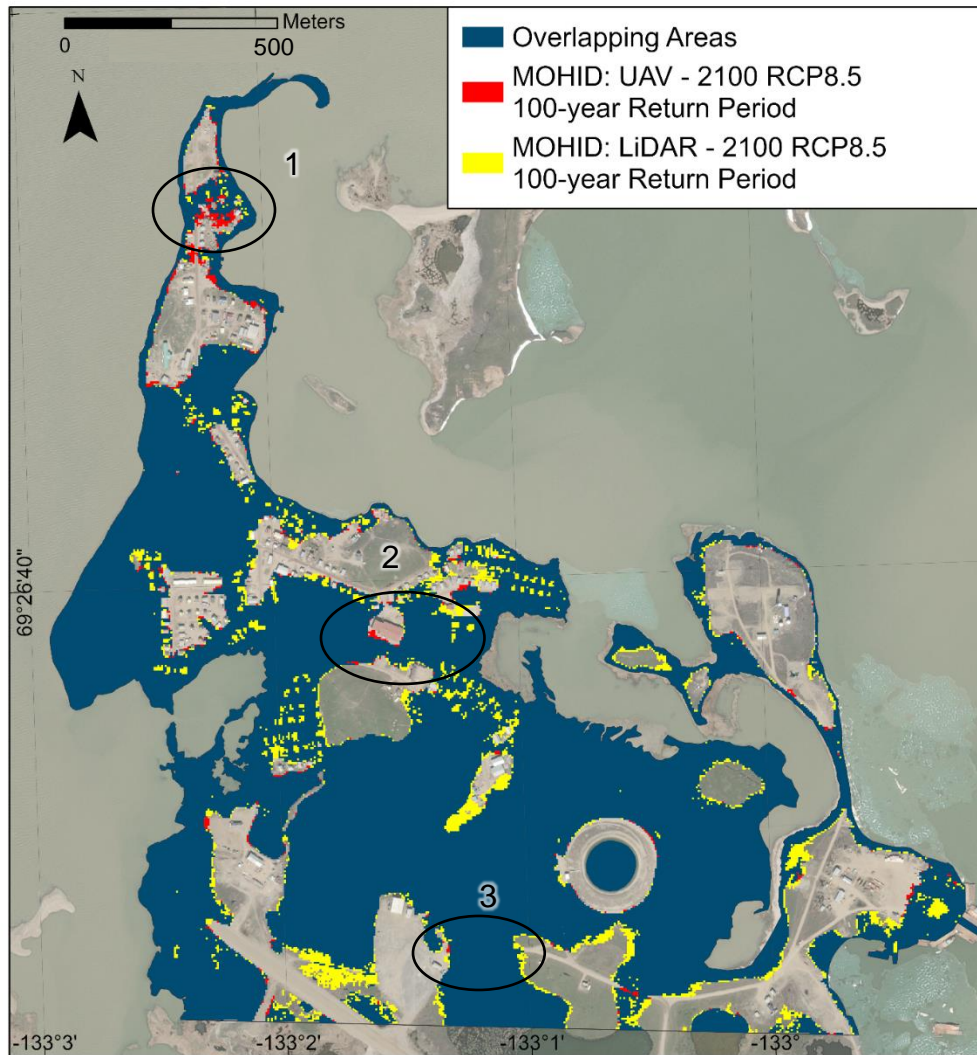


Figure 67 - Comparison between the UAV DSM and LiDAR DEM outputs from the hydrodynamic model for the year 2100 and scenario RCP8.5 for a 100-year return period storm surge event.

The 100-year return period storm surge event combined with the RCP4.5 scenario simulated in MOHID for the years 2060 and 2100 is available in the Appendix for the UAV DSM and LiDAR DEM (see Figure A 10 and Figure A 11). The darker blue areas represent what areas are flooded by a 100-year return period storm surge over the 2020 MHAT. The results reveal new breakage areas, when compared to a 50-year return period storm, in Flagpole point, by 2060 (1), south of Mangilaluk school (2), and in the access to the airstrip for the year 2100 (3). In Figure 68, the results represent the most pessimistic scenario simulated in this study where a 100-year return period storm surge is synchronized with the MHAT and the RCP8.5 SLR

projection. The differences between RCP4.5 and RCP8.5 are located in the centre of the study area, surrounding and between the pingos, and in the northern sector, where the flood extents are amplified in relation to scenario RCP4.5.

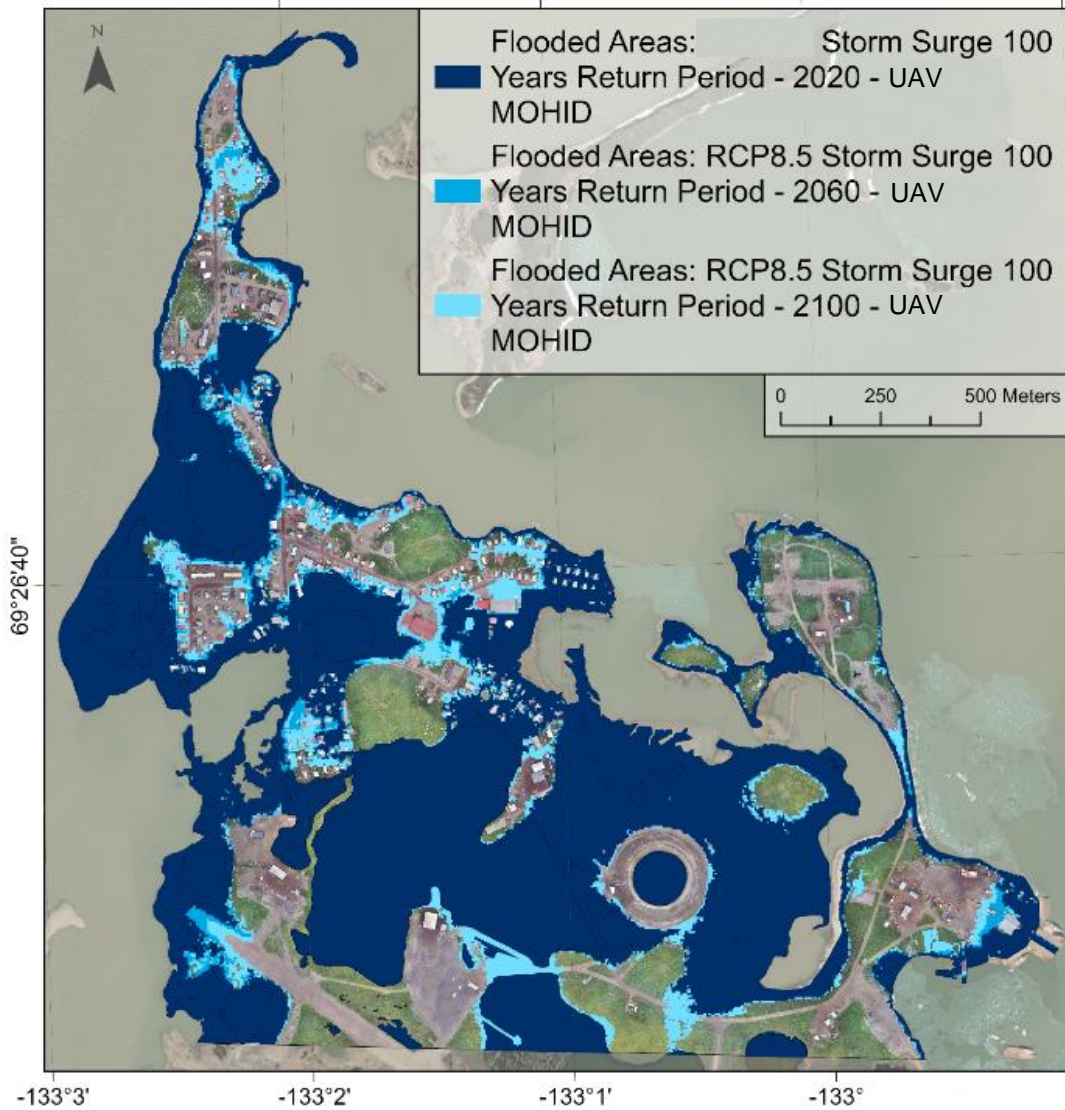


Figure 68 - MOHID water flooded areas by year for with a 100-year return period storm surge on UAV DSM and RCP8.5 scenario.

c) Exposure of infrastructure to flooding

The buildings and roads identified as affected by the simulated water surfaces for 100-year return period storm surge are represented in Figure 69 and Figure 70 for the bathtub model by 2100. The MOHID results are not shown since the bathtub provides a more conservative approach allowing the categorization of the affected buildings by the probability of flooding.

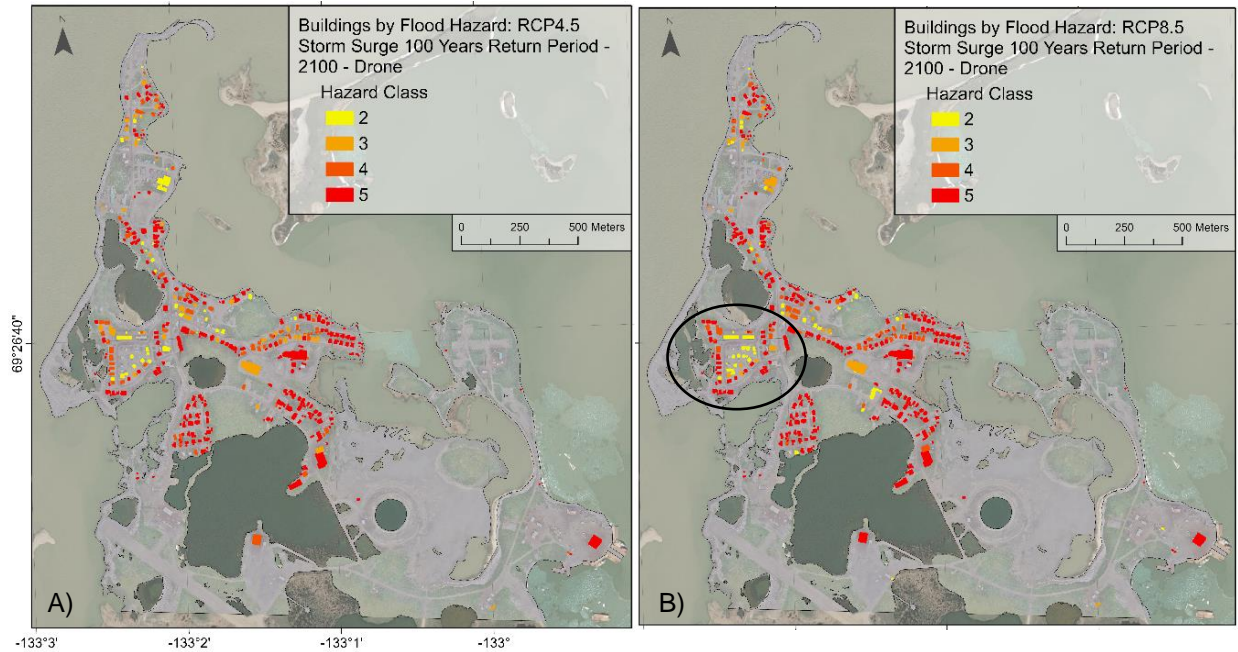


Figure 69 - Flooded buildings identified by the bathtub model for the year of 2100 by scenario for a 100-year return period storm surge event over the UAV DSM. A) RCP4.5. B) RCP8.5.

In Figure 69 there are 510 different features inside the flood extent for the scenario RCP4.5 and 544 for RCP8.5. While both scenarios are devastating to the local community, there are differences between the flood extents worth mention. The areas identified by scenario RCP8.5 that are not displayed in RCP4.5 are marked by the circle in the figure. Another difference is that most buildings that belong to classes 4 and 3 are now classified as 5 and 4 due to the increase in the sea level difference between scenarios. The road network analysis for the RCP8.5 scenario combined with a 100-year return period storm surge is depicted in Figure 70. There are no notable differences when comparing the extents of flooded roads to the 50-year return period scenario for the same year, except in the circled area marked in Figure 69 B), where the road is now marked as affected by flooding with hazard classes ranging from 3 to 2 and an overall transition from lower probability hazard classes to higher ones in RCP8.5.

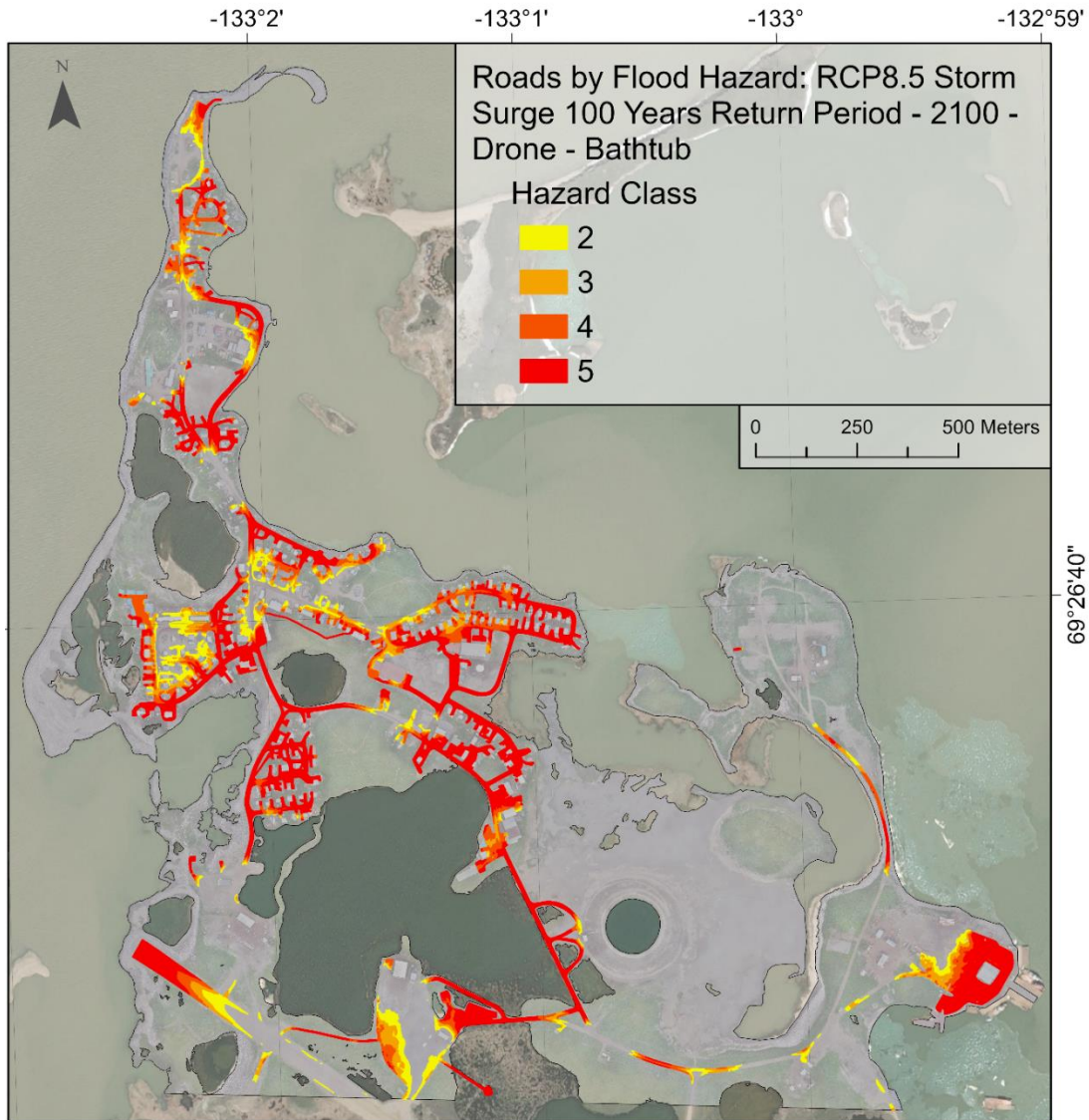


Figure 70 – Flooded roads identified by the bathtub model for the year of 2100 by scenario for a 100-year return period storm surge event over the UAV DSM.

The combination of sea level rise scenario RCP8.5 and a 100-year return period storm surge correspond to the most pessimistic simulation and represents the uppermost limit of the water surface which is crucial in infrastructure and territorial flood risk assessment from a precautionary and conservative perspective.

5.7. Presently Flood Exposed Infrastructure

In this chapter is presented an analysis and assessment of the built environment that is endangered by the flood events of 50 and 100-years return periods coupled with the 2020 MHAT of 0.92 m above CD. The analysis was done on both hydrodynamic and bathtub models, although, due to lower uncertainty of the elevation data and no sea level rise projections, the results are shown only for the bathtub model flood

maps. This model was chosen since it provides insight regarding flood probability instead of a rigid single water level flood map.

5.7.1. Transportation and Buildings

The road network and buildings affected by the 50 and 100-year return period storms based on the bathtub model coupled with the UAV data are represented in Figure 71 and Figure 72.

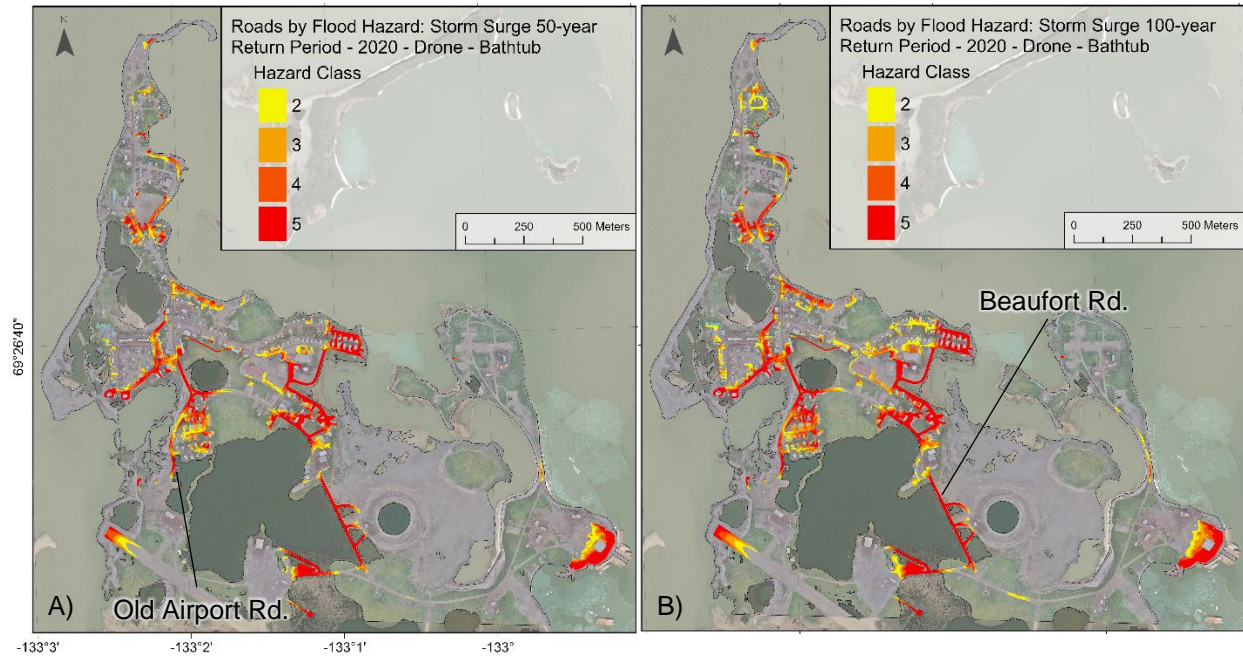


Figure 71 – Roads by flood hazard class obtained by the bathtub model over UAV DSM for two different storm surge events in 2020. A) 50-year return. B) 100-year return period.

As seen in Figure 71, the segment of Beaufort Road, west of the water reservoir is one of the two possible land connections to mainland, along with Old Airport Road. Both roads become flooded by the 50-year return period storm surge becoming highly susceptible to flooding. If both roads are not traversable, there is no other connection available to the north part of the hamlet, leaving it completely isolated from the mainland. Figure 72 represents the buildings that were identified as susceptible to flooding for the year of 2020. In case of relocation, buildings marked as class 5 should be considered as highest priority. Despite coastal erosion is not as intense in the eastern shore of Tuktoyaktuk and the strongest storm winds that generate the most dramatic wave run up heights blow from northwest, many of these buildings are still endangered in case of severe storm surge events as the ones included in the simulations.

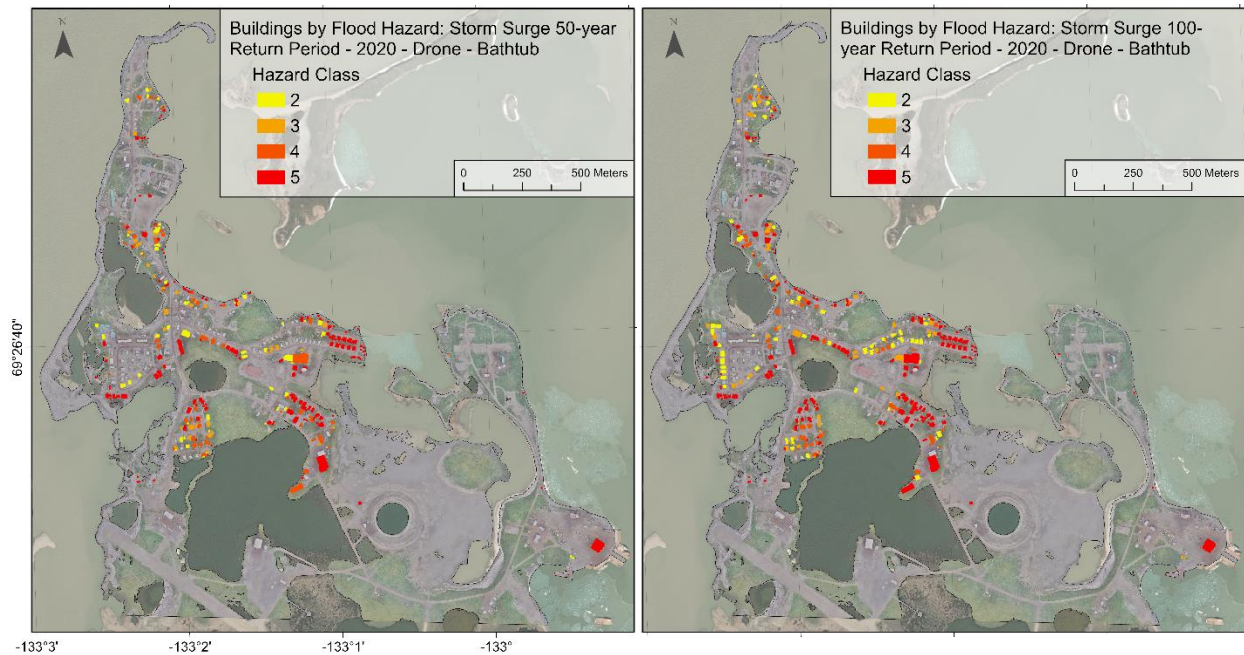


Figure 72 – Buildings by flood hazard class obtained by the bathtub model over UAV DSM for a 50-year (left) return period storm surge and 100-year (right) return period for 2020.

The results presented in this thesis may be used as an update to the current flood risk geodata available at the Northwest Territories ATLAS (Government of Northwest Territories, 2021) as seen in Figure 73. According to the description available online in the ATLAS User Manual, the “Floodway” layer represents the floodway to assist in flood damage reduction that shows all elevations below that designated under the Canada – Northwest Territories Agreement Respecting Flood Damage Reduction and Flood Risk Mapping in the mid-1980s, and “Flood Fringe” is defined as the area that where the elevation is 1.0 m or less higher than the flood water elevation. The output of the bathtub model for the UAV DSM identifies 423 flooded features: 199 hazard class 5, 70 class 4, 63 class 3 and 91 class 2, while the total of the features contained in both Floodway and Floodfringe are 264, where 33 belong in the latter. There is a clear overlap by buildings identified with higher probability classes (5 and 4) and both Flood Risk layers, but 159 features, from all hazard classes, are outside the boundaries. The buildings not included in the ATLAS layers are located in the north sector, by Flagpole Point, north of Kitti Hall and Mangilaluk School and two small clusters south of the sports field and by the northwest shore of Tareoknitok Lagoon,

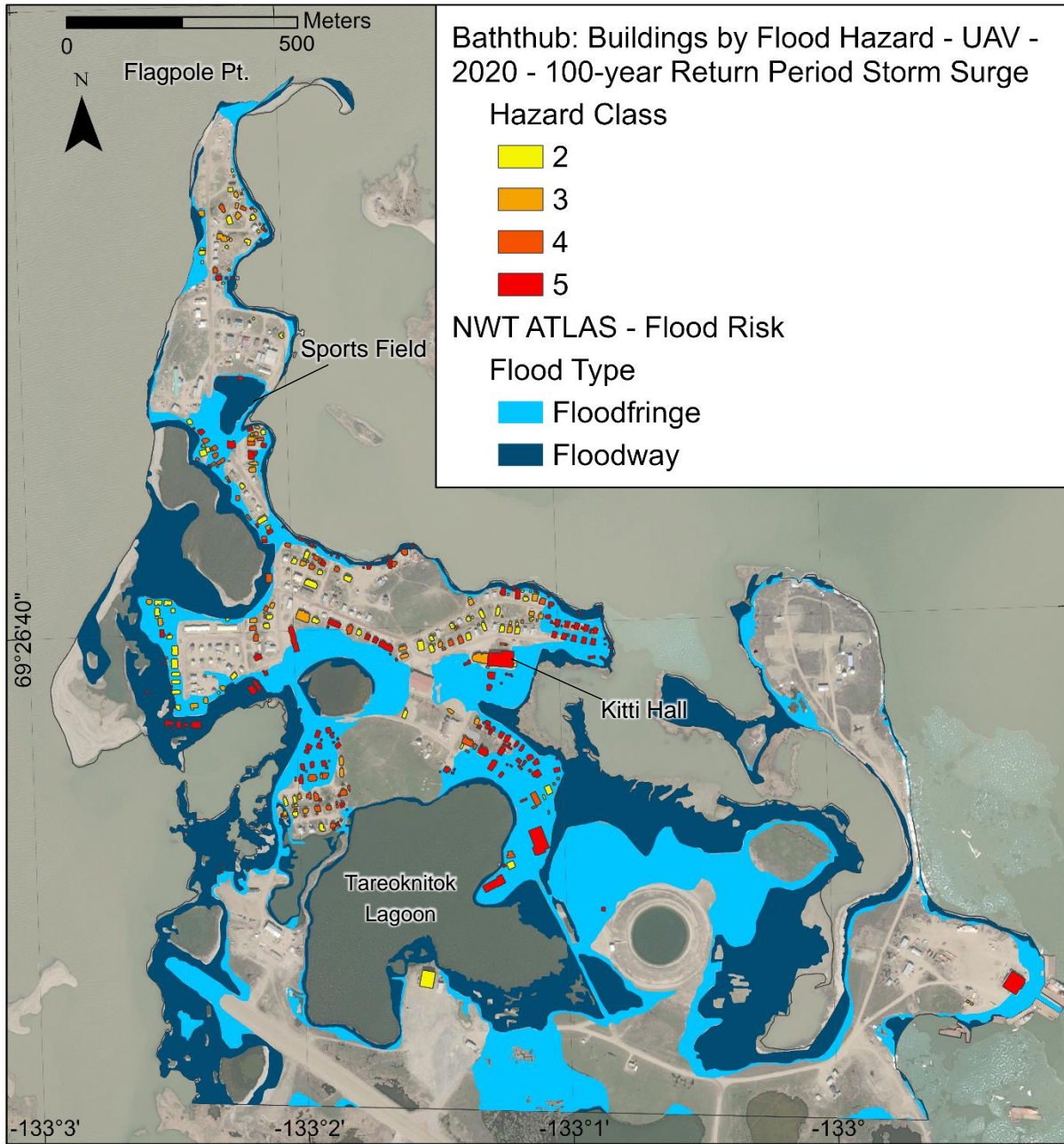


Figure 73 – Detail of the overlay of ATLAS’ (Government of Northwest Territories, 2021) “Flood_Risk” layer and the year 2020 bathtub model result for a 100-year return period storm surge as affected buildings by hazard class.

6. Conclusions and Outlook

The results obtained from this study show that it was possible to model and map with great accuracy the water surface changes in different scenarios in the Hamlet of Tuktoyaktuk. The models allowed the quantification and identification of flooded areas and to categorize the built environment by its vulnerability to sea level rise and storm surge events.

The main goal of this thesis focused in developing a methodology that permitted the identification, with precision, of areas vulnerable to coastal flooding including two different sea level rise scenarios, for the years of 2060 and 2100, and extreme events with two different return periods. It was possible to conclude that the quality and availability of the data played a major role in flood mapping and that there is a significant water level data gap from 1982 to 1991 and 1992 to 2003 that can impact the results obtained by tidal harmonic analysis and extreme event analysis of storm surge levels. Regarding elevation data, using a UAV-derived well-georeferenced surface model with higher vertical and horizontal accuracy and spatial resolution, reduced significantly the overall uncertainty included in the bathtub model and, therefore, reduced over-estimation of flooded areas compared to LiDAR.

The lower uncertainty of the UAV data drastically improved the water-surface modelling. With the tightening of areas with hazard classes of lower probabilities, the model showed precise overlaps of probability classes between 99.9% and 40% (classes 5 to 3) with the water surface captured by the UAV footage, as well as by time-lapse cameras, used as ground truthing data. This reinforces the advantage of UAV over the available 2004 LiDAR data. Having an ultra-high-resolution mosaic of the study area revealed a major advantage to derive the local difference between vertical datums, to validate results by replicating the conditions registered at the time of the flight and identify details to a centimetric precision in 2D and 3D.

Regarding the hydrodynamic modelling, the resampling from 0.1 x 0.1 m to 5 x 5 m cell size significantly reduced the vertical accuracy of the UAV model due to the interpolation algorithm. This transformation resulted in similar outputs for both LiDAR and UAV elevation datasets by diluting the differences. The culvert system had to be manually edited and exaggerated to be represented in 5 x 5 m cells after the smoothing effect of the algorithm. For a simplistic modelling of the water surface, the results show that complexity of the hydrodynamic model does not translate directly in a more accurate flood mapping. By maintaining the original cell size, the bathtub model does not lose vertical data and it offers the advantage of probabilistic mapping allowing the quantification of the flooded area and identification of the susceptibility by different hazard classes of specific locations. These drawbacks were also identified by Seenath et al. (2015) when comparing two different hydrodynamic models with a GIS-based bathtub approach. While the hydrodynamic model predicts an 8.9% submersion of the total study area by 2060 with a RCP4.5 SLR scenario and 14.4% in 2100, for the same epoch, the bathtub model returns 22.4% and 29.2% respectively. For RCP8.5, MOHID returns 9.3% in 2060 and 16.1% as the bathtub model calculates 23.5% and 32.2%

respectively. The percentage of the study area affected by an extreme flood event of 100-year return period coinciding with the MHAT can reach up to 80.7% for RCP8.5 and the year of 2100 using the UAV elevation. For 2020, in case of a flood event with a 50-year return period combined with the highest tide, represents a complete isolation of the hamlet from land, a situation that has occurred several times in the past. The modelling approach used in this study is based on the present physical conditions and on keeping them constant. While this might be a satisfactory assumption for some sectors of the study area, it is not the case for the western and northern coastline due to high rates of coastal erosion and sediment transport and deposition patterns. The changes in landforms and their geometry affect coastal hydraulics that translate in changes in tidal elevations. These variables are not included in bathtub approaches but can be minimized with continuous surveying and hydrodynamic modelling. The cartography in this thesis was created to be used as a tool for coastal planning adaptation for the community of Tuktoyaktuk and provide an updated, more accurate and pre-emptive version of the flood maps currently available on Northwest Territories ATLAS (Government of Northwest Territories, 2021).

There are many aspects of flood modelling, not necessarily related with the quality of the elevation data, that can be continuously implemented and developed to improve the methodology used in this study. Including wave set up and wave run up will lead to an overall increase in floodable areas for storm surge scenarios. Wave models such as SWAN (Simulating Waves Nearshore) can be coupled with hydrodynamic models to address this limitation if accurate wave and wind data is provided. The current available wave and wind data for Tuktoyaktuk reveals significant gaps where the most recent data is hourly data from September 2014 to February 2015. From the hydrodynamic analysis and in-situ observations, the shore exposed to the predominantly and stronger storm winds and waves from north-west, act as a physical barrier to wave action. Deploying a buoy to record wave data during the open water season can lead to major improvements regarding the inclusion of wave modelling in future flood mapping and coastal erosion dynamics. For the bathtub model, the incorporation of uncertainty of the elevation data is achieved by using a single value of RMSE that represents the global error of the dataset. However, it is known that errors show spatial variability, meaning that it is possible to break the study area in smaller sectors, of similar values of RMSE to better represent the uncertainty and leading to a more accurate spatial representation of uncertainty for a given sector.

The soaring coastal erosion rates in Tuktoyaktuk create an intricate aspect for flood modelling by sculpting the coast constantly. Incorporating these changes would only be possible by updating the elevation data more frequently, at least, along the most affected coastline sectors. The morphological changes caused by coastal erosion can lead to the exposure of areas that are currently identified as not affected by coastal flooding.

7. References

- Andrachuck, M., Smit, B. (2002). Community-based vulnerability assessment of Tuktoyaktuk, NWT, Canada to environmental and socio-economic changes. *Regional Environmental Change*, 12(4), 867-885, <https://doi.org/10.1007/s10113-012-0299-0>.
- Annis, A., Nardi, F., Petroselli, A., Apollonio, C., Arcangeletti, E., Tauro, F., Belli, C., Bianconi, R., Grimaldi, S. (2020). UAV-DEMs for small-scale flood hazard mapping. *Water*. 12(1717), <https://doi.org/10.3390/w12061717>
- Antunes, C., Rocha, C., & Catita, C. (2019). Coastal Flood Assessment due to Sea Level Rise and Extreme Storm Events: A Case Study of the Atlantic Coast of Portugal's Mainland. *Geosciences*, 9(5), 239. MDPI AG.
- Arakawa, A. (1966). Computational design for long-term numerical integration of the equations of fluid motion: Two-dimensional incompressible flow. Part 1. *Journal of Computational Physics*, 1(122), 119–143.
- Atkinson, D. E. (2005): Observed storminess patterns and trends in the circum-Arctic coastal regime. *Geo-Mar. Lett.*, 25, 98–109.
- Aveco Infrastructure Consultants. July 1986. Tuktoyaktuk Shore Erosion Protection.
- Backes, D.; Schumann, G.; Teferele, F.N.; Boehm, J. (2019). Towards a High-Resolution Drone-Based 3D Mapping Dataset to Optimise Flood Hazard Modelling. *Int. Arch. Photogramm. Remote Sens. Spat. Inf. Sci.—ISPRS Arch.*, 42, 181–187.
- Bales, J.D., Wagner, C.R., Tighe, K.C., Terziotti, S. (2007). LiDAR-derived flood-inundation maps for real-time flood-mapping applications, Tar River Basin, North Carolina. Geological Survey (US): Reston, VA, USA.
- Baltsavias EP (1999) Airborne laser scanning: basic relations and formulas. *ISPRS J Photogrammetry Remote Sens* 54(2–3):199–214
- Barber, D. G., and J. M. Hanesiak (2004): Meteorological forcing of sea ice concentrations in the southern Beaufort Sea over the period 1979 to 2000. *J. Geophys. Res.*, 109, C06014, doi:10. 1029/2003JC002027.
- Barnhart, K.R., Anderson, R.S., Overeem, I., Wobus, C., Clow, G.D., Urban, F.E., (2014). Modeling erosion of ice-rich permafrost bluffs along the Alaskan Beaufort Sea coast. *J. Geophys. Res. Earth Surf.* 119, 1155–1179. <http://dx.doi.org/10.1002/2013JF002845>.

Brown, J., Jorgenson, M.T., Smith, O. P. and Lee, W. (2003) Long-term rates of erosion and carbon input, Elson Lagoon, Barrow, Alaska 2003 ICOP2003 Permafrost: Proc. 8th Int. Conf. on Permafrost ed M Phillips et al. (Netherlands: A.A. Balkema Publishers) pp 101–6

Brunner, R. D., A. H. Lynch, J. C. Pardikes, E. N. Cassano, L. R. Lestak, and J. M. Vogel (2004). An Arctic disaster and its policy implications. *Arctic* 57 (4):336–46. doi: 10.14430/arctic512.

Burn CR, Kokelj SV. (2009). The environment and permafrost of the Mackenzie Delta area. *Permafrost and Periglacial Processes* 20: 83 –105. <https://doi.org/10.1002/ppp.655>.

Burn CR. (2002). Tundra lakes and permafrost, Richards Island, western Arctic coast, Canada. *Canadian Journal of Earth Sciences* 39: 1281–1298. <https://doi.org/10.1139/e02-035>

Burn, C.R., Zhang, Y. (2010). Sensitivity of active-layer development to winter conditions north of tree line, Mackenzie Delta area, western Arctic coast. In *Proceedings 6th Canadian Permafrost Conference, 12–16 September 2010, Calgary, AB, Paper 194*. Canadian Geotechnical Society; 1458–1465.

Casas, A.; Benito, G.; Thorndycraft, V.R.; Rico, M. (2006). The topographic data source of digital terrain models as a key element in the accuracy of hydraulic flood modelling. *Earth Surf. Process. Landf.*, 31, 444–456.

Church, J. A., P. Clark, A. Cazenave, J. Gregory, S. Jevrejeva, A. Levermann, M. Merrifield, G. Milne, R.S.Nerem, P. Nunn, A. Payne, W. Pfeffer, D. Stammer, and A. Unnikrishnan (2013), *Sea level change*, in *Climate Change 2013: The Physical Science Basis*, edited by T. F. Stocker, D. Qin, G.-K. Plattner, M. Tignor, S. Allen, J. Boschung, A. Nauels, Y. Xia, V. Bex, and P. Midgley, Cambridge University Press, Cambridge, UK and New York, NY. USA. Regional sea level data from IPCC AR5 distributed in netCDF format by the Integrated Climate Data Center/ICDC, CEN, University of Hamburg, Hamburg, Germany.

Comiso, J. C. (2003): Warming trends in the Arctic from clear sky satellite observations. *J. Climate*, 16, 3498–3510.

Community of Tuktoyaktuk, Wildlife Management Advisory Council (N.W.T.), Tuktoyaktuk Conservation Plan Working Group. Joint Secretariat (2000), *Tuktoyaktuk Community Conservation Plan: A plan for the conservation and management of renewable resources and lands within the Inuvialuit settlement region in the vicinity of Tuktoyaktuk, Northwest Territories*.

Couture, R., Robinson, S., Burgess, M., & Solomon, S. (2002). *Climate Change, Permafrost, and Infrastructure Community: A Compilation of Background Material from a Pilot Study of Tuktoyaktuk, Northwest Territories*, Geological Survey of Canada, Open File 3867, 83 p.

Craymer, M.R., J. Henton, M. Piraszewski, E. Lapelle, (2011). An updated GPS velocity field for Canada. *Eos Transactions, AGU*, 92(51), Fall Meeting Supplement, Abstract G21A-0793, 2011 (available at ftp://geod.nrcan.gc.ca/pub/GSD/craymer/pubs/cgsbn_agu2011fall_poster.pdf). Dallimore, S.R., Wolfe,

S.A., Solomon, S.M., (1996). Influence of ground ice and permafrost on coastal evolution, Richards Island, Beaufort Sea coast, NWT. *Can. J. Earth Sci.* 33, 664–675.

Danard, M., A. Munro, and T. Murty (2003): Storm surge hazard in Canada. *Nat. Hazards*, 28, 407–431.

Daniel Codiga (2021). UTide Unified Tidal Analysis and Prediction Functions (<https://www.mathworks.com/matlabcentral/fileexchange/46523-utide-unified-tidal-analysis-and-prediction-functions>), MATLAB Central File Exchange. Retrieved August 27, 2021.

De Smith, M. J., Goodchild, M. F. and Longley, P. A. (2007). *Geospatial analysis: a comprehensive guide to principles, techniques and software tools*. Leicester, Matador.

Department of Public Works (1971). Investigation of storm, September 13-16, 1970 - Mackenzie Delta region, Beaufort Sea. Unpublished Technical Report by Public Works of Canada, Ottawa. 20 p. Available at the Department of Public Works, Ottawa.

Drobot, S. D., and J. A. Maslanik (2003): Interannual variability in summer Beaufort Sea ice conditions: Relationship to winter and summer surface and atmospheric variability. *J. Geophys. Res.*, 108, 3233, doi:10.1029/2002JC001537.

Environment Canada (2021). 1981 to 2010 Canadian Climate Normals station data. https://climate.weather.gc.ca/climate_normals/results_1981_2010_e.html?searchType=stnName&txtStationName=tuktoyaktuk&searchMethod=contains&txtCentralLatMin=0&txtCentralLatSec=0&txtCentralLongMin=0&txtCentralLongSec=0&stnID=1700&dispBack=1

Favalli, M., Fornaciai, A., and Pareschi, M. T. (2009). LIDAR strip adjustment: Application to volcanic areas, *Geomorphology*, 111, 123–135, <https://doi.org/10.1016/j.geomorph.2009.04.010>

FEMA. (2003). *Guidance for Flood Risk Analysis and Mapping*. Department of Homeland Security.

Fissel, D.B. and Birch, J.R., (1984). Sediment transport in the Canadian Beaufort Sea. *Arctic Sci. Ltd.*, Sidney, B.C., Tech. Rep. for Geol. Surv. Can. 165 pp. (Unpublished).

Fofonoff, N. P., and Millard Jr, R. C. (1983). Algorithms for the computation of fundamental properties of seawater. *UNESCO Technical Papers in Marine Sciences*; 44.

Franz, G., Delpy, T. M., Brito, D., Neves, R., Leitão, P., and Pinto, L. (2017). “Modelling of sediment transport and morphological evolution under the combined action of waves and currents.” *Ocean Science*, 13(5), 673–690.

Fraser RH, Lantz TC, Olthof I, Kokelj SV, Sims RA. (2014). Warming-induced shrub expansion and lichen decline in the Western Canadian Arctic. *Ecosystems* 17:1151–1168. <https://doi.org/10.1007/s10021-014-9783-3>

Fritz, M., Wetterich, S., Meyer, H., Schirrmeister, L., Lantuit, H., Pollard, W.H., 2011. Origin and characteristics of massive ground ice on Herschel Island (western Canadian Arctic) as revealed by stable water isotope and hydrochemical signatures. *Permafrost Periglacial Processes*, 22:26–38. <http://dx.doi.org/10.1002/ppp.714>.

Government of Northwest Territories (2021). Administration of the Territorial Land Acts System – ATLAS Map Viewer. https://www.maps.geomatics.gov.nt.ca/HTML5Viewer_Prod/index.html?viewer=ATLAS

Günther, F., Overduin, P.P., Sandakov, A.V., Grosse G. and Grigoriev, M.N. (2013) Short- and long-term thermo-erosion of ice-rich permafrost coasts in the Laptev Sea region *Biogeosciences* 2013 4297–318. doi: 10.5194/bg-10-4297-2013.

Harper, J.R., 1990. Morphology of the Canadian Beaufort Sea Coast. In: P.R. Hill (Editor), *The Beaufort Sea Coastal Zone*. *Mar. Geol.*, 91 (Spec. Sect.): 75-91

Harper, J.R., Henry R.F., Stewart, G.G. (1988). Maximum storm surge elevations in the Tuktoyaktuk region of the Canadian Beaufort Sea. *Arctic*, 41(1), 48-52.

Hashemi-Beni, L.; Jones, J.; Thompson, G.; Johnson, C.; Gebrehiwot, A. (2018) Challenges and Opportunities for UAV-Based Digital Elevation Model Generation for Flood-Risk Management: A Case of Princeville, North Carolina. *Sensors*, 18, 3843.

Henry, R.F. (1975). Storm surges, Beaufort Sea project technical report no. 19. Sidney, B.C.: Institute of Ocean Sciences, 41p.

Henry, R.F., & Heaps, N.S. (1976). Storm surges in the southern Beaufort Sea. *Journal of the Fisheries Research Board of Canada*, 33, 2362-2376.

Hinkel, J., D. P. van Vuuren, R. J. Nicholls, and R. J. T. Klein. 2013. The effects of adaptation and mitigation on coastal flood impacts during the 21st century. An application of the DIVA and IMAGE models. *Climatic Change* 117 (4):783–94. doi: 10.1007/s10584-012-0564-8.

Hudak, D., and J. Young (2002): Storm climatology of the southern Beaufort Sea. *Atmos.–Ocean*, 40, 145–158.

Hume, J., and M. Schalk. 1967. Shoreline processes near Barrow, Alaska: A comparison of the normal and the catastrophic. *Arctic* 20 (2):86–103. doi: 10.14430/arctic3285.

Hynes, S., Solomon, S.M., Whalen, D. (2014). GIS compilation of coastline variability spanning 60 years in the Mackenzie Delta and Tuktoyaktuk in the Beaufort Sea. Geological Survey of Canada, Open File 7685, 1 .zip file. doi:10.4095/295579

IPCC, (2019): IPCC Special Report on the Ocean and Cryosphere in a Changing Climate [H.-O. Pörtner, D.C. Roberts, V. Masson-Delmotte, P. Zhai, M. Tignor, E. Poloczanska, K. Mintenbeck, A. Alegría, M. Nicolai, A. Okem, J. Petzold, B. Rama, N.M. Weyer (eds.)]. In press.

IPCC, (2021): Climate Change 2021: The Physical Science Basis. Contribution of Working Group I to the Sixth Assessment Report of the Intergovernmental Panel on Climate Change [Masson-Delmotte, V., P. Zhai, A. Pirani, S. L. Connors, C. Péan, S. Berger, N. Caud, Y. Chen, L. Goldfarb, M. I. Gomis, M. Huang, K. Leitzell, E. Lonnoy, J. B. R. Matthews, T. K. Maycock, T. Waterfield, O. Yelekçi, R. Yu and B. Zhou (eds.)]. Cambridge University Press. In Press.

James, M. R., Chandler, J. H., Eltner, A., Fraser, C., Miller, P. E., Mills, J. P., Noble, T., Robson, S., and Lane, S. N. (2019). Guidelines on the use of structure-from-motion photogrammetry in geomorphic research, *Earth Surf. Proc. Land.*, 44, 2081–2084, <https://doi.org/10.1002/esp.4637>

James, T.S., Henton, J.A., Leonard, L.J., Darlington, A., Forbes, D.L., and Craymer, M., (2014). Relative sea-level projections in Canada and the adjacent mainland United States; Geological Survey of Canada, Open File 7737, 72 p. doi:10.4095/295574

Johannessen OM, Bengtsson L, Miles MW, Kuzmina SI, Semenov VA, Alekseev GV, Nagurnyi AP, Zakharov VF, Bobylev L, Pettersson LH, Hasselmann K, Cattle HP (2002) Arctic climate change—observed and modelled temperature and sea ice variability. Nansen Environmental and Remote Sensing Centre Tech Rep 218:22

Johnson, K., Solomon, S., Berry, D. and Graham, P. (2003). Erosion progression and adaptation strategy in a northern coastal community, *Permafrost. M. Philips, S. M. Springman and L. U. Arenson*), 489-494, 8th International Conference on Permafrost, Zurich, Switzerland.

Jones, B. M., C. D. Arp, M. T. Jorgenson, K. M. Hinkel, J. A. Schmutz, and P. L. Flint (2009): Increase in the rate and uniformity of coastline erosion in Arctic Alaska. *Geophys. Res. Lett.*, 36, L03503, doi:10.1029/2008GL036205.

Jones, B.M., Arp, C.D., Jorgenson, M. T., Hinkel, K.M., Schmutz, J. A. and Flint, PL (2009b). Increase in the rate and uniformity of coastline erosion in Arctic Alaska *Geophys. Res. Lett.* 36 L03503

Jorgenson, M. T., Y. L. Shur, and E. R. Pullman (2006): Abrupt increase in permafrost degradation in Arctic Alaska. *Geophys. Res. Lett.*, 33, L02503, doi:10.1029/2005GL024960.

Judge AS, Pelletier BR, Norquay I. (1987). Permafrost base and distribution of gas hydrates. In *Marine science atlas of the Beaufort Sea: geology and geophysics*. Pelletier BR (ed.). Geological Survey of Canada, Miscellaneous Report 40, Map 39

Khan, H.; Vasilescu, L.G.; Khan, A. (2008). Disaster management cycle—A theoretical approach. *J. Manag. Mark.* 6, 43–50.

- Kokelj SV, Lantz TC, Wolfe SA, Kanigan JC, Morse PD, Coutts R, Molina-Giraldo N, Burn CR. (2014). Distribution and activity of ice wedges across the forest–tundra transition, western Arctic Canada. *Journal of Geophysical Research: Earth Surface* 119:2032–2047. <https://doi.org/10.1002/2014JF003085>
- Langhammer, J.; Bernsteinová, J.; Mirijovský, J. (2017) Building a High-Precision 2D Hydrodynamic Flood Model Using UAV Photogrammetry and Sensor Network Monitoring. *Water*, 9, 861.
- Lantuit, H., Overduin, P.P. et al. (2012). The Arctic Coastal Dynamics database. A new classification scheme and statistics on arctic permafrost coastlines. *Estuaries and Coasts*, 35, 383–400.
- Lantz TC, Marsh P, Kokelj SV. (2013). Recent shrub proliferation in the Mackenzie Delta uplands and microclimatic implications. *Ecosystems* 16: 47 –59. <https://doi.org/10.1007/s10021-012-9595-2>
- Leitão, P. (2002). Integração de Escalas e de Processos na Modelação do Ambiente Marinho. Instituto Superior Técnico.
- Li, J.; Wong, D.W.S. (2010). Effects of DEM sources on hydrologic applications. *Comput. Environ. Urban Syst.*,34, 251–261.
- Li, Z., Q. Zhu, and C. Gold. (2005). *Digital Terrain Modelling, Principles and Methodology*. Boca Raton, FL: CRC Press.
- Lintern, D. G., R. W. Macdonald, S. M. Solomon, and H. Jakes (2011), Beaufort Sea storm and resuspension modeling, *J. Mar. Syst.*, doi:10.1016/j.jmarsys.2011.11.015
- Mackay JR. (1992). Lake stability in an ice-rich permafrost environment: examples from the western Arctic coast. In *Aquatic Ecosystems in Semi-Arid Regions: Implications for Resource Management*, Robarts RD, Bothwell ML (eds). NHRI Symposium Series 7. Environment Canada: Saskatoon; 1–26.
- Manson GK, Solomon SM, Forbes DL, Whalen D, Taylor B, Frobel D, Parlee K (2006) Hazards to coastal infrastructure in Canada and the implications of climate change: with special reference to the Mackenzie Delta and Tuktoyaktuk. In: Presentation at Coastal Zone Canada 2006 conference. Tuktoyaktuk, Northwest Territories, Canada. 14–18 Aug 2006
- Manson, G., and S. Solomon (2007): Past and future forcing of Beaufort Sea coastal change. *Atmos.–Ocean*, 45, 107–122.
- Marcy, D., N. Herold, K. Waters, NOAA Coastal Services Center; W. Brooks, B. Hadley, M. Pendleton, K. Schmid, M. Sutherland, I.M. Systems Group; K. Dragonov, J. McCombs, S. Ryan, The Baldwin Group (2011). *New Mapping Tool and Techniques for Visualizing Sea Level Rise and Coastal Flooding Impacts*. NOAA Coastal Services Center, South California.
- MARETEC. (2012). *Descrição do MOHID*. (E. Editora, ed.), Instituto Superior Técnico.

- Marsh P, Russell M, Pohl S, Haywood H, Onclin C. (2009). Changes in thaw lake drainage in the western Canadian Arctic from 1950 to 2000. *Hydrological Processes* 23: 145–158. <https://doi.org/10.1002/hyp.7179>
- Martins, F. A., Neves, R. J., and Leitão, P. C. (1998). A three-dimensional hydrodynamic model with generic vertical coordinate. *Hydro-informatics* 98, (Bryan), 1403–1410.
- Martins, F., Leitão, P. C., Silva, A., and Neves, R. (2001). 3D modelling in the Sado estuary using a new generic vertical discretization approach. *Oceanologica Acta*, 24, 51–62.
- Mateus, M., & Neves, R. (2013). Ocean modelling management for coastal Case Studies with MOHID. In *Ocean modelling for coastal management – Case studies with MOHID* (Vol. 68, Issue C).
- McCulloch, M.M., Forbes, D.L., Shaw, R.W., and the CCAF A041 Scientific Team (2002). Coastal impacts of climate change and sea-level rise on Prince Edward Island. Edited by D.L. Forbes and R.W. Shaw. CD-ROM. Geological Survey of Canada, Open File 4261, xxxiv + 62 pp. and 11 supporting documents.
- McLean, R., A. Tsyban, V. Burkett, J. O. Codignotto, D. L. Forbes, N. Mimura, R. J. Beamish and V. Ittekkot, (2001): Coastal zone and marine ecosystems. *Climate Change 2001: Impacts, Adaptation and Vulnerability. Contribution of Working Group II to the Third Assessment Report of the Intergovernmental Panel on Climate Change*, J. J. McCarthy, O. F. Canziani, N. A. Leary, D. J. Dokken and K.S. White, Eds., Cambridge University Press, Cambridge, 343-380.
- Meehl, G.A., et al., (2007). Global climate projections, I: Climate change 2007: the physical science basis, contribution of working group I to the Fourth Assessment Report of the Intergovernmental Panel on Climate Change, Solomon, S. et al. (eds.), Cambridge University Press, Cambridge, UK and New York, USA.
- Milne, G.A., W.R. Gehrels, C.W. Hughes, and M.E. Tamisiea, (2009). Identifying the causes of sea-level change, *Nat. Geosc.*, 2, 471-478.
- Moss, R.H., J.A. Edmonds, K.A. Hibbard, M.R. Manning, S.K. Rose, D.P. van Vuuren, T.R. Carter, S. Emori, M. Kainuma, T. Kram, G.A. Meehl, J.F.B. Mitchell, N. Nakicenovic, K. Riahi, S.J. Smith, R.J. Stouffer, A.M. Thomson, J. P. Weyant, T.J. Wilbanks, (2010). The next generation of scenarios for climate change research and assessment, *Nature*, 463, 747-756, <https://doi.org/10.1038/nature08823>
- Mourato, S.; Fernandez, P.; Pereira, L.; Moreira, M. (2017). Improving a DSM Obtained by Unmanned Aerial Vehicles for Flood Modelling. *IOP Conf. Ser. Earth Environ. Sci.*, 95.
- Nakicenovic, N., and R. Swart (eds.), (2000). *Special report on emissions scenarios*, Cambridge University Press, UK., 570 pp.
- NHC (2021). Storm surge overview. <https://www.nhc.noaa.gov/surge/>
- NOAA (2021). Average Seasonal Cycle 970-211 Tuktoyaktuk, Canada, https://tidesandcurrents.noaa.gov/sltrends/sltrends_station.shtml?id=970-211

NOAA (2021). Global mean sea level from TOPEX/Poseidon, Jason-1, Jason-2, and Jason-3. https://www.star.nesdis.noaa.gov/socd/lisa/SeaLevelRise/LSA_SLR_timeseries_global.php

NOAA (2021). What is storm surge?. <https://oceanservice.noaa.gov/facts/stormsurge-stormtide.html>
com

Overeem, I., R. S. Anderson, C. W. Wobus, G. D. Clow, F. E. Urban, and N. Matell (2011), Sea ice loss enhances wave action at the Arctic coast, *Geophys. Res. Lett.*, 38, doi:10.1029/2011GL048681

P. P. Overduin, M. C. Strzelecki, M. N. Grigoriev, N. Couture, H. Lantuit, D. St-Hilaire-Gravel, F. Günther and S. Wetterich (2014). Coastal changes in the Arctic. Geological Society, London, Special Publications, first published February 12, 2014; doi 10.1144/SP388.13

Pajares, G. Overview and Current Status of Remote Sensing Applications Based on Unmanned Aerial Vehicles (UAVs) (2015). *Photogramm. Eng. Remote Sens.*, 81, 281–329.

Parker, B.B. (2007). Tidal analysis and prediction. NOAA Special Publication NOS CO-OPS 3.

Pugh, D.J., (1987). Tides, Surges and Mean Sea-Level. A handbook for engineers and scientists, Wiley, Chichester. 472 pp.

Räisänen J. (2001) CO₂-induced climate change in CMIP2 experiments: Quantification of agreement and role of internal variability. *J Climate* 14:2088–2104

Ramage, J. L., Irrgang, A. M., Morgenstern, A., & Lantuit, H. (2018). Increasing coastal slump activity impacts the release of sediment and organic carbon into the Arctic Ocean. *Biogeosciences*, 15(5), 1483–1495. <https://doi.org/10.5194/bg-15-1483-2018>

Reimnitz, E., & Maurer, D.F. (1978). Storm surges in the Alaskan Beaufort Sea. U.S. Geological Survey, Open file report 78-593, 13p.

Reimnitz, E., & Maurer, D.F. (1979). Effects of Beaufort Sea surges on the Beaufort Sea coast, Northern Alaska. *Arctic*, 32, 329-344.

Sampson, C.C., Smith, A.M., Bates, P.D., Neal, J.C.; Trigg, M.A. (2016). Perspectives on open access high resolution digital elevation models to produce global flood hazard layers. *Front. Earth Sci.*, 3, 85.

Santos, A. J. (1995). “Modelo Hidrodinâmico Tridimensional de Circulação Oceânica e Estuarina.” Instituto Superior Técnico, Lisboa.

Schumann, G.J.P.; Muhlhausen, J.; Andreadis, K.M. (2019) Rapid Mapping of Small-Scale River-Floodplain Environments Using UAV SfM Supports Classical Theory. *Remote Sens.*, 11, 982.

Seenath, A., Wilson M., Miller, K. (2015). Hydrodynamic versus GIS modelling for coastal flood vulnerability assessment: Which is better for guiding coastal management? *Ocean & Coastal Management*, 120, 99-109. <https://doi.org/10.1016/j.ocecoaman.2015.11.019>

Serreze, M. C., M. M. Holland, and J. Stroeve (2007), Perspectives of the Arctic's shrinking ice cover, *Science*, 315, 1533–1536

Shaw, J., R.B. Taylor, D.L. Forbes, M.-H. Ruz and S. Solomon (1998). "Sensitivity of the coasts of Canada to sea-level rise". Geological Survey of Canada, 505, p. 90.

Shishir K. Dube, Tad S. Murty, Jesse C. Feyen, Reggina Cabrera, Bruce A. Harper, Jerad D. Bales, Saud Amer, (2010). Storm surge modeling and applications in coastal areas. *World scientific series on Asia-Pacific weather and climate – Global perspectives on tropical cyclones*, 4, 363-406, https://doi.org/10.1142/9789814293488_0012

Simmonds, I., C. Burke, and K. Keay (2008): Arctic climate change as manifest in cyclone behaviour. *J. Climate*, 21, 5777–5796.

Small, D., Atallah, E., & Gyakum, J. (2011). Wind regimes along the Beaufort Sea coast favorable for strong wind events at Tuktoyaktuk. *Journal of Applied Meteorology and Climatology*, 50(6), 1291–1306. <https://doi.org/10.1175/2010JAMC2606.1>

Smith SL, Burgess MM, Riseborough D, Nixon M. (2005). Recent trends from Canadian permafrost thermal monitoring network sites. *Permafrost and Periglacial Processes* 16: 19 –30. <https://doi.org/10.1002/ppp.511>

Solomon, S. M. (2005). Spatial and temporal variability of shoreline change in the Beaufort-Mackenzie region, northwest territories, Canada. *Geo-Marine Letters*, 25(2–3), 127–137. <https://doi.org/10.1007/s00367-004-0194-x>

Steedman AE, Lantz TC, Kokelj SV. (2016). Spatio-temporal variation in high-centre polygons and ice-wedge melt ponds, Tuktoyaktuk coastlands, Northwest Territories. *Permafrost and Periglacial Processes* (in press) <https://doi.org/10.1002/ppp.1880>

Stern, N., 2007. *The economics of climate change: The Stern review*, Cambridge University Press.

Strauss, B.H.; Ziemiński, R.; Weiss, J.L.; Overpeck, J.T. (2012). Tidally adjusted estimates of topographic vulnerability to sea level rise and flooding for the contiguous United States. *Environ. Res. Lett.*, 7, 014033.

Tarik Benkaci (2021). Flood Frequency Distribution (FFD 2.1) (https://github.com/TBenkHyd2/Flood_Freq_Matlab), GitHub. Retrieved August 30, 2021.

Terenzi, J., M. T. Jorgenson, and C. R. Ely. 2014. Storm-surge flooding on the Yukon-Kuskokwim Delta, Alaska. *Arctic* 67 (3):360–74. doi: 10.14430/arctic4403

Timoney KP, La Roi GHL, Zoltai SC, Robinson AL. (1992). The high subarctic forest-tundra of northwestern Canada: position, width, and vegetation gradients in relation to climate. *Arctic* 45: 1 –19. <https://doi.org/10.14430/arctic1367>

Titus, J.G.; Richman, C. (2001). Maps of lands vulnerable to sea level rise: Modeled elevations along the US Atlantic and Gulf Coasts. *Clim. Res.*, 18, 205–228.

Trillium Engineering and Hydrographs Inc. November 1997. Tuktoyaktuk Erosion Control Using Monolithic Concrete Slabs.

Vaan de Sante, B.; Lansen, J.; Claartje, H. (2012). Sensitivity of coastal flood risk assessments to digital elevation models. *Water*, 4, 568–579.

Véronneau, M. (2014). The Canadian Geodetic Vertical Datum of 2013(CGVD2013) [ppt]. <https://cdnscepub.com/doi/10.5623/ciq2016-101>.

Vieira, R., Antunes, C., Taborda, R. (2012). Caracterização da sobrelevação meteorológica em Cascais nos últimos 50 anos. 2^{as} Jornadas de Engenharia Hidrográfica.1. 20-22.

Webster, T. L., Forbes, D. L., MacKinnon, E., Roberts, D. (2006). Flood-risk mapping for storm-surge vents and sea-level rise using lidar or southeast New Brunswick.

Webster, T.L., Christian, M., Sangster, C., and Kingston, D. (2004b). High- resolution elevation and image data within the Bay of Fundy coastal zone, Nova Scotia, Canada. In *GIS for coastal zone management*. Edited by D. Bartlett and J. Smith. CRC Press, Boca Raton, Fla. Chapt. 15, pp. 195–218.

Webster, T.L., Dickie, S., O'Reilly, C., Forbes, D.L., Parkes, G., Poole, D., and Quinn, R. (2003). Mapping storm-surge flood risk using a LIDAR-derived DEM. *Elevation (Supplement to Geospatial Solutions and GPS World)*, May 2003, pp. 4–9.

Webster, T.L., Dickie, S., O'Reilly, C., Forbes, D.L., Thompson, K., and Parkes, G. (2001). Integration of diverse datasets and knowledge to produce high resolution elevation flood risk maps for Charlottetown, Prince Edward Island, Canada. In *CoastGIS2001, 4th International Symposium on Computer Mapping and GIS for Coastal Zone Management*, Halifax, N.S. Vol. 2, 27 pp.

Webster, T.L., Forbes, D.L., Dickie, S., and Shreenan, R. (2004a). Using topographic lidar to map flood risk from storm-surge events for Charlottetown, Prince Edward Island, Canada. *Canadian Journal of Remote Sensing*, Vol. 30, No. 1, pp. 1–13.

Wehr A, Lohr U (1999) Airborne laser scanning - an introduction and overview. *ISPRS J Photogrammetry Remote Sens* 54(2–3):68–82

Whalen, D., Forbes, D.L., Hopkinson, C., Lavergne, J.C., Manson, G.K., Marsh, P., Solomon S.M. (2009). Topographic LiDAR - providing a new perspective in the Mackenzie Delta, Canadian Symposium on Remote Sensing.

Yunus, A. P., Avtar, R., Kraines, S., Yamamuro, M., Lindberg, F., & Grimmond, C. S. B. (2016). Uncertainties in tidally adjusted estimates of sea level rise flooding (bathtub model) for the greater London. Remote Sensing, 8(5). <https://doi.org/10.3390/rs8050366>

8. Appendix

Table A 1 - GPS points used to determine the RMSE of the UAV DSM.

OBJECTID	X	Y	Z Drone	Z GPS	Z GPS - Z Drone	Squared Difference
1	578602.89	7704493.03	3.250	3.467	0.216	0.047
2	578548.32	7704829.72	3.719	3.543	-0.176	0.031
3	578284.74	7704997.98	3.024	3.323	0.298	0.089
6	577884.97	7704084.48	5.539	5.665	0.126	0.016
8	577480.99	7704148.25	4.340	4.502	0.162	0.026
9	576763.88	7705173.12	3.828	3.940	0.112	0.013
10	577407.32	7705074.85	2.721	2.867	0.146	0.021
13	576782.75	7705856.42	7.423	7.423	-0.001	0.000
17	576890.42	7706443.69	2.595	2.670	0.075	0.006
18	576876.56	7706449.70	2.587	2.734	0.147	0.022
19	576878.00	7706454.49	2.372	2.513	0.141	0.020
20	576886.02	7706454.22	2.047	2.099	0.052	0.003
27	576776.61	7705675.20	1.400	1.452	0.052	0.003
29	576746.87	7705443.26	1.057	1.082	0.025	0.001
33	576684.69	7705353.35	0.620	0.769	0.149	0.022
37	576962.87	7705227.42	1.347	1.394	0.047	0.002
40	576951.17	7705716.98	2.234	2.397	0.163	0.027
41	577189.07	7705329.76	1.254	1.343	0.089	0.008
42	577199.47	7705295.22	2.680	2.716	0.036	0.001
43	577792.04	7705191.86	1.422	1.377	-0.045	0.002
44	577796.21	7705188.44	1.588	1.594	0.006	0.000
45	577644.09	7705046.69	0.349	0.286	-0.063	0.004
47	577672.01	7704546.97	1.153	1.120	-0.033	0.001
48	577709.32	7704462.44	1.722	1.762	0.040	0.002
49	577836.51	7704475.06	1.472	1.479	0.007	0.000
50	577838.41	7704473.42	1.607	1.569	-0.038	0.001
51	577840.38	7704471.71	1.663	1.686	0.023	0.001
52	577842.30	7704470.07	1.795	1.788	-0.007	0.000
53	577844.54	7704468.20	2.239	2.248	0.009	0.000
54	577846.09	7704466.87	2.670	2.639	-0.031	0.001
55	577037.65	7704841.60	1.187	1.367	0.180	0.032
56	577028.04	7704812.84	2.067	2.022	-0.045	0.002
57	577015.71	7704642.73	1.289	1.336	0.047	0.002
58	578568.64	7704768.21	1.565	1.492	-0.073	0.005
59	578531.87	7704764.59	1.243	1.242	-0.001	0.000

Table A 2 - GPS points used to determine the RMSE of the LiDAR DEM.

OBJECTID	X	Y	Z LiDAR	Z GPS	Z GPS - Z LiDAR	Squared Difference
2	578548.32	7704829.72	3.448	3.543	0.094	0.009
4	578443.65	7704199.08	4.637	5.587	0.950	0.902
7	577802.18	7704111.83	3.996	4.013	0.016	0.000
13	576782.75	7705856.42	7.240	7.423	0.182	0.033
14	577052.86	7705912.46	2.059	1.914	-0.145	0.021
17	576890.42	7706443.69	2.541	2.670	0.129	0.017
24	576826.41	7706146.44	2.194	2.162	-0.032	0.001
25	576723.52	7705653.82	1.029	1.526	0.497	0.247
27	576776.61	7705675.20	1.439	1.452	0.013	0.000
28	576784.14	7705670.01	1.621	1.555	-0.066	0.004
31	576806.98	7705471.45	1.427	1.694	0.267	0.071
33	576684.69	7705353.35	0.559	0.769	0.210	0.044
37	576962.87	7705227.42	1.525	1.394	-0.131	0.017
39	576927.65	7705687.60	2.195	2.400	0.205	0.042
41	577189.07	7705329.76	1.211	1.343	0.132	0.017
42	577199.47	7705295.22	2.672	2.716	0.044	0.002
43	577792.04	7705191.86	1.307	1.377	0.070	0.005
44	577796.21	7705188.44	1.569	1.594	0.025	0.001
45	577644.09	7705046.69	0.018	0.286	0.268	0.072
46	577633.85	7705050.56	0.545	0.402	-0.143	0.020
47	577672.01	7704546.97	1.092	1.120	0.028	0.001
48	577709.32	7704462.44	1.871	1.762	-0.109	0.012
49	577836.51	7704475.06	1.465	1.479	0.014	0.000
50	577838.41	7704473.42	1.646	1.569	-0.077	0.006
52	577842.30	7704470.07	1.750	1.788	0.038	0.001
56	577028.04	7704812.84	1.801	2.022	0.221	0.049
57	577015.71	7704642.73	1.453	1.336	-0.117	0.014
58	578568.64	7704768.21	1.817	1.492	-0.325	0.106
69	578604.42	7704516.58	3.725	3.533	-0.192	0.037

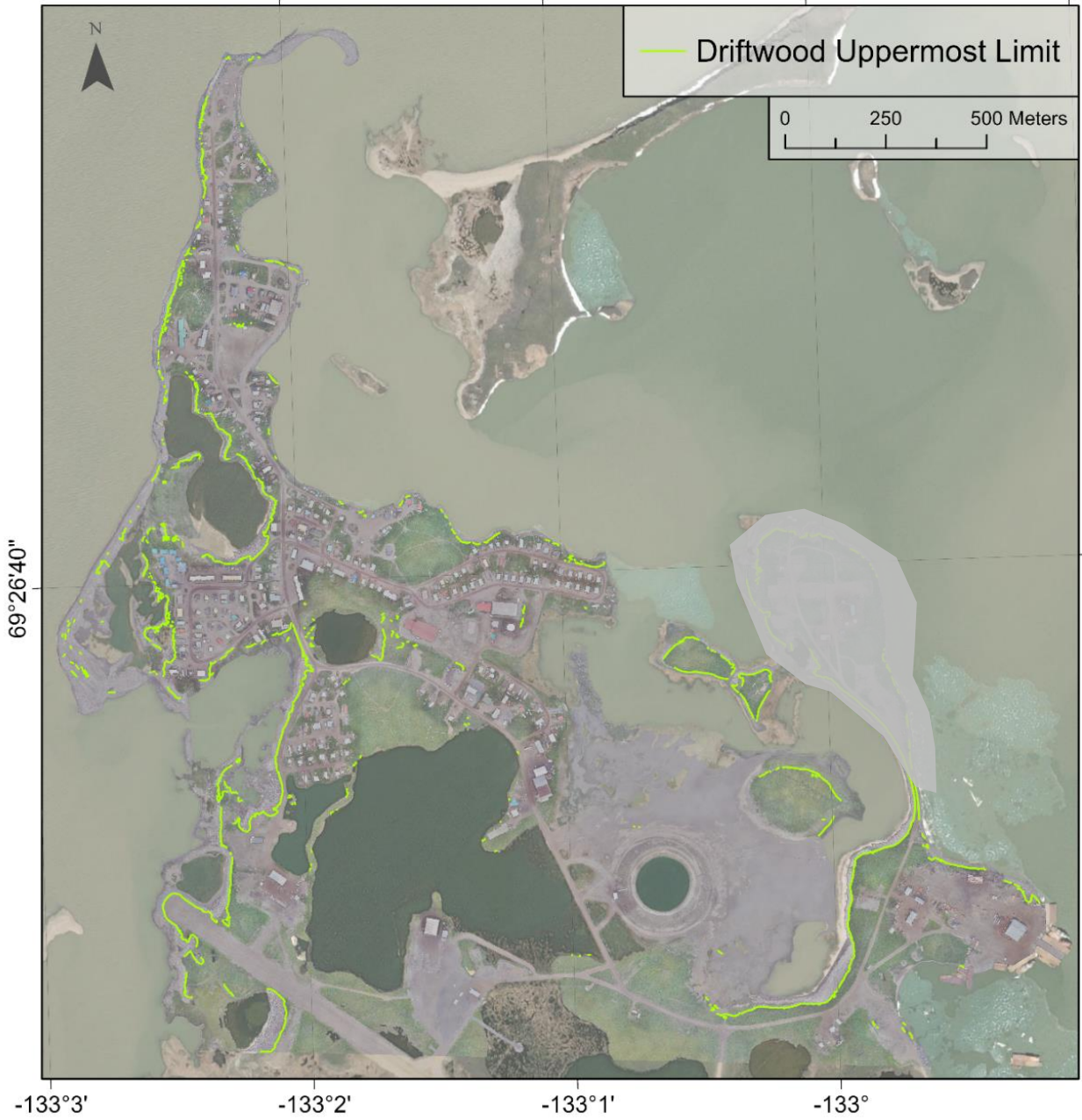


Figure A 1 - Driftwood uppermost limit derived from the UAV orthophotomaps, manually digitized and vectorized as linear features.



Figure A 2 - Flood and coastal erosion affected locations, comments and historical water heights identified by the staff of Hamlet of Tuktoyaktuk (Courtesy of Calvin Pokiak – unpublished).

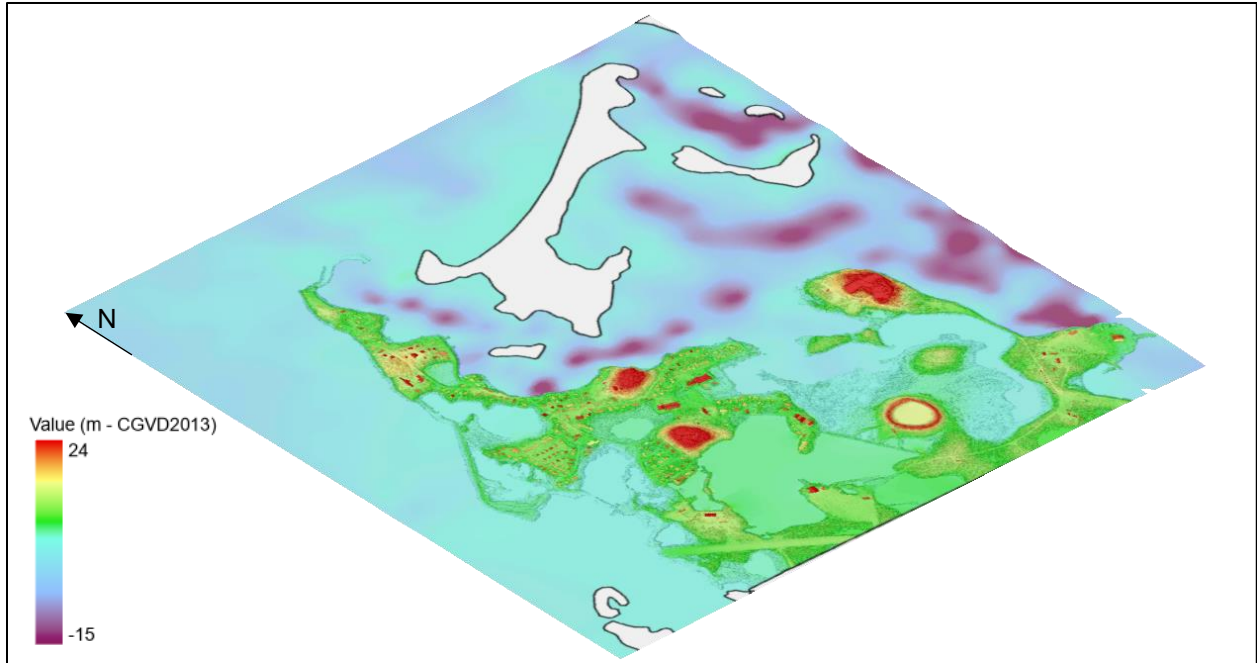


Figure A 3 – MOHID Grid data (5 x 5 m) of the UAV DSM combined with the bathymetry derived from Tuktoyaktuk Harbour nautical chart, rendered in ArcGIS Pro.

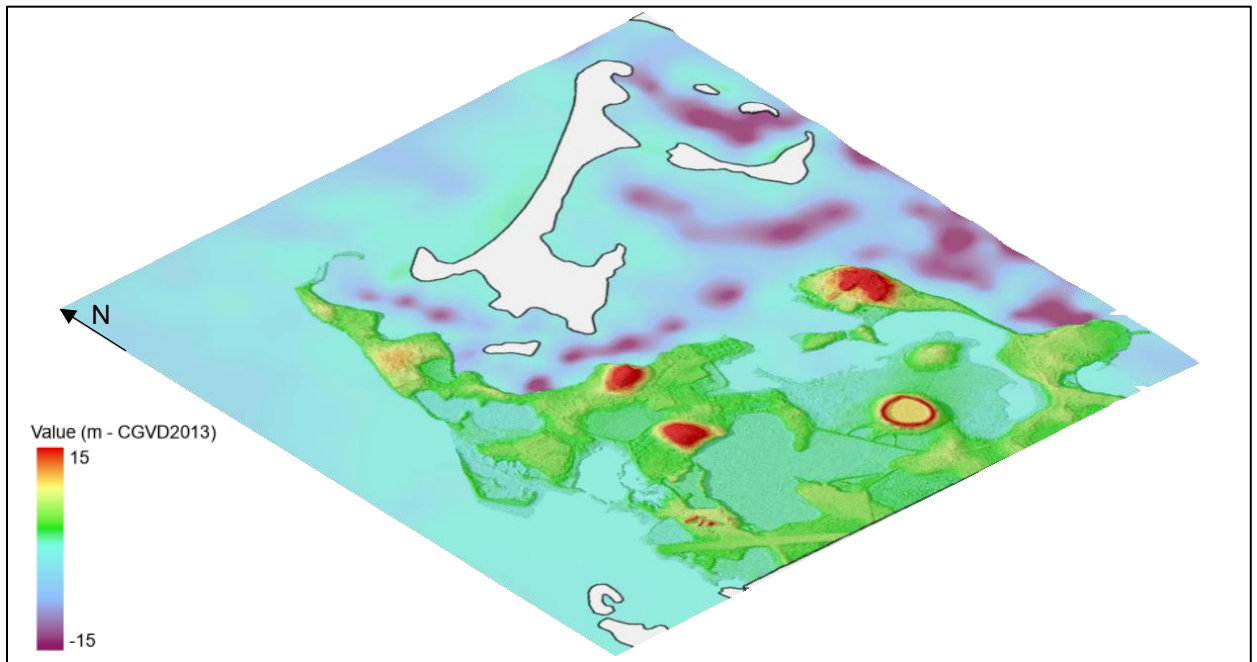


Figure A 4 - MOHID Grid data (5 x 5 m) of the LiDAR DEM combined with the bathymetry derived from Tuktoyaktuk Harbour nautical chart, rendered in ArcGIS Pro.

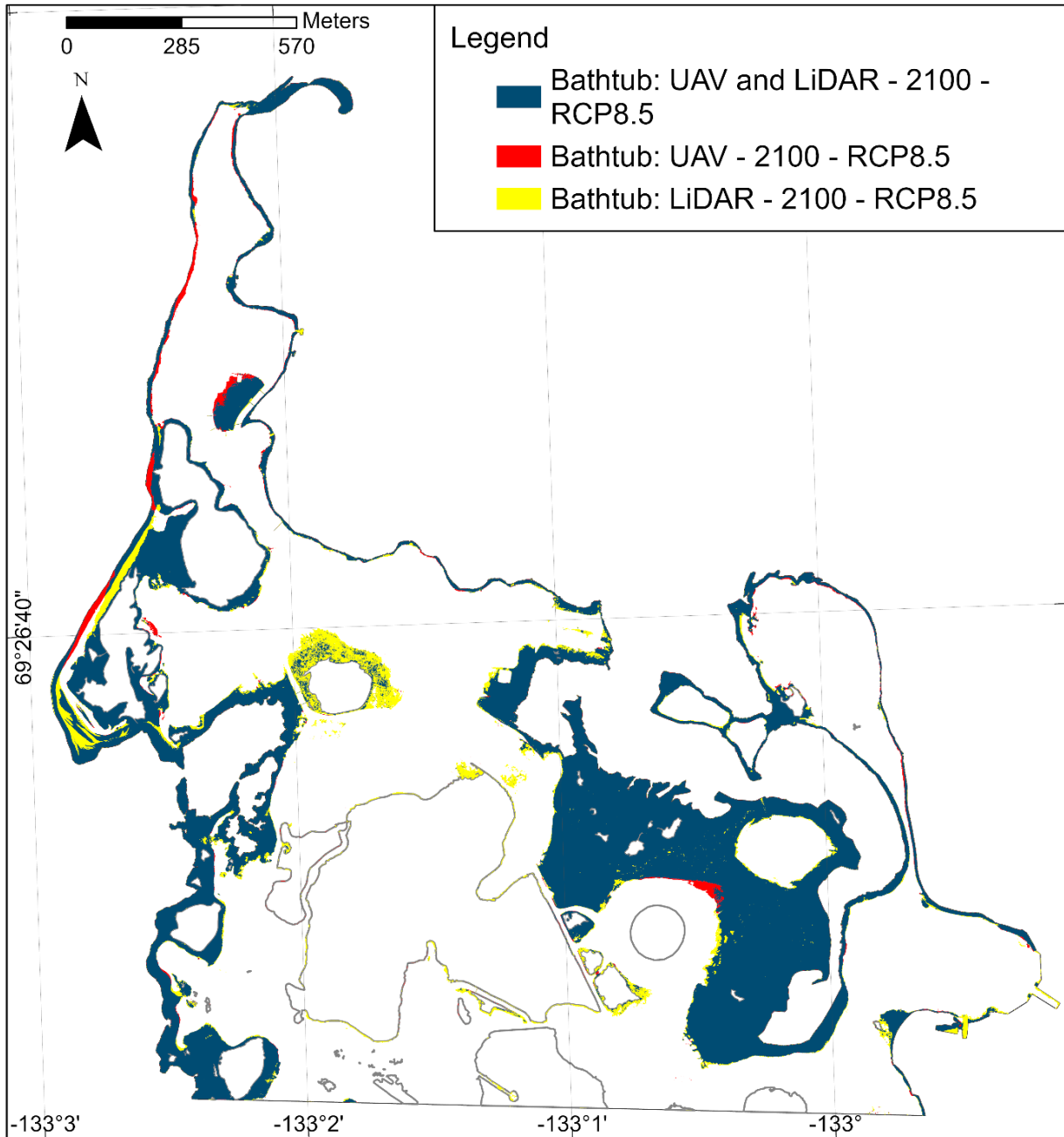


Figure A 5 - Differences and overlapped extents of the bathtub model with a sea level rise scenario RCP8.5 for UAV and LiDAR with all hazard classes grouped for the year 2100.

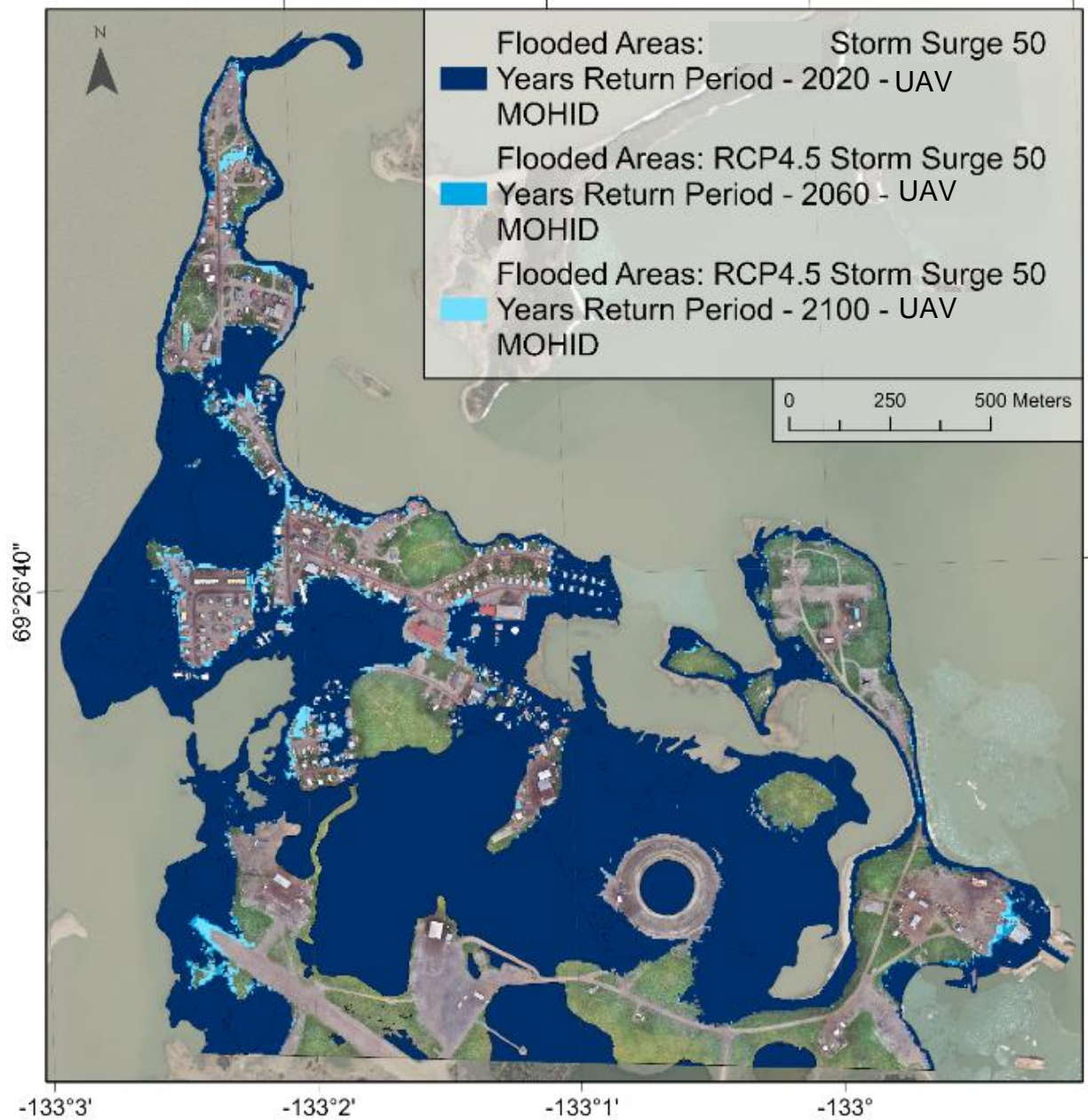


Figure A 6 - MOHID flooded areas for 2020, 2060 and 2100 for the RCP4.5 scenario with a 50-year return period storm surge on UAV DSM.

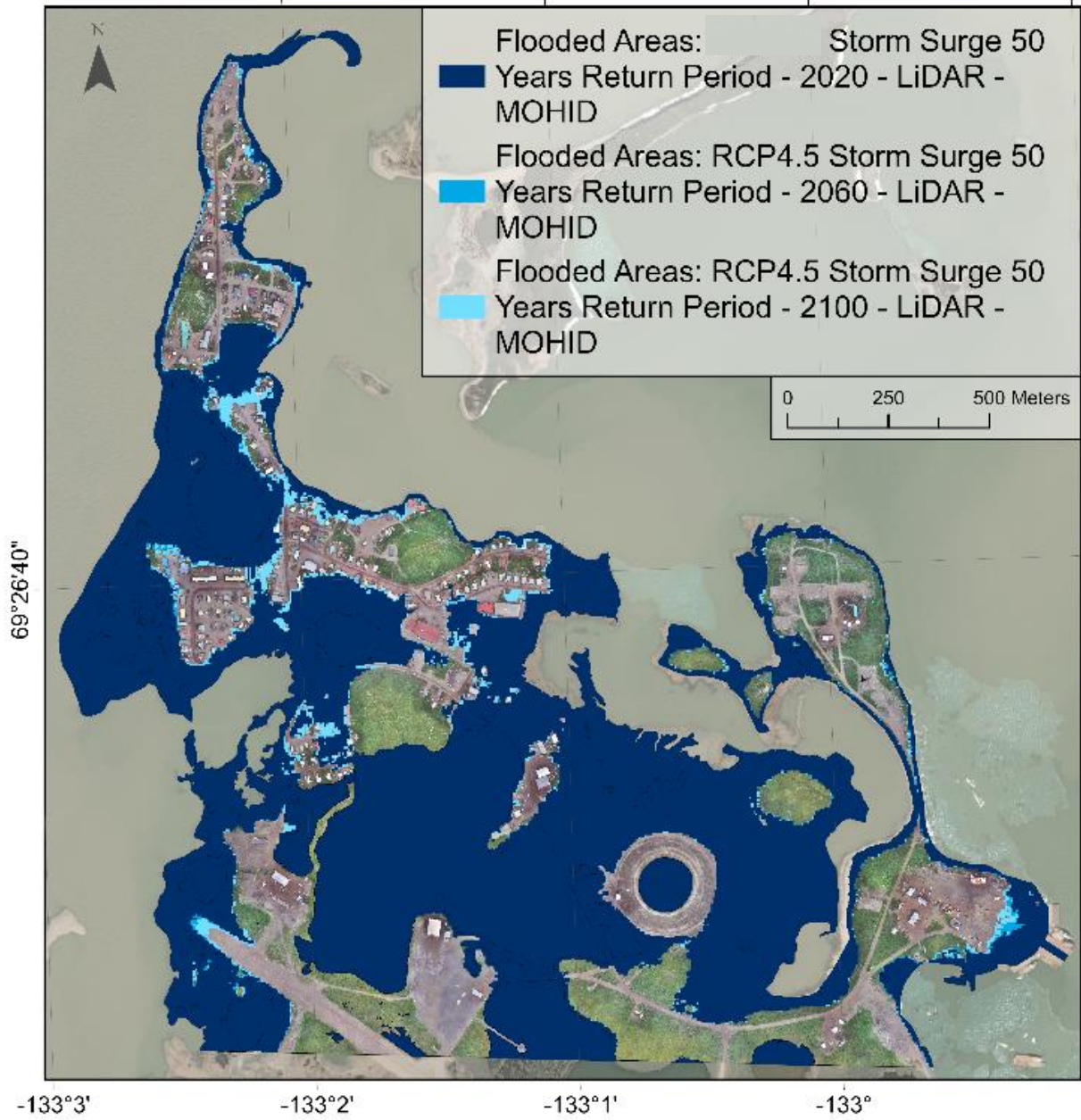


Figure A 7 - MOHID flooded areas for 2020, 2060 and 2100 for the RCP4.5 scenario with a 50-year return period storm surge on LiDAR DEM.

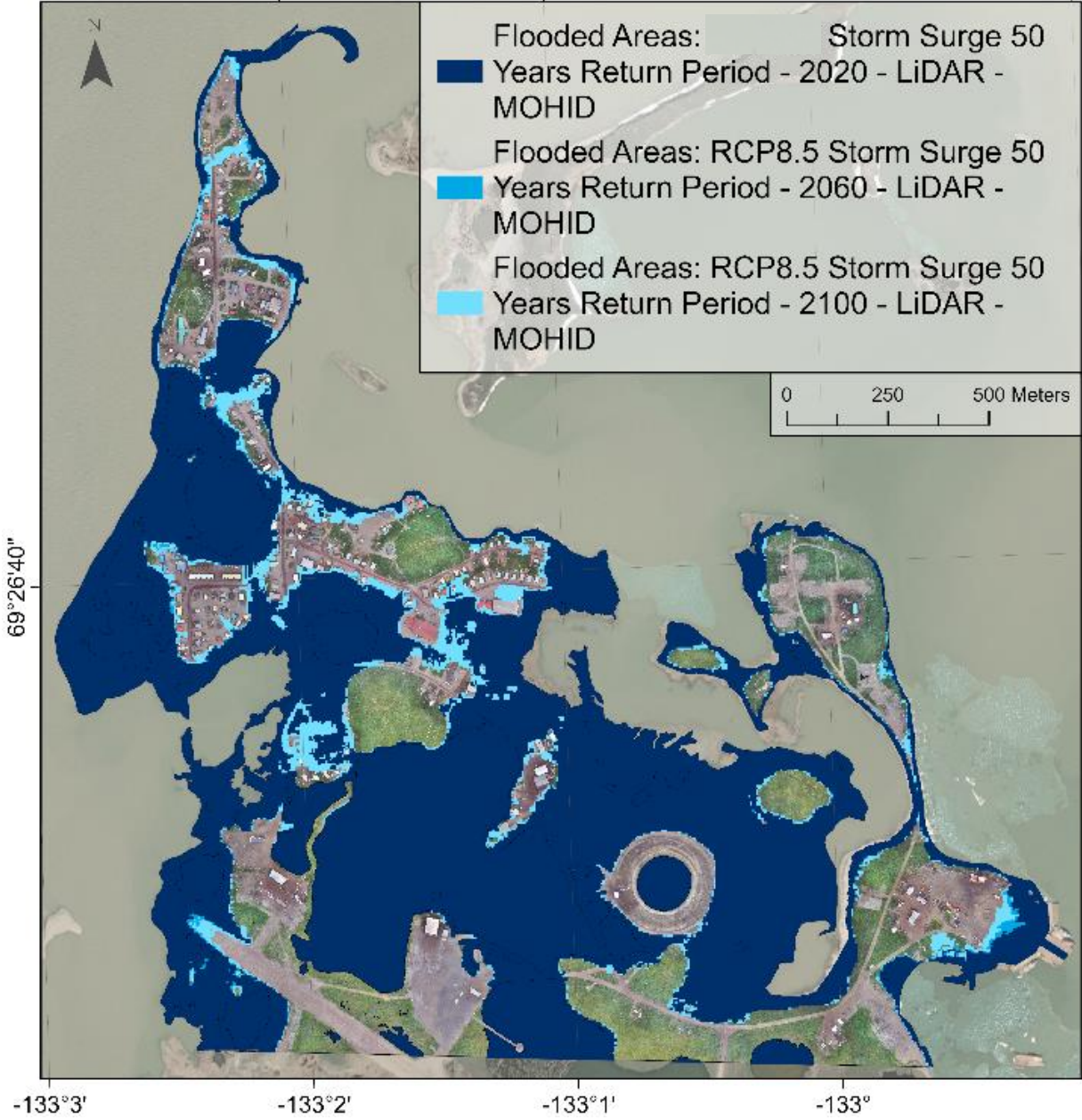


Figure A 8 - MOHID flooded areas for 2020, 2060 and 2100 for the RCP8.5 scenario with a 50-year return period storm surge on LiDAR DEM.

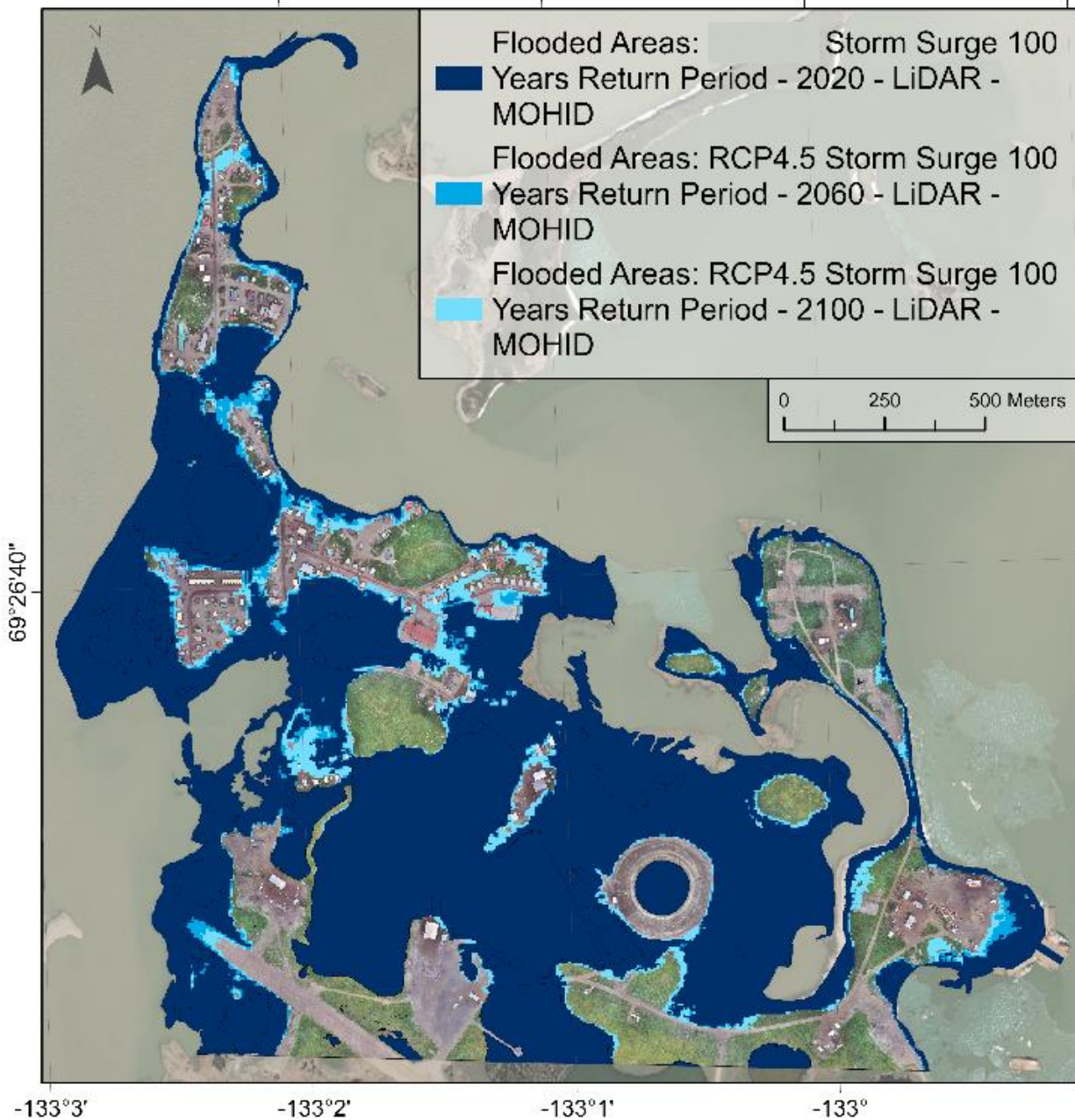


Figure A 9 - MOHID flooded areas for 2020, 2060 and 2100 for the RCP4.5 scenario with a 100-year return period storm surge on LiDAR DEM.

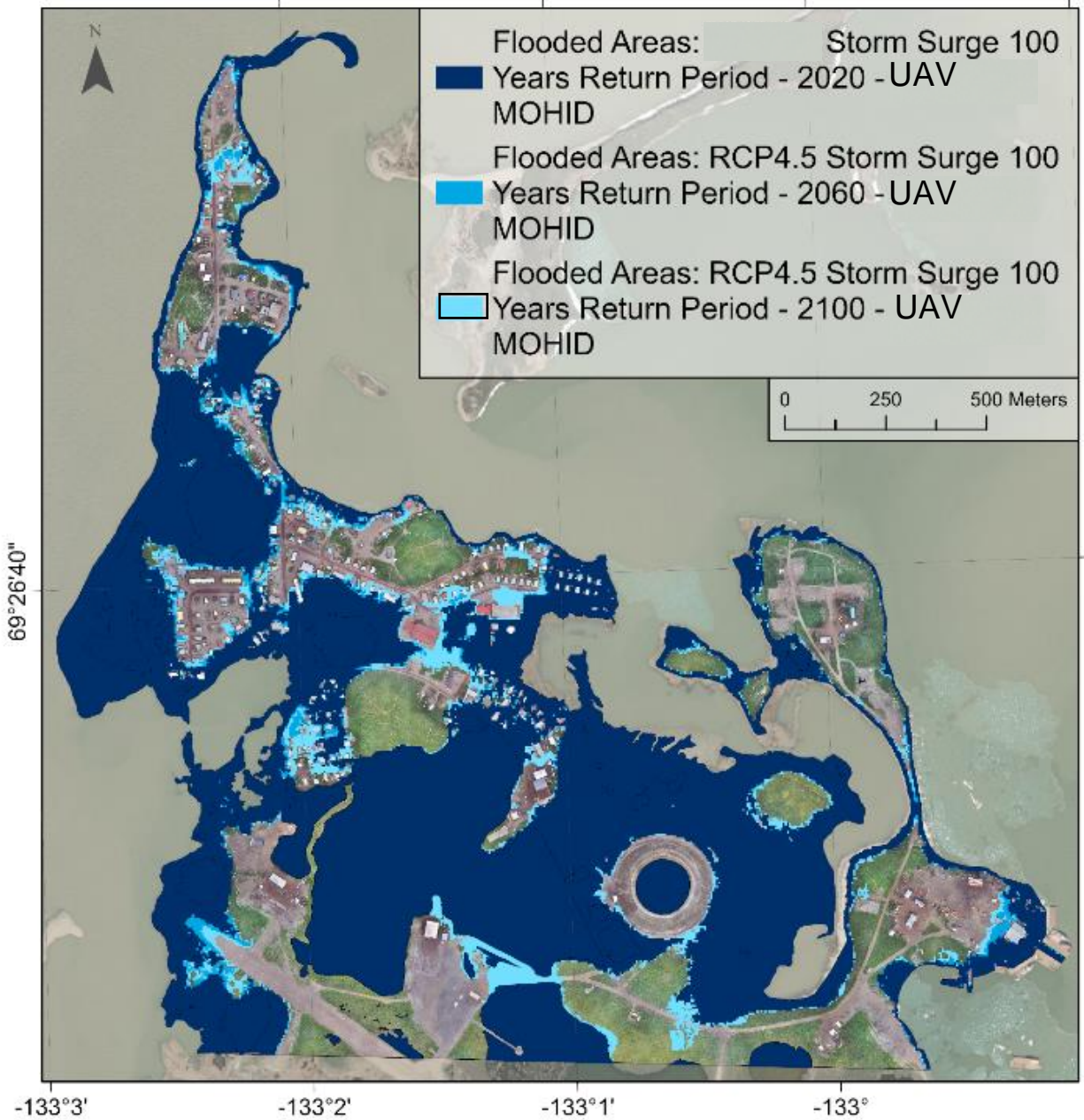


Figure A 10 – MOHID flooded areas by year for with a 100-year return period storm surge on UAV DSM and RCP4.5 scenario.

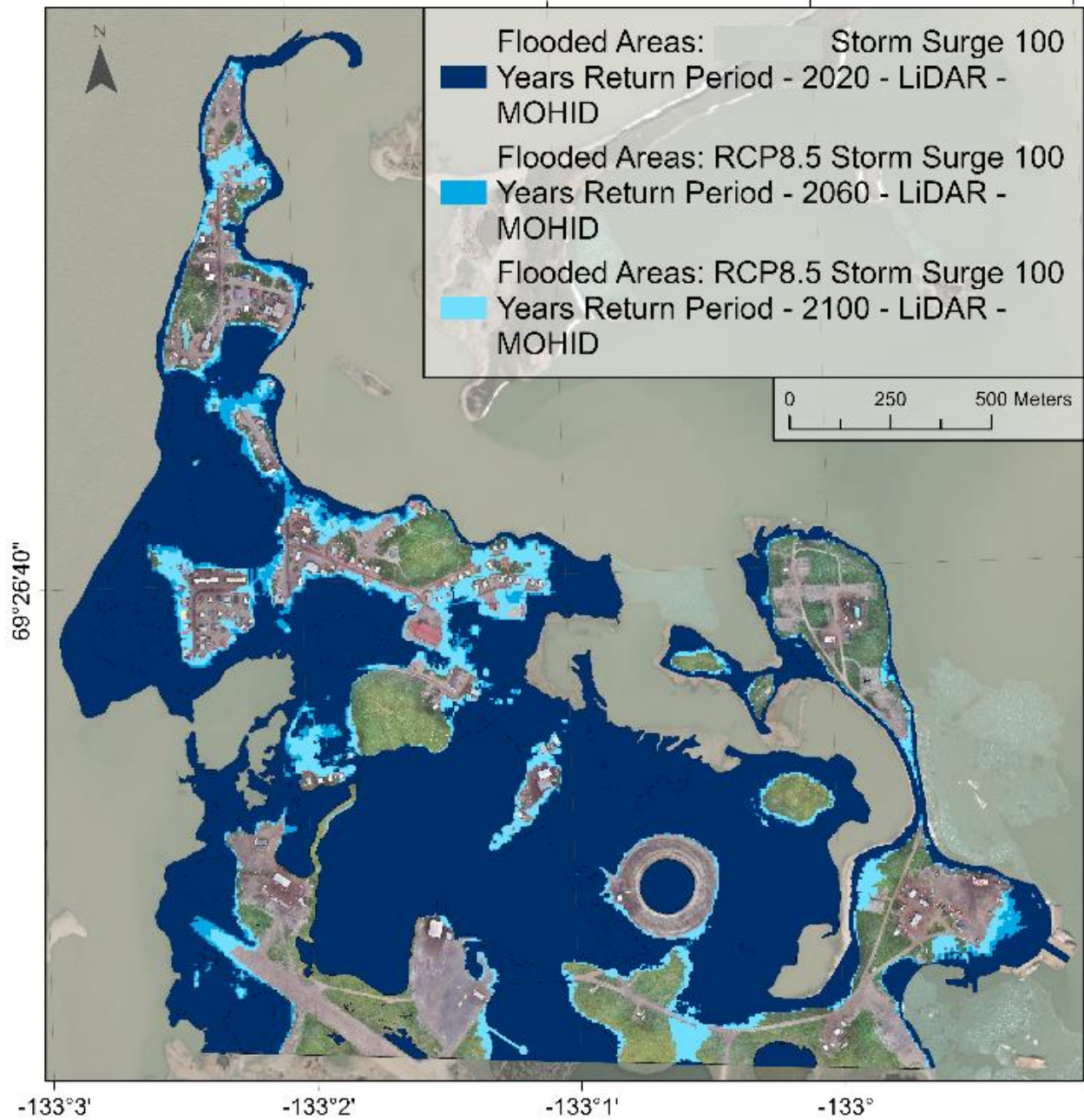


Figure A 11 - MOHID flooded areas for 2020, 2060 and 2100 for the RCP8.5 scenario with a 100-year return period storm surge on LiDAR DEM.

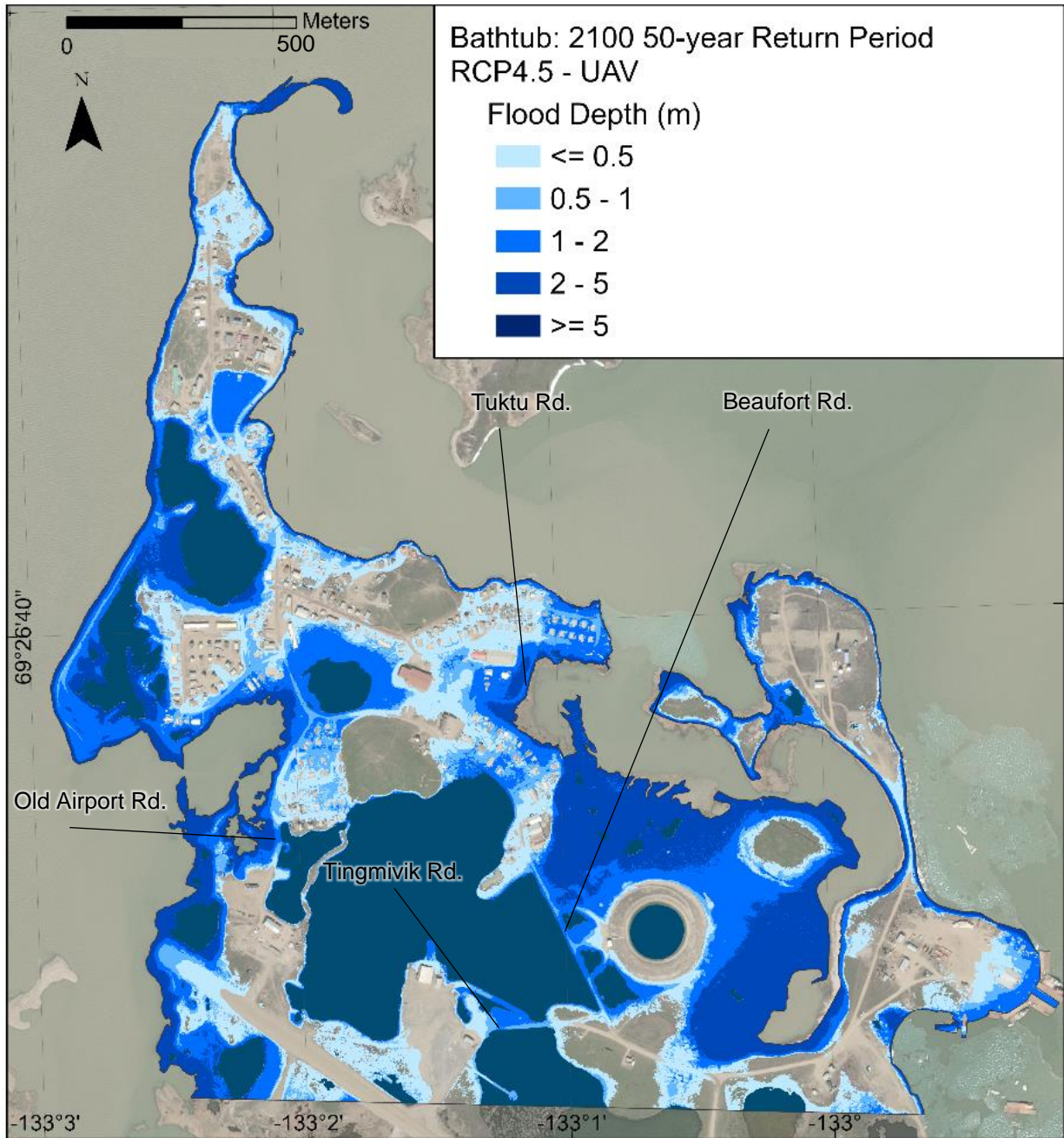


Figure A 12 - Flood depth for the RCP4.5 scenario and a storm surge event with a 50-year return period on UAV DSM.

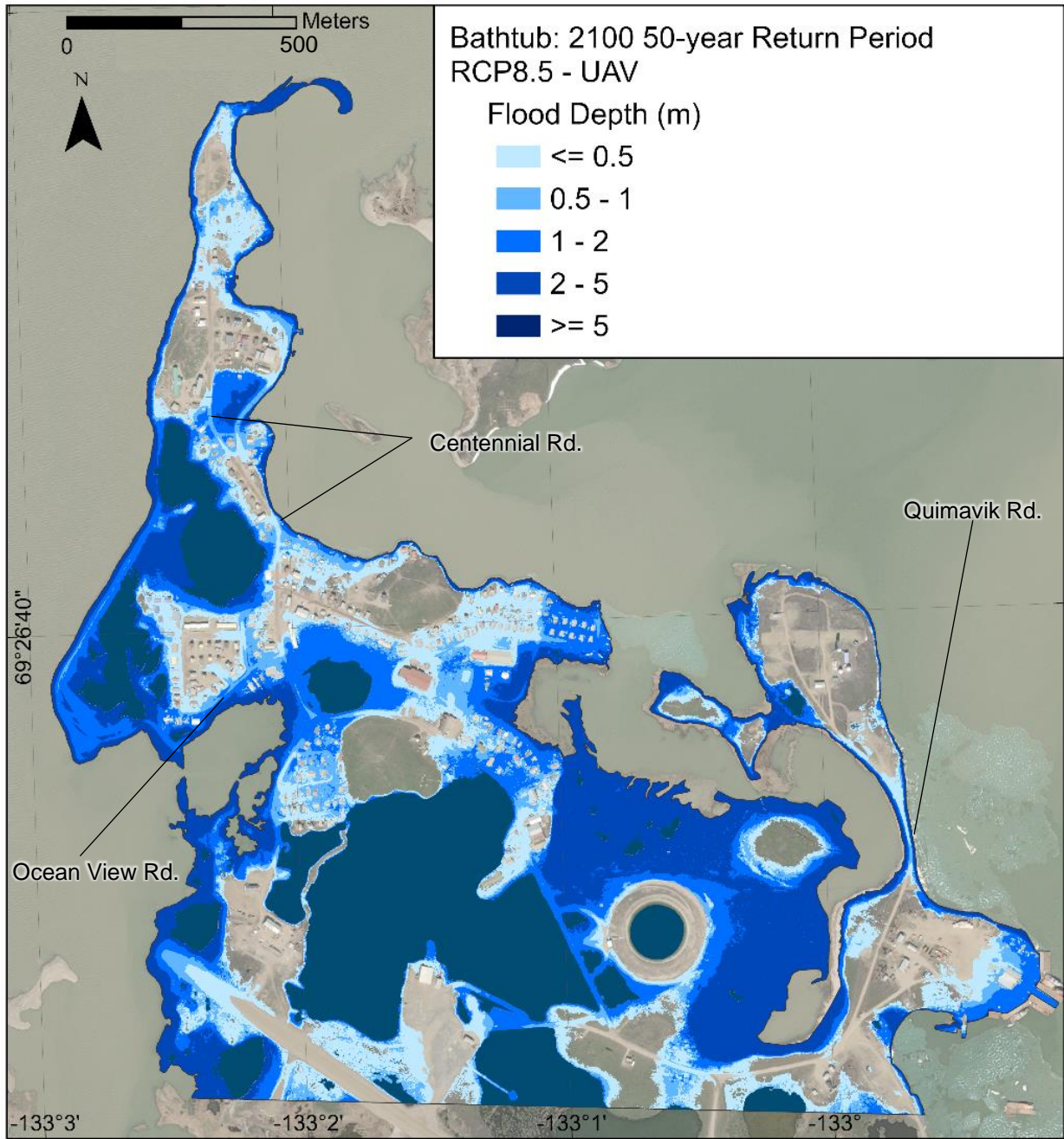


Figure A 13 - Flood depth for the RCP8.5 scenario and a storm surge event with a 50-year return period on UAV DSM.

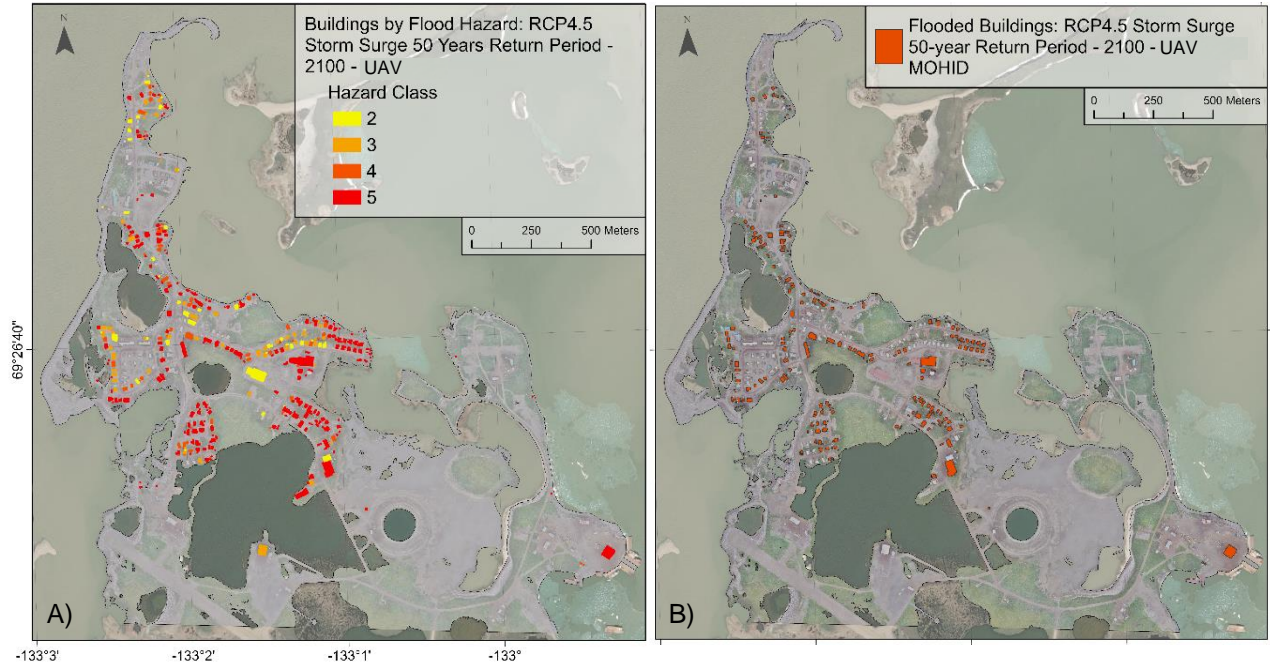


Figure A 14 - Flooded buildings by model for the year 2100 and scenario RCP4.5 with a 50-year return period storm surge event on UAV DSM. A) Bathtub. B) MOHID.

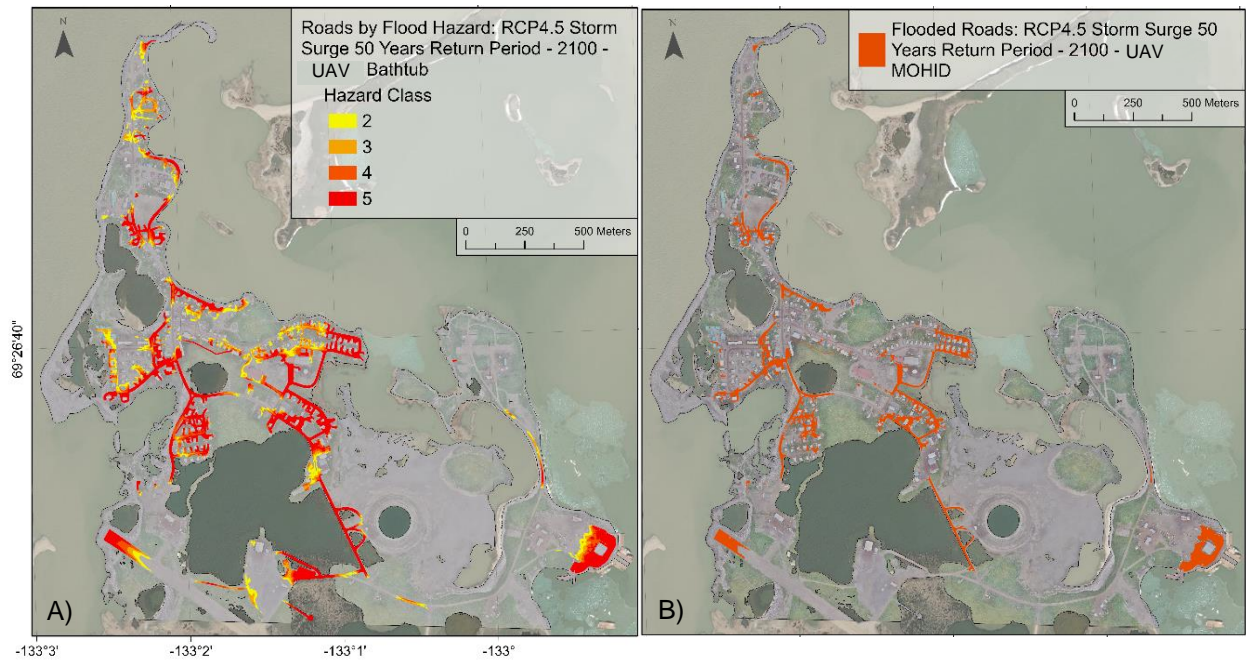


Figure A 15 - Flooded roads by model for the year 2100 and scenario RCP4.5 with a 50-year return period storm surge event on UAV DSM. A) Bathtub. B) MOHID.